NTNU
Norwegian University of
Science and Technology

Numerical and Experimental Study of the Fred Olsen Wind Turbine Concept

Marius Maastad

Marine Technology
Submission date: December 2016
Supervisor: Zhen Gao, IMT

Norwegian University of Science and Technology
Department of Marine Technology

NTNU Trondheim
Norwegian University of Science and Technology
Department of Marine Technology – Group of Marine Structures

MSC THESIS IN MARINE TECHNOLOGY

FALL 2016

FOR

STUD.TECHN. Marius Maastad

Numerical and Experimental Study of the Fred. Olsen Floating Wind Turbine Concept

Background:
Wind industry develops very fast in recent years, moving from onshore to offshore in shallow water and then in deep water. Several floating wind turbine concepts have been proposed and their technological feasibility has been demonstrated with successful prototype testing of Hywind in Norway, WindFloat in Portugal and other concepts in Japan. Cost reduction is a main challenge for developing offshore wind turbines. In shallow water, offshore wind technology based on bottom-fixed foundations prevails. When the water depth reaches 60-100m, a floating wind turbine might be economically feasible.

As we know, spar floating wind turbines (like Hywind) have a large draft and can be only deployed in relatively deep water. Fred. Olsen Ocean proposed an innovative floater design for offshore wind turbines in shallow/intermediate waters. It essentially consists of a low-draft central spar, connected via pre-tensioned cables to a surface ring pontoon (torus). A catenary mooring system with fairlead connections at the torus was considered. Heaving plates attached to the torus for motion reduction were also suggested. Illustrative experimental tests in a small wave tank have been carried out and accordingly preliminary numerical simulations using a Morison-type model in the code 3DFLOAT were performed. In order to further develop this concept, hydrodynamic load and motion characteristics need to be understood. In particular, the whole structure has a relatively small mass and it may have resonant motions under the first-order wave excitation loads, which will induce significant structural responses in its components. Moreover, the torus has a large diameter and a small cross-section. When the floating wind turbine has large pitch motions in waves, the torus may experience water exit and entry problems.

The student Marius Maastad did a preliminary hydrodynamic test of this concept in the small towing tank at NTNU during his project work in the spring semester of 2016. In this thesis work, Marius will focus on the numerical modelling of this concept in 3DFLOAT using a potential flow theory-based model and the comparison of motion responses against the experimental measurement. Based on this comparative study, he will also do a preliminary design check considering the fatigue and ultimate limit states and give recommendations for design improvements.

The student will be provided the guidance on the use of the HydroD and the 3DFLOAT software.

Assignment:
The following tasks should be addressed in the thesis work:

1. Literature review on the fundamental theories that are relevant for coupled dynamic analysis of floating wind turbines, including hydrodynamics of floating structures with focus on potential flow theory, dynamic analysis of rigid-body motions and structural responses, and in addition aerodynamics of wind turbines.

2. Finalize the data processing related to the model test that were carried out during the project work and prepare the results from decay tests and regular wave tests. Upscale the results to full-scale for the comparison with the numerical results. Assess the uncertainties in the model test and give possible improvements for future test.

3. Improve the hydrodynamic model in HydroD that was developed during the project work and develop the new models with heave plates. Understand the importance of the diffraction/radiation effects of the torus and the difference between the Morison-type and the potential flow theory-based models. Prepare the input data for the numerical model in the time-domain code 3DFLOAT.

4. Based on the preliminary 3DFLOAT model, develop a new model that is consistent with the dimensions and parameters that were considered in the model test. Equivalent viscous damping from the spar, torus and heave plates and equivalent mooring stiffness should be determined and considered in the numerical model. Compare the decay test results (including natural periods of rigid-body motions and linear/quadratic damping), calibrate the damping coefficients in the numerical model.

5. Perform numerical simulations and compare the numerical and experimental results for regular wave cases. Discuss the accuracy of the numerical models (including both the potential flow theory-based and the Morison-type models) and possible reasons for the discrepancies. Discuss separately for the small and large wave height cases.

6. Based on the developed and calibrated numerical models in 3DFLOAT, perform a preliminary design check considering both the fatigue limit state (FLS) and ultimate limit state (ULS), with focus on the tower structure. FLS design check should be considered using a set of representative sea states, while ULS design check can be considered for selected extreme sea states.

6. Report and conclude on the investigation. Make recommendations for future work on design changes/improvements and nonlinear hydrodynamic and response analysis of this concept.

In the thesis the candidate shall present his personal contribution to the resolution of problem within the scope of the thesis work.

Theories and conclusions should be based on mathematical derivations and/or logic reasoning identifying the various steps in the deduction.

The candidate should utilize the existing possibilities for obtaining relevant literature.

The thesis should be organized in a rational manner to give a clear exposition of results, assessments, and conclusions. The text should be brief and to the point, with a clear language. Telegraphic language should be avoided.

The thesis shall contain the following elements: A text defining the scope, preface, list of contents, summary, main body of thesis, conclusions with recommendations for further work, list of symbols and acronyms, reference and (optional) appendices. All figures, tables and equations shall be numerated.

The supervisor may require that the candidate, in an early stage of the work, present a written plan for the completion of the work. The plan should include a budget for the use of computer and laboratory resources that will be charged to the department. Overruns shall be reported to the supervisor.

The original contribution of the candidate and material taken from other sources shall be clearly defined. Work from other sources shall be properly referenced using an acknowledged referencing system.

The thesis shall be submitted electronically in DAIM:

- Signed by the candidate
- The text defining the scope included
- Codes and/or drawings which cannot be inserted in the thesis file should be organized in a separate zip file.

Zhen Gao
Supervisor

Deadline: 22.12.2016

Preface

This Master's thesis is written by Marius Berg Maastad, in collaboration with NTNU and Fred. Olsen Ocean. This Master's thesis was carried out during the fall semester of 2016.

The content of this Master's thesis was originally an idea that Fred Olsen came up with two years ago. The project has been on hold for six months, and this Master's thesis, combined with the project thesis, is a continuation of their work. The idea was to create a floating wind turbine that included features from already known designs, with the intention of building a wind turbine with all the advantages. The idea was for me fascinating since I have an interest within marine hydrodynamics, structural engineering, and green technology.

This thesis is written for a student who has knowledge within marine dynamics and marine structures.

Trondheim, December 21, 2016

Marius Berg Maastad

Marius Berg Maastad

Acknowledgment

I would like to thank my supervisor Zhen Gao for the extraordinary help during the semester. He has always been available at the office or by email, to give me quick and very helpful answers. He has also motivated and helped me in a structural manner throughout the semester with an organized plan, making it very easy for me to progress between our meetings. I would not have completed this thesis without his knowledge and his eager to help.

I would also like to thank Fred. Olsen Ocean, especially Jonas Sjolte and Gaute Tjensvoll, in their, follow up throughout the semester. They have been available for questions and counseling every week and given me motivation for delivering an excellent report. Without their help, I would not have achieved this result.

Jacobus Bernardus de Vaal and Tor Anders Nygaard at IFE also deserves special thanks for their help in developing the software 3DFloat and answering questions throughout the semester.

I would, also, thank my fellow students, friends, professors and family in the discussion of theory, results, and proofreading of the report.

M.B.M

Abstract

In this Master's thesis the numerical model designed by Fred. Olsen (FO) is improved, and a long-term analysis for design checks is performed.

The hydrodynamic loads for the numerical model were initially based on Morison's formulation, while the hydrodynamic loads for the improved model are based on Linear Potential Theory (LPT) formulation. The Morison's and numerical LPT model are judged according to a comparison study with experimental results. The experimental results are valid for heave motions, while results for pitch motions are questionable. This is due to the inadequate measurement set up, during the experiment. The Morison's formulation gives a poor representation of the experimental results. An LPT formulation is, in general, a better choice. The latter results in an adequate representation of the heave motions, while the description of the pitch motions is unsatisfactory. The natural periods for linear and nonlinear motions are, respectively, 3.4 and 4.4 s for heave, 7.5 and 9.0 s for pitch and 6.9 and 10.6 s for heave with heave plates.

The Fatigue Limit State (FLS) design check requirement is violated. For heave with and without heave plates, the cumulative fatigue damage is 122.9 and 172.4, respectively. The structure is vulnerable for a wave heading of 90 degrees without heave plates, while the case with heave plates is more robust. The large fatigue damage occurs due to the structural natural periods being within the 1^{st} order wave frequency interval.

The Ultimate Limit State (ULS) requirements are, in terms of buckling, violated for all cross-sectional orientations. ULS, in terms of yield, is only satisfied designed for the orientation which is not affected by the wind- and wave- induced bending loads.

A re-design of the foundation is recommended for future work, to change the structural natural periods and enhance the hydrodynamic performance.

Sammendrag

I denne masteroppgaven er den numerisk modellen, designet av Fred. Olsen (FO), forbedret og langsiktig analyser utført.

De hydrodynamiske belastningene for den numeriske modellen var opprinnelig basert på Morison's formulering, mens hydrodynamiske belastninger for den forbedrede modellen er basert på lineær potensiel teori (LPT) formuleringen. Den numeriske modellen er vurdert etter et sammenligningsstudie med eksperimentelle resultater. De eksperimentelle resultatene er gyldig for hiv-bevegelser, mens resultatene for stamp er tvilsomme. Dette er på grunn av et dårlig måleoppsett, under de eksperimentelle forsøkene. Morison's formulering gir en dårlig representasjon av de eksperimentelle resultatene. En LPT formulering er generelt et bedre valg. Den sistnevnte formuleringen resulterer i en akseptabel representasjon av hiv-bevegelser, mens beskrivelsen av stampebevegelser er utilfredsstillende. Egenperiodene for lineære og ikke-lineære bevegelser er henholdsvis 3.4 og 4.4 s for hiv, 7.5 og 9.0 s for stamp og 6.9 og 10.6 s for hiv med hivplater.

Utmattingstilstandens (FLS) design krav er brutt. For strukturen med og uten hiv-plater, er den kumulative utmattingsskaden, 122.9 og 172.4, respektivt. Strukturen er sårbar for en relativ bølgeposisjon på 90 grader uten hiv-platene, mens med hiv-plater er strukturen mer robust. De store utmattingsskadene oppstår på grunn av at de strukturelle egenperiodene ligger i første ordens bølgefrekvensen intervall.

Bruddgrensetilstandens (ULS) design krav for knekking er brutt for alle tverrsnittsretninger. ULS krav for flyting er bare tilfredsstilt for tverrsnittsretningen som ikke er berørt av vind- og bølgeinduserte bøyelaster.

Et nytt design av fundamentet er anbefalt for videre arbeid, for å endre de strukturelle egenperiodene og forbedre de hydrodynamiske egenskapene.

Contents

1 Introduction 1

1.1 Fred. Olsen OFWT Novel Concept . . . 2

1.2 Previous Research . . . 4

1.3 Objectives . . . 5

1.4 Limitations . . . 5

1.5 Approach . . . 5

1.6 Scope and Structure of the Report . . . 6

2 Theoretical Background 9

2.1 Environmental Conditions . . . 9

2.1.1 Ocean Waves . . . 10

2.1.2 Ocean Wind . . . 12

2.2 Hydrodynamic Loading . . . 12

2.2.1 Hydrostatic Problem . . . 13

2.2.2 Linear Potential Theory . . . 14

2.2.3 Hydrodynamic Problem . . . 16

2.2.4 Nonlinear Hydrodynamic Loading . . . 22

2.3 Aerodynamic Loading . . . 24

2.3.1 Blade Element Momentum . . . 24

2.3.2 Generalized Dynamic Wake . . . 26

2.3.3 Unsteady BEM model . . . 27

2.3.4 Drag on tower . . . 29

2.4 Mooring Lines Loading . . . 29
2.5 Structural Loading . . . 30
2.5.1 Nonlinear Beam Element Theory . . . 31
2.5.2 Inertia and Damping Loads . . . 32
2.6 Motions . . . 34
2.6.1 Equation of Motion in Frequency- and Time-Domain . . . 35
2.6.2 Time - Integration: HHT- α method . . . 37
2.7 Time-Domain Response Analysis . . . 38
2.7.1 Rigid Body Resonant Frequencies . . . 39
2.7.2 Flexible Body Resonant Frequencies . . . 40
2.7.3 Coupling . . . 40
2.8 Design Checks . . . 41
2.8.1 Fatigue Limit State . . . 42
2.8.2 Ultimate Limit State . . . 44

3 Full-Scale and Model-Scale Model Presentation 47
3.1 Presentation of Models . . . 47
3.1.1 Full-Scale Numerical Dimensions . . . 48
3.1.2 Experimental Dimensions . . . 49
3.2 Tank Facilities . . . 50
3.3 Post-Processing of Experimental Results . . . 51
3.4 Problems and Observations for the Experimental Model . . . 52

4 Numerical Modeling 53
4.1 Software Flowchart . . . 53
4.2 Environmental Representation . . . 55
4.3 Hydrodynamic Formulation . . . 55
4.3.1 Morison’s Formulation . . . 55
4.3.2 Linear Potential Theory Formulation . . . 56
4.3.3 Determination of Constant Hydrodynamic Coefficients . . . 60
4.4 Aerodynamic Formulation . . . 61

4.5 Mooring Line Formulation 62
4.6 Structural Formulation 63
4.7 Response Formulation 64
  4.7.1 Equation of Motion 64
  4.7.2 Design Checks 64
4.8 Summary 65

5 Comparison of Numerical Morison's Model and Experimental Model 67
5.1 Decay Test 68
  5.1.1 Heave Nonlinear 68
5.2 Regular Wave Test 69
  5.2.1 Case 1 - Linear 70
  5.2.2 Case 2 - Semi linear 71
  5.2.3 Case 3 - Nonlinear 71
5.3 Discussion 73

6 Comparison of Numerical LPT Model and Experimental Model 75
6.1 Decay Tests 76
  6.1.1 Heave 76
  6.1.2 Pitch 79
  6.1.3 Heave with Heave Plates 81
  6.1.4 Updated Natural Periods 83
  6.1.5 Discussion 83
6.2 Regular Wave Test 86
  6.2.1 Case 1 - Linear 86
  6.2.2 Case 2 - Semi Linear 87
  6.2.3 Case 3 - Nonlinear 89
  6.2.4 Case 4 - Nonlinear with Heave Plates 91
  6.2.5 Discussion 93
6.3 RAO 95
  6.3.1 Wave Height 1 m 96

6.3.2 Wave Height 2 m . . . 97
6.3.3 Wave Height 3 m . . . 98
6.3.4 Discussion . . . 99
6.4 Discussion Summary . . . 102

7 Fatigue Limit State Design Check **105**
7.1 Definition of Reference Frame . . . 105
7.2 20-Year Cumulative Fatigue Damage . . . 107
7.2.1 Without Heave Plates . . . 107
7.2.2 With Heave Plates . . . 109
7.3 Most Probable Sea State Study . . . 110
7.3.1 Without Heave Plates . . . 111
7.3.2 With Heave Plates . . . 116
7.4 Comparison . . . 120
7.4.1 Annual and 20-Year Fatigue Damage . . . 120
7.4.2 Spectrum . . . 120
7.4.3 1-Hour Cumulative Fatigue Damage . . . 122
7.5 Discussion . . . 123

8 Ultimate Limit State Design Check **127**
8.1 Definition of Reference Frame . . . 127
8.2 Checks . . . 128
8.2.1 Without Heave Plates . . . 129
8.2.2 With Heave Plates . . . 130
8.3 Discussion . . . 131

9 Conclusions and Recommendation for Future Work **133**
9.1 Recommendations for Future Work . . . 134
9.1.1 Design of the Floater Foundation . . . 134
9.1.2 Improvement of the Experimental Results and the Experimental Model . . . 135
9.1.3 Software and Numerical Modeling . . . 137

A Acronyms **139**

B Design Check for Buckling of Shells **141**
B.1 Buckling Modes 141
B.2 Method for Buckling Design Check 142

C Previous Work **145**
C.1 Experimental and Numerical Dimensions 145
C.1.1 Froude Scaling 146
C.2 Establishment of Scaling Factor 146
C.3 Hydrostatic Stability During Operation and Storm 147
C.4 Tank Facilities and Experimental Setup 147

D Software Background **151**
D.1 GeniE and HydroD (WAMIT) 151
D.2 3DFloat 154
D.3 Matlab 158
D.3.1 Import from Experimental and Numerical Tests 159
D.3.2 Comparison 159
D.3.3 Design Checks 160
D.4 Drag Forces for Morisons Representation and LPT Representations 160
D.5 Added Mass at Infinite Frequency 161
D.6 Determination of Coefficients 162
D.6.1 Hydrodynamic Coefficients 162
D.6.2 Structural Coefficients 164

E Comparison Between Numerical Morison Model and Experimental Model **169**
E.1 Decay 169
E.2 Regular wave 170

F Comparison Between Numerical LPT Model and Experimental Model **175**
F.1 Linear Decay 175
F.2 NonLinear Decay 177

F.3 Regular Wave 180

G Verification of Computational Damage **187**

Bibliography **191**

List of Figures

1.1 FO OFWT concept 3

1.2 Model usage for the scope of the report 6

2.1 Spectrum and irregular wave (Taken from [21]) 11

2.2 Definition of a floating structure within a boundary (Taken from [43]) 15

2.3 Illustration of radiation and diffraction problem (Taken from [21]) 17

2.4 Submerged torus 22

2.5 Slamming over torus 23

2.6 Heave plates 24

2.7 Induced velocities and loads according to BEM theory (Taken from [22]) 25

2.8 Unsteady BEM model (Taken from [22]) 27

2.9 Motions of a moored structure (Taken from [18]) 30

2.10 Co- rotated coordinate system (Taken from [16]) 31

2.11 Degrees of freedom for a floating wind turbine(Taken from [19]) 34

2.12 Relevant excitation frequencies for a floating wind turbine 39

2.13 Damping contribution from rotor 41

2.14 Orientation of coordinate system at tower base, forces and moments during a FLS analysis (based on [7]) 42

3.1 Full-scale numerical model 48

3.2 Experimental model 49

3.3 Experimental model setup (Taken from [32]) 51

4.1 Flowchart of software 54

4.2 GeniE/HydroD model with and without heave plates 58
4.3 Mooring line formulation of the numerical model 62

5.1 Heave nonlinear decay analysis done by Fred. Olsen 69
5.2 Comparison of case 1 70
5.3 Comparison of case 2 71
5.4 Comparison of case 3 72

6.1 Linear decay heave motions 77
6.2 Nonlinear decay heave motions 78
6.3 Linear decay pitch motions 79
6.4 Nonlinear decay pitch motions 80
6.5 Linear decay heave motions with heave plates 81
6.6 Nonlinear decay heave motions with heave plates 82
6.7 Comparison of case 1 87
6.8 Comparison of case 2 88
6.9 Detailed comparison case 2 88
6.10 Comparison of case 3 90
6.11 Detailed comparison of case 3 90
6.12 Comparison of case 4, with heave plates 92
6.13 Detailed comparison of case 4, with heave plates 92
6.14 RAO for wave height 1 m 97
6.15 RAO for wave height 2 m 98
6.16 RAO for wave height 3 m 99
6.17 Three different experimental wave cases for heave displacement and sea elevation, picked out from the RAO 100

7.1 Verification of tower base moments 106
7.2 1-hour simulation of stress (F-A) at tower base for wave heading 0 degrees 111
7.3 Spectral analysis of stress at F-A for wave heading of 0 degrees 112
7.4 1-hour simulation of stress (S-S) at tower base for wave heading 0 degrees 114
7.5 Spectral analysis of stress at S-S for wave heading of 90 degrees 115

7.6 1-hour simulation of stress (F-A) at tower base for wave heading 0 degrees, with heave plates . . . 116
7.7 Spectral analysis of stress at F-A for wave heading of 0 degrees, with heave plates . 117
7.8 1-hour simulation of stress (S-S) at tower base for wave heading 90 degrees, with heave plates . . . 118
7.9 Spectral analysis of stress at S-S for wave heading of 90 degrees, with heave plates . 119

8.1 Reference frame for ULS calculations . . . 128

9.1 Adjustment for future work of the current floater foundation . . . 135
9.2 Adjustment of experimental accelerometers setup . . . 136
9.3 Two body system of FO concept . . . 138

B.1 Buckling modes (Taken from [4]) . . . 142

C.1 Overturning moment vs restoring moment for operation and storm . . . 147
C.2 Experimental model setup (Taken from [32]) . . . 148

D.1 GeniE models with and without heave plates . . . 152
D.2 HydroD models with and without heave plates . . . 153
D.3 3DFloat model with and without heave plates . . . 158
D.4 Mean difference between experimental and numerical motions for constant hydrodynamic coefficients . . . 164
D.5 Regular wave test of the first numerical model . . . 165
D.6 Mean error between numerical and experimental acceleration for the different cases167
D.7 Numerical results with usage of α equal to 0.016, compared with experimental results . . . 167

E.1 Nonlinear heave decay a nalysis done by Fred. Olsen . . . 169
E.2 Comparison of case 1 . . . 170
E.3 Comparison of case 2 . . . 171
E.4 Comparison of case 3 . . . 172
E.5 Comparison of case 4 . . . 173

E.6 Comparison of case 5 174

F.1 Linear heave decay motions 176
F.2 Linear pitch decay motions 176
F.3 Linear heave decay motions with heave plates 177
F.4 Nonlinear heave decay motions 178
F.5 Nonlinear pitch decay motions 178
F.6 Nonlinear heave decay motions with heave plates 179
F.7 Comparison of case 1 180
F.8 Comparison of case 2 181
F.9 Comparison of case 3 182
F.10 Comparison of case 4 183
F.11 Comparison of case 5 184
F.12 Comparison of case 6, with heave plates 185

G.1 Fatigue Model 188
G.2 Moment about y - axis for measured and calculated values 189

List of Tables

2.1 Degree of Freedom 34
2.2 Variables (Found in [2]) 44
2.3 Action factors for design loads in ULS (Found in [6]) 45

3.1 Some full-scale structural dimensions 49
3.2 Experimental model dimensions 50

4.1 Definition of hydrodynamic coefficients for Morison's formulation 56
4.2 Parameters for GeniE calculations without heave plates 57
4.3 Hydrostatic coefficients 58
4.4 Wave cases in HydroD 59
4.5 Constant hydrodynamic coefficients 61
4.6 Structural damping coefficients 64

5.1 Natural periods for the FO OFWT concept (Taken from [32]) 68

6.1 Updated natural periods 83
6.2 Regular wave cases for RAO comparison 96

7.1 Definition of local in global coordinate system 106
7.2 Fatigue damage at tower base, for structure without heave plates 108
7.3 Fatigue damage at toer base, for structure with heave plates 109
7.4 Sea state parameter for case 2 110
7.5 Evaluation of frequencies influencing spectral density 113
7.6 Fatigue damage during 1 hour simulation with wave heading of 0 degrees 113

7.7 Fatigue damage during 1 hour simulation with wave heading of 0 degrees 115
7.8 Evaluation of frequencies influencing spectral density, with heave plates 117
7.9 Fatigue damage during 1 hour simulation with wave heading of 0 degrees, with heave plates 118
7.10 Fatigue damage during 1 hour simulation with wave heading of 90 degrees, with heave plates 119
7.11 Comparison of annual and 20 year cumulative fatigue damage 120
7.12 Comparison of spectral peaks and associated periods with wave heading of 0 degrees 121
7.13 Comparison of spectral peaks and associated periods with wave heading of 90 degrees 122
7.14 Comparison of 1 hour cumulative fatigue damages (F-A) for weave heading of 0 degrees 123

8.1 50- year worst sea state parameters for Norway 5 (Taken from [27]) 129
8.2 Relevant environmental cases for ULS checks (Taken from [27]) 129
8.3 Checks for eight angles between fore and aft, without heave plates 130
8.4 Checks for eight angles between fore and aft, with heave plates 131

C.1 Dimensions of experimental and numerical model 145
C.2 Relationships between model and scale 146
C.3 Tank facility dimensions 148
C.4 Accelerometers description 148
C.5 Full-scale and model-scale mooring stiffness 149

D.1 Default parameters 156
D.2 Changes from default parameters in 3DFloat 156
D.3 Mass coefficient for LPT and Morison’s formulation 161
D.4 Information and input values for the constant hydrodynamic coefficients 163
D.5 Final coefficients for drag and damping 164
D.6 Natural frequencies versus damping ratio 165
D.7 Information and input values for the tuning study 166

G.1 Input and measured values from 3DFloat 187
G.2 Description of parameters 188
G.3 Measured and calculated values from 3DFloat 189

Nomenclature

α	Constant for JONSWAP spectrum
α	Constant for Rayleigh damping
β	Constant for JONSWAP spectrum
β	Constant for Rayleigh damping
χ	Wake skew angle
$\Delta\sigma$	Stress range in a fatigue analysis
η	Body oscillatory motion
γ	Constant for JONSWAP spectrum
γ	Phase angle
$\kappa(t-\tau)$	Retardation function
$\mathbf{a}$	Particle acceleration from the incident velocity potential
$\mathbf{v}$	Particle velocity from the incident velocity potential
$\ddot{\eta}$	Structural acceleration
$\dot{\eta}$	Structural velocity

∇	Displaced fluid volume
ω	Wave oscillation frequency
ω_p	Peak frequency for a wave spectrum
ϕ	Inflow angle
ϕ	Velocity potential
ϕ_0	Incident velocity potential
ϕ_1	Linear velocity potential
ϕ_2	Second order velocity potential
ϕ_3	Third order velocity potential
ϕ_7	Scattered velocity potential
ϕ_D	Diffraction velocity potential
ρ	Density
σ	Empirical parameter in a fatigue analysis
σ_p	Variance for a wave spectrum
σ_{Rd}	Structural design resistance
σ_{Sd}	Design stress
$\mathbf{B}_{\text{structure}}$	Structural damping matrix
$\mathbf{K}_{\text{global}}$	Global stiffness matrix
$\mathbf{M}_{\text{global}}$	Global mass matrix
$\mathbf{M}_{\text{structure}}$	Structural mass matrix

$\mathbf{R}_{\text{ext}}$	External forces from environmental loads
$\mathbf{R}_{\text{int}}$	Internal reaction force due to external loading
θ	Orientation angle
$\theta_{\text{wing}-\theta_0}$	Difference between the rotation of blad and the angle where the blade is deepest into the wake
φ_j	Unit-amplitude radiation potential for translation j
φ_R	Radiation velocity potential
ζ_a	Wave amplitude
ζ_i	Damping ratio
A	Area
A_∞	Added mass at $\omega \to \infty$
A_{kj}	Added mass for motion in k contribution in j
A_{nn}	Added mass in n degree of freedom
B_1	Linear damping from mooring lines
B_2	Second order damping from mooring lines
B_{linear}	Linear damping
$B_{\text{quadratic}}$	Quadratic damping
B_{kj}	Hydrodynamic damping for motion in k contribution in j
C_D	Drag coefficient
C_M	Mass coefficient

C_{33}	Water plane stiffness
C_{44}	Roll radii stiffness
C_{55}	Pitch radii stiffness
C_{nn}	Stiffness in n degree of freedom
$D_{1\text{ year}}$	Cumulative fatigue damage 1 year
$D_{20\text{ year}}$	Cumulative fatigue damage 20 year
$F(\omega)$	Frequency dependent excitation force
F^{D}	Diffraction force
F^{FK}	Froude kriloff force
I_y	Moment of inertia about y- axis
I_z	Moment of inertia about z- axis
K	Stiffness matrix
M_y	Bending moment about y- axis
M_z	Bending moment about z- axis
M_{nn}	Mass in n degree of freedom
N	Number of oscillations in a fatigue analysis
N_x	Axial force
p_a	pressure
p_N	Normal pressure on a blade
p_T	Transverse pressure on a blade

S_{0B}	Wetted body
T_{nn}	Natural period in n degree of freedom
t_{ref}	Empirical parameter in a fatigue analysis
V_0	Incident wind velocity
V_{rel}	Relative incident wind velocity
V_{rot}	Rotational incident wind velocity
W	Wake
W_{int}	Intermediate velocity value
W_{qs}	Induced velocities
X_{LF}	Low frequency
X_{WF}	Wave frequency
$Y(\omega)$	Response amplitude operator
Z_{COB}	Center of buoyancy
Z_{COG}	Center of gravity
A	Area
a	Induced velocity factor
a	Empirical parameter in a fatigue analysis
a’	Induced rotational factor
B	Blades
D	Drag force

dr	Longitudonal thickness of a blade element
g	Gravitational constant
h	water depth
i	vectorial horizontal direction
j	vectorial transverse direction
k	Wave number
k	vectorial vertical direction
L	Lift force
M	Moment
m	Empirical parameter in a fatigue analysis
n	Vector from a body
p	pressure
r	Distance from hub to a selected element
S	Wave spectrum
T	Torque
U	Constant wind speed
u’	Fluctuating wind speed
V	Volume
x	horizontal direction in a Cartesian coordinate system
y	transverse direction in a Cartesian coordinate system

z	vertical direction in a Cartesian coordinate system

Chapter 1

Introduction

Today, three fourth of the produced power comes from fossil fuels [41]. The remaining one fourth is a combination of renewable and nuclear energy. The European Union (EU) and Organisation for Economic Co-operation and Development (OECD)[14], are continuously discussing the future goals for making the world a greener place. The target, set by the European Comission[14], is to cut 40 % in greenhouse gas emissions, 27 % share of the total energy production shall be renewable, and the energy efficiency shall increase with 27 %. This framework should be accomplished within 2030, and all parties have a joint responsibility of achieving these goals.

The problematic regarding green power production comes down to whether it is economically feasible or not. The Wind Turbine (WT) industry has shown that green technology is economical feasible, where the WT industry had in 2008 the world's fastest growing rate of energy production, on a percentage basis [31]. Onshore WT is a well established and modern industry, due to operational advantages, simple designs and the high potential magnitude of generated power. The WT industry sees its limitations as large open fields close to urban cities are filled up. The Offshore Wind Turbine (OWT) industry is another aim to solve the demanding energy consumption problem.

OWT industry has continued the design from the onshore industry, which resulted in the bottom-fixed structure called monopile. The majority of the current structures has the monopile foundation, which is feasible to install up to 30 meters[39]. These structures have become popular due to its low costs, reliability, and simplicity. The OWT industry is, besides, popular since sites with water depth below 30 meters are close to urban cities.

When the shallow waters are filled up with bottom fixed structure becomes Offshore Floating Wind Turbine (OFWT) more relevant. Many sites with water depth greater than 30 m are close urban cities. For instance, the potential for offshore energy outside the west coast of USA is assumed to be more than 900 GW [44], where the water depth is larger than 30 m[8].

The problematic regarding the design of a floating structure that has a high reliability, low cost and is easy to operate is critical to address. The O & G industry has shown that it is plausible to design a floating structure with a minimum response, which is the driving factor for developing OFWT. Today, it exists well established floating wind turbine designs for larger water depth that are reliable, has a low cost and is easy to operate. The spar foundation, Hywind, developed by Statoil is the most familiar deep water WT foundation. OFWT foundation for intermediate water depths is questionable, regarding the optimal design and the associated operation. The Tension-Leg-Platform(TLP) and barge foundation is the most well-known foundation for intermediate water depths, in addition to hybrid concepts that tries to take advantages for all the previous mentioned designs.

This Master's thesis will consider a hybrid concept, developed by Fred. Olsen Ocean, that will operate at a water depth of 70 m. In the next sections, the concept will be presented.

1.1 Fred. Olsen OFWT Novel Concept

The Fred Olsen Offshore Floating Wind Turbine (FO OFWT) concept had been an ongoing project for two years when this Project and Master's thesis started. Fred. Olsen (FO) wanted to design an OFWT that handled the hydrodynamical loads, had a low material weight and was designed for making marine operations easy. The FO OFWT is a hybrid concept that tries to use the advantage from buoyancy, mooring lines and ballast. The FO OFWT concept presented in Figure 1.1 is designed for intermediate water depths.

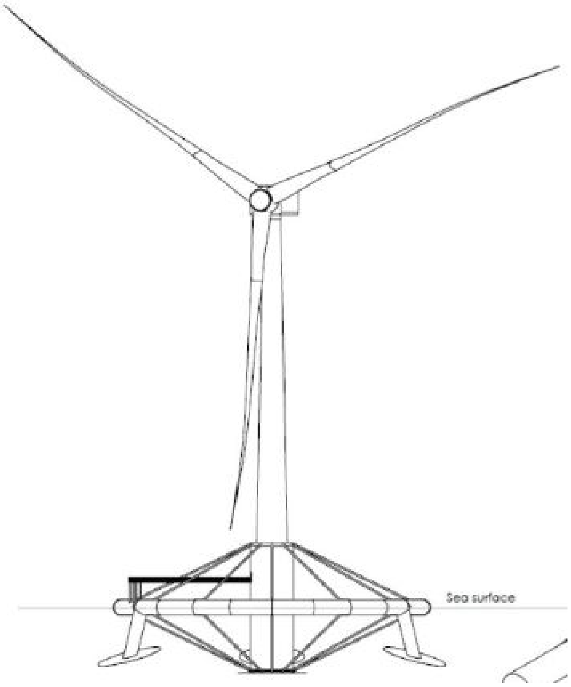

Figure 1.1: FO OFWT concept

It is seen that the foundation consists of a torus and column, interconnected with pre-tensioned cables for the torus to contribute to the structural stability. The torus is temporarily filled with air, and the column is filled with ballast. Three heave plates are also connected to the torus, which reduces the general acceleration of the structure. The rotor connected has the possibility to generate 5MW.

FO wanted to have a reliable numerical time-domain solver that could be used for development of OFWT. FO was early in the design phase introduced to the software 3DFloat. FO did not know the applicability of 3DFloat but performed numerical calculations nevertheless. The advantage of using the initial version of 3DFloat was that structural dimensions could easily be changed and analyzed numerically. This possibility was only an advantage if the numerical model calculated the structural responses correctly.

FO understood that the numerical time-domain solver produced strange results, and they decided to design an experimental model. This model is described into further detail in Chapter 3. The design of the experimental model had the purpose of verifying the numerical calculations and did not follow general scaling theory consistently. This leads to the fact that the experimental model was not meant for an optimal design and detailed comparison with the full-scale numerical model, but just for verification.

1.2 Previous Research

Large scale OFWT was introduced in 1972 [23], but it took approximately 20 years before more research within this field was initialized. From the year 2000 to today has numerous papers regarding OFWT been carried out, for various foundation types.

The initial programs used in OWT coupled hydrodynamic and aerodynamic simulators was meant for analyzation of monopile structures. These structural motions used an aero-servo-elastic simulator that simplifies the hydrodynamic load [29, 28]. The hydrodynamic loads are calculated from the Morison's theory that neglects the effects of potential effects, i.e. the inherited free surface effect from wave radiating from the structure. The Morison's theory is applicable for a cylinder with a small diameter compared to the wavelength, piercing the sea surface vertically. The theory uses the linear analytical solution by [35] to simplify Morison's diffraction term, seen in Section 2.2.3.2. This made the theoretical implementation to the software applicable for fixed bottom structures, such as monopiles.

It was not before 2006, from [25] combined with the work done by NREL, that a reliable aero-hydro-servo-elastic simulator was established for determining the hydrodynamic forces using either Morison's or potential theory. This made it possible to perform numerical simulations for large-scale OFWT with large volumes.

There have been various programs that establish the coupling loads for aerodynamic and hydrodynamic loads, where SIMO/RIFLEX + Aerodyn from [26] is the most familiar one (for the author since it is developed by SINTEF). Another aero-hydro-servo-elastic simulator developed by ”Institutt for energiteknikk” (IFE) [40], named 3DFloat, is also known for reliable fully coupled aero- and hydrodynamic calculations. Both simulators use results from WAMIT [43] which solves the potential effects Morison's theory neglects.

1.3 Objectives

This Master's thesis will continue the work done by Fred Olsen on the novel OFWT concept. This Master's thesis aims to:

1. Solve the hydrodynamic problem the FO OFWT concept faces.
2. Design a numerical model that corresponds with the experimental model.
3. Perform Fatigue Limit State (FLS) design check
4. Perform Ultimate Limit State (ULS) design check

1.4 Limitations

The limitation for this Master's thesis is the incorrectly scaled experimental model, and the linear assumption using LPT theory for establishing the hydrodynamic loads. Another limitation is the experimental measurement system which the comparison study is based on.

1.5 Approach

The approach for solving the hydrodynamic problem is basic knowledge about the applicability of Morison's and LPT theory, to understand which theory that shall be used for specified floater foundations. The hydrodynamic problem is solved by using a combination of Morison's and LPT theory, where the hydrodynamic coefficients are established using the core program WAMIT (implemented in DNV HydroD). The implementation of the hydrodynamic theory is verified with experimental tests performed by the author, for decay and regular waves.

The numerical model is created on behalf of previous work done by FO, and the experimental model. Various coefficients for determining hydrodynamic loads are established from DNV recommended practice.

The FLS and ULS design check are verified with requirements from the DNV recommended practice. The program 3DFloat calculates the numerical loads used in FLS and ULS study.

1.6 Scope and Structure of the Report

The scope of this Master's thesis will give a through background theory, before the listed objectives are solved. Figure 1.2 illustrates the scope of this Master's thesis:

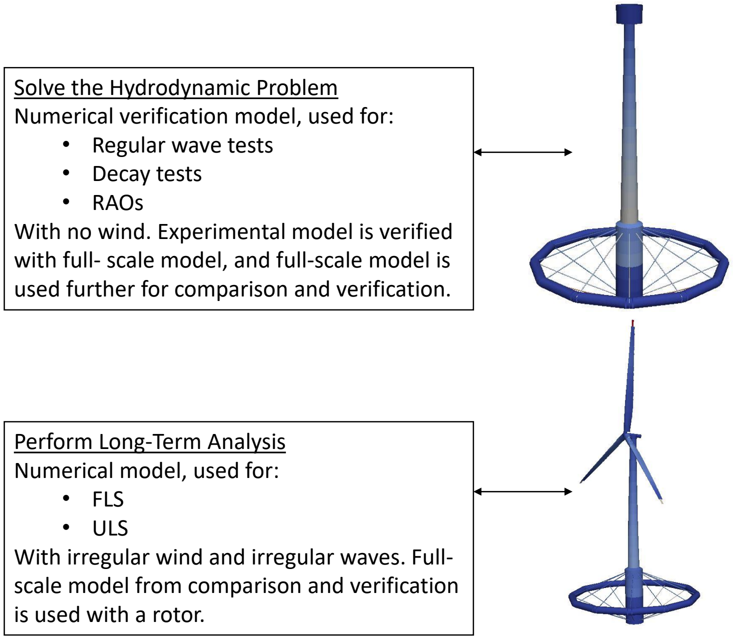

Solve the Hydrodynamic Problem

Numerical verification model, used for:

- Regular wave tests
- Decay tests
- RAOs

With no wind. Experimental model is verified with full- scale model, and full-scale model is used further for comparison and verification.

Perform Long-Term Analysis

Numerical model, used for:

- FLS
- ULS

With irregular wind and irregular waves. Full-scale model from comparison and verification is used with a rotor.

Figure 1.2: Model usage for the scope of the report

This figure shows that a simplified numerical model is used for solving the hydrodynamic problem the experimental model faces. Also, the figure demonstrates that design checks and further analysis use the fully coupled aerodynamic- hydrodynamic numerical model.

This Master's thesis consist of nine chapters, to solve the presented problems. This Master's thesis has the following setup:

Chapter1 This chapter gives an introduction to renewable energy, wind turbine industry, offshore wind turbine industry, the FO OFWT novel concept, objectives, limitations, approach and the structure of the report.

Chapter 2 This chapter gives a thorough general theoretical background for an aero-hydro-servo-elastic simulator. The chapter is setup by identifying all external loads (environmental loads, hydrodynamic loads etc.), all internal loads, (Mass, stiffness, damping, etc.) before the equation of motion is established for a general OFWT turbine. The response formulation is covered in the latter part of this chapter.

Chapter 3 This chapter includes the necessary information about previous work and information about the numerical and experimental model for further analysis. Visual observation and problems from the experimental tests will also be mentioned.

Chapter 4 This chapter gives a software background and how the FO OFWT concept is modeled numerically in the software. A description of the software flowchart will also be outlined.

Chapter 5 This chapter contains a numerical and experimental comparison study, where the hydrodynamic loads are calculated using Morison's theory. The comparison study contains decay and regular wave tests.

Chapter 6 This chapter contains a numerical and experimental comparison study, where the hydrodynamic loads are calculated using LPT theory. The comparison study contains decay, regular wave, and RAO tests.

Chapter 7 This chapter studies whether the structure is designed according to the FLS design check.

Chapter 8 This chapter studies whether the structure is designed according to the ULS design check.

Chapter 9 This chapter contains the overall conclusion and recommendation for future work.

Chapter 2

Theoretical Background

Novel concepts, such as the FO OFWT concept, requires a general understanding of the underlying theory to create a numerical model that corresponds with real-time motions. Existing theory must be applied with care since novel concepts do not follow standard designs which well-known theory is applied for. The importance of understanding the general theory and its limitations are vital in the future analysis of the FO OFWT concept. This chapter will give a thorough introduction to the theory behind the software and what the limitations are.

The literature study investigates the necessary information for establishing the Equation of Motion (EOM). The EOM can be split into external and internal loads. The external loads consist of the environmental loads, where the coupled hydrodynamic and aerodynamic loads will be investigated in detail. The hydrodynamic loads can be established either by Morison's theory or LPT, which will be outlined. The second part of establishing the EOM is the internal loads, which also will be outlined. The latter part of this chapter will inform the reader of coupled dynamic analysis of rigid-body motion and structural response for a floating wind turbine.

2.1 Environmental Conditions

The environmental parameters influencing an OFWT are determined from a specific site. The waves, wind, and water depth are the parameters of interest in this thesis.

2.1.1 Ocean Waves

The environmental waves can be approximated as linear and nonlinear. Linear waves (First order) are the most probable waves and have a wave period interval between 5 and 20 seconds for most locations. The nonlinear waves are characterized as waves with low and high frequencies, which is outside the 1^{st} order wave frequency interval.

Linear irregular waves are the best linear representation of real ocean waves. These linear waves are two-dimensional and are based on linear conditions. The linear condition makes it possible to formulate irregular waves from regular waves, through the superposition principle.

Incident regular waves have a constant period, wave height and phase angle propagating at a selected heading angle. A regular incident wave is linear and generated far away. A linear propagating wave in x direction is determined from the velocity potential, described in Section 2.2.2. The velocity potential for a regular wave and the sea elevation for a regular wave follows in Equation 2.1[15].

$$\phi = \zeta_a \frac{g}{\omega} e^{kz} \cos(\omega t - kx + \gamma) \tag{2.1a}$$

$$\zeta = \zeta_a sin(\omega t - kx + \gamma) \tag{2.1b}$$

where ζ_a is the wave amplitude, g is gravity, ω is the wave oscillation frequency, z is the water depth, x is the horizontal distance and γ is the phase angle. The velocity potential describes the sea elevation but it may also describe the water pressure, particle acceleration and more[15].

Irregular waves are connected to a wave spectrum, which is a formulation of wave energy for a specific site. It is illustrated in Figure 2.1.

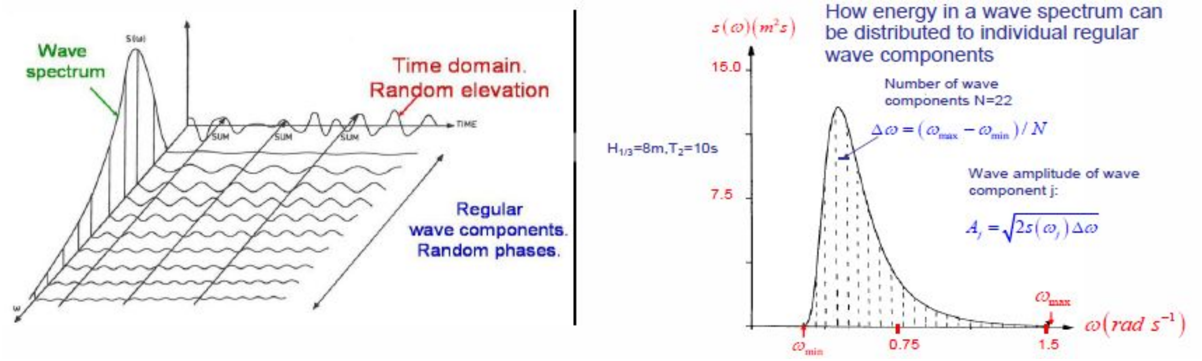
Wave spectrum
S(ω)
Time domain.
Random elevation
TIME
SUM
SUM
SUM
Regular wave components.
Random phases.
w
$s(\omega)(m^2s)$
How energy in a wave spectrum can be distributed to individual regular wave components
15.0
7.5
$H_{1/3}$=8m, T_2=10s
Number of wave components N=22
$\Delta\omega = (\omega_{max} - \omega_{min})/N$
Wave amplitude of wave component j:
$A_j = \sqrt{2s(\omega_j)\Delta\omega}$
ω_{min}
0.75
1.5
ω_{max}
$\omega(rad\ s^{-1})$

Figure 2.1: Spectrum and irregular wave (Taken from [21])

Each frequency for the wave spectrum is associated with a constant wave period and wave height (regular wave), seen from Figure 2.1. The wave spectrum peak is where the site's energy is largest, meaning that a wave with this frequency is the most likely wave within a site. The sea surface is expressed as in Equation 2.2 [21].

$$\zeta = \sum_{j=1}^{N} A_j \sin(\omega_j t - k_j x + \gamma_j) \tag{2.2a}$$

$$A_j = \sqrt{2 \cdot S(\omega)\Delta\omega} \tag{2.2b}$$

where N is the number of frequencies from the wave spectrum.

There are multiple numerical wave spectrums to illustrate different sea conditions. JONSWAP and Torsethaugen spectrums are the most familiar spectrums. JONSWAP is a single peak spectrum which describes waves generated by the wind, while Torsethaugen spectrum takes swell into consideration. The JONSWAP spectrum is described in Eqs. 2.3 - 2.5[21].

$$S(\omega) = \frac{\alpha g^2}{\omega^5} exp\big(-\beta(\frac{\omega_p}{\omega})^4\big)\gamma^{a(\omega)} \tag{2.3}$$

where

$$a(\omega) = exp(\frac{(\omega/\omega_p - 1)^2}{2\bar{\sigma}^2}) \tag{2.4}$$

where

$$\bar{\sigma} = \begin{cases} 0.07, & \omega \leq \omega_p \\ 0.09, & \omega > \omega_p \end{cases} \tag{2.5}$$

where α, β, γ are constants, and ω_p is the peak frequency for the spectrum.

2.1.2 Ocean Wind

The ocean wind is represented by a mean and fluctuating wind speed. The fluctuating change occurs over a long period, which means that the wind frequencies are denoted as low frequencies.

The mean wind speed arises directly from the steady-state wind. This formulation only, is an unrealistic wind to the ocean wind problem. It is a formulation that reduces the simulation time but gives less accurate results. The combination of mean and fluctuating wind speed is turbulent wind, which varies with time and represents the ocean wind well. Turbulent wind varies additionally within space, and a wind component has, therefore, four components: U(x,y,z,t). A typical formulation of wind speed at a time instant at a selected point in space is described by Equation 2.6[15], where $\bar{U}$ and u' is respectively mean and fluctuating wind speed.

$$U = \bar{U} + u' \tag{2.6}$$

A detailed explanation of wind and the derivation can be seen in lecture notes from Marilena Greco [21].

2.2 Hydrodynamic Loading

The hydrodynamic loading on an OFWT can be split into two problems, hydrostatic and hydrodynamic. The hydrodynamic problem can again be calculated by using two different theories. The hydrodynamic loading rises from potential theory which is described in Section 2.2.2.

2.2.1 Hydrostatic Problem

The first part of the hydrodynamic loading is the hydrostatic problem. The structure is freely floating in calm water in its neutral position, and it is possible by simple calculations to establish hydrostatic properties. The hydrostatic problem solves the stiffness matrix, where C_{33}, C_{44} and C_{55} (and the coupling coefficients) are respectively dependent on water plane area, pitch radii of gyration and roll radii of gyration. The radii of gyration is reliant on the center of buoyancy (z_{COB}).

The resulting hydrostatic matrix for a floating strucutre is shown in Equation 2.7[25].

$$\mathbf{F}^{\text{Hydrostatic}} = -\begin{bmatrix} 0 & 0 & 0 & 0 & 0 & 0 \\ 0 & 0 & 0 & 0 & 0 & 0 \\ 0 & 0 & \rho g A_w & 0 & -\rho g \iint\limits_{A_w} x dA & 0 \\ 0 & 0 & 0 & \rho g \iint\limits_{A_w} y^2 dA + \rho g \nabla z_{\text{COB}} & 0 & 0 \\ 0 & 0 & -\rho g \iint\limits_{A_w} x dA & 0 & \rho g \iint\limits_{A_w} x^2 dA + \rho g \nabla z_{\text{COB}} & 0 \\ 0 & 0 & 0 & 0 & 0 & 0 \end{bmatrix} \eta \tag{2.7}$$

where ρ is the water density, g is the gravitational acceleration, ∇ is the displaced fluid volume when the structure is in its initial position. Stiffness coefficient (3,3), gives a change of force when the structure is displaced. When it is multiplied with the displacement can this be seen as a spring, where stiffness coefficient (3,3) is the spring stiffness. The stiffness coefficients (4,4) and (5,5) illustrates the moments from roll and pitch displacement, and it is additionally important to include the center of buoyancy represented by the last term in coefficients: 4,4 and 5,5. The point of force will change as the center of buoyancy moves.

The stiffness coefficients (3,5) and (5,3) can be set to zero if a structure is symmetric about the y-z plane.

2.2.2 Linear Potential Theory

Linear Potential Theory (LPT) is the basis for understanding fluid dynamics and is necessary for an environmental representation.

The velocity potential, ϕ, describes the fluid within a control volume. The velocity potential gives an understanding of how the pressure within a control volume varies. The velocity potential is based on three fluid properties which must be true [21]:

1. Inviscid: Zero viscosity $\mu = 0$
2. Irrotational: No rotation of the fluid $\omega = 0$
3. Incompressible: Fluid volume does not change, $\nabla \cdot \mathbf{V} = 0$

These assumptions makes it possible to write the velocity of a fluid particle, **V**, as a function of the velocity potential:

$$\mathbf{V} = \nabla\phi = \frac{\partial\phi}{\partial x}\mathbf{i} + \frac{\partial\phi}{\partial y}\mathbf{j} + \frac{\partial\phi}{\partial z}\mathbf{k} \tag{2.8}$$

A direct assumption of potential theory (fluid is incompressible, inviscid and irrotational) is that Laplace's equation is valid. Laplace's equation must be valid within the whole controle volume:

$$\nabla^{\mathbf{2}}\phi = \frac{\partial^2\phi}{\partial x^2}\mathbf{i} + \frac{\partial^2\phi}{\partial y^2}\mathbf{j} + \frac{\partial^2\phi}{\partial z^2}\mathbf{k} = 0 \tag{2.9}$$

Equation 2.8 gives an advantage in determining pressure. From Bernoulli's equation is:

$$p - p_a = -\rho g z - \rho\frac{\partial\phi}{\partial t} - \frac{1}{2}\rho(\nabla\phi)^2 \tag{2.10}$$

where p is pressure in the fluid, p_a is the atmospheric pressure, and z is the position in a Cartesian coordinate system. The pressure is now only dependent on the variable ϕ and the z position, which is an advantage.

To establish a velocity potential that describes the fluid, a boundary problem must be defined. An accurate body value problem solves ϕ further. The next section investigates this.

2.2.2.1 Boundary-Value Problem

The boundary-value problem is approached by water representation. Figure 2.2 describes a freely floating body within a boundary frame, with waves propagating in the x-y plane with an angle β. The Cartesian coordinate system is fixed at a given position, and it is for most cases convenient to place this in the middle of the structure at the MSL.

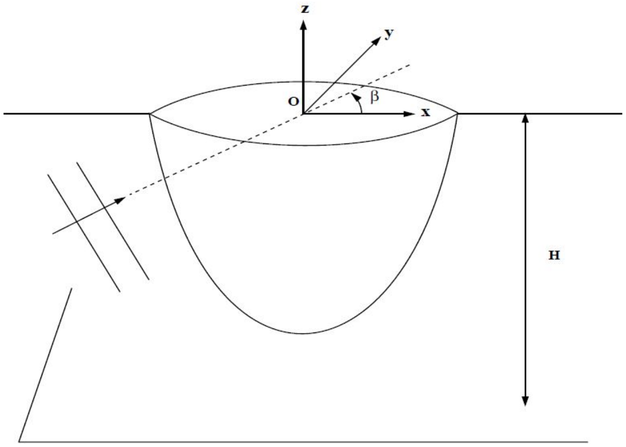

Figure 2.2: Definition of a floating structure within a boundary (Taken from [43])

The boundary consist now of five conditions [21]:

1. Sea - bottom kinematic, $\frac{\partial \phi}{\partial n} = 0$
2. Body kinematic $\frac{\partial \phi}{\partial n} = \mathbf{V_B} \cdot \mathbf{n}$
3. Free - surface kinematic
4. Free - surface dynamic
5. Far field

These five boundary conditions are necessary for obtaining the velocity potential for the control volume. These conditions can be looked up in [15].

2.2.2.2 Limitations

The linear potential theory associated with waves are a simplification to a realistic problem. A velocity potential for higher orders can be represented by:

$$\phi = \phi_1 + \phi_2 + \phi_3.. \tag{2.11}$$

where ϕ_1 is the linear velocity potential, ϕ_2 is the second order velocity potential and further on. The Bernoulli's equation can be expressed for higher order effects. A second order representation is given in Equation 2.12.

$$p - p_a = -\rho g z - \rho \frac{\partial \phi_1}{\partial t} - \rho \frac{\partial \phi_2}{\partial t} - \frac{1}{2} \rho \nabla \phi_1 \cdot \phi_1 \tag{2.12}$$

This representation establishes a pressure within a control volume better, but the complexity increases as well. The complexity increases because it is now needed to solve the second-order velocity potential, ϕ_2, as well.

2.2.3 Hydrodynamic Problem

There are two different ways to analyze the hydrodynamic problem of a floating structure: Linear Potential Theory method (LPT) and Morison's method.This section will give an understanding of both theories, the usage, and its limitations.

2.2.3.1 Linear Potential Flow Theory Formulation

Hydrodynamic forces based on purely Linear Potential Flow Theory (LPT) is often used for large volume structures, due to a constant water plane area. The main characteristic of LPT is that hydrodynamic pressure across a rigid body is integrated and applied at one reference point. It is directly connected to LPT of fluid and the velocity potential. The velocity potential problem for an LPT approach is solved by splitting the velocity potential into two problems: Diffraction and Radiation. This is illustrated in Figure 2.3.

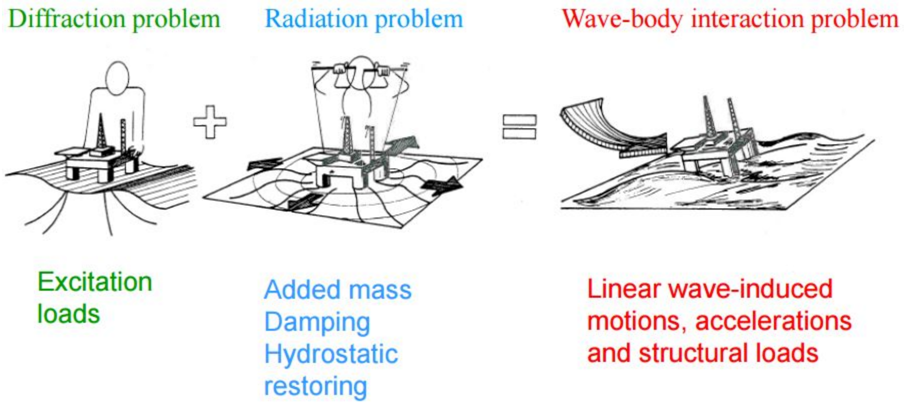
Diffraction problem
Radiation problem
Wave-body interaction problem
+
=
Excitation loads
Added mass
Damping
Hydrostatic restoring
Linear wave-induced motions, accelerations and structural loads

Figure 2.3: Illustration of radiation and diffraction problem (Taken from [21])

The velocity potential describes how a structure penetrates the fluid, how the fluid changes when the structure oscillates and how the fluid changes when incident regular waves are applied to the structure, seen by Figure 2.3. The hydrodynamic load from the LPT approach can, therefore, be presented as in Equation 2.13.

$$F^{\text{Hydrodynamic}} = F^{\text{Diffraction}} + F^{\text{Radiation}} \tag{2.13}$$

2.2.3.1.1 Diffraction

The excitation loads for the diffraction problem depends on the incoming wave velocity potential, ϕ_0, and the disturbed velocity potential, ϕ_7, around the structure. In other words, it depends on how the waves interact with the structure when the structure is fixed. The diffraction potential is often denoted as in Equation 2.14. The velocity potential for a regular wave at finite depth is shown in Equation 2.15a[15].

$$\phi_D = \varphi_0 + \varphi_7 \tag{2.14}$$

$$\varphi_0 = \frac{g\zeta_a}{\omega}\frac{\cosh[k(z+h)]}{\sinh kh}\cos(\omega t - kx) \tag{2.15a}$$

$$\frac{\omega^2}{g} = k\tanh kh \tag{2.15b}$$

where g is the gravity, ζ_a is the wave amplitude, ω is the wave frequency, k is wavenumber (Equation 2.15b), z is the vertical coordinate, and the water depth is h. The same equations can easily be expanded to infinite water depth and with waves of different heading angle [15]. This velocity potential arises from LPT which was described initially in this chapter.

The scattered velocity potential, ϕ_7 can be found from Equation 2.16 [43].

$$2\pi\varphi_7(\mathbf{x}) + \iint_{S_b}\varphi_7(\eta)\frac{\partial G(\eta;\mathbf{x})}{\partial n_\eta}d\eta = -\iint_{S_b}\frac{\partial\varphi_0(\eta)}{\partial n}G(\eta;\mathbf{x})d\eta \tag{2.16}$$

where $\mathbf{x}$ is the Cartesian coordinate, η is the body oscillatory motion in 6 DOFs, n is a unit vector normal to the body boundary and G is the Green Function [11]. This equation is derived from a source method, which is one of the method to establish the scattered velocity potential. As it is seen by the rigth-hand side (RHS) of the equation, the incident velocity potential must be known in order to establish ϕ_7, and often are alternative equations used to reduce computational time.

Further, the excitation force can be determined by integrating the pressure, arising from the diffraction velocity potential, over the mean wetted surface of the structure, see Equations 2.17a-

2.17c [32].

$$F^{\text{Diffraction}}(t) = \int_{S_{0B}} \underbrace{-\rho \frac{\partial \phi_D}{\partial t}}_{\text{Pressure}} dS_{0B} \tag{2.17a}$$

$$= -\int_{S_{0B}} \underbrace{\rho \frac{\partial \varphi_0}{\partial t} dS_{0B}}_{\text{FK-pressure}} - \int_{S_0 B} \underbrace{\rho \frac{\partial \varphi_7}{\partial t} dS_{0B}}_{\text{Diffraction-pressure}} \tag{2.17b}$$

$$\Updownarrow$$

$$F^{\text{Diffraction}}(t) = \mathbb{R}\underbrace{\left[\int_{S_{0B}} -i\omega e^{i\omega t}\rho(\varphi_0 + \varphi_7) n_k dS_{0B}\right]}_{\text{Excition load}} \tag{2.17c}$$

The excitation force from Equation 2.17c is the final result of the diffraction problem.

2.2.3.1.2 Radiation

The radiation potential is found by oscillating the floating body in its six DOFs in calm water. The structure will generate waves because of its motions, and the radiation velocity potential can express these waves. The velocity potential for the radiation problem is often denoted as in Equation 2.18.

$$\phi_R = i\omega \sum_{j=1}^{6} \eta_j \varphi_j \tag{2.18}$$

where η_j is the complex amplitude of the body motion in j direction, and ϕ_j is the unit-amplitude radiation potentials [43]. The unit-amplitude radiation velocity potential must satisfy the same boundary conditions as the general velocity potential from LPT.

Furthermore, it is possible to establish the force that arises from the velocity potential. By utilizing the same method as for the diffraction problem, the radiation force can be presented as per Equation 2.19.

$$F^{\text{Radiation}}(t) = \int_{S_0B} \underbrace{-\rho\frac{\partial \phi_R}{\partial t} n_k}_{\text{Pressure arised from radiation}} dS_{0B}, \tag{2.19}$$

This oscillating force will generate steady-state hydrodynamic forces and moments that are called added mass, A, damping, B, and restoring, C. For a freely floating single body system, these forces and moment are matrices of 6x6, due to 6 DOFs and coupling effects. The relationship between the radiation force and the hydrodynamic forces are given in Equation 2.20[21].

$$F_k^{\text{Radiation}}(t) = \sum_{j=1}^{6} [-A_{kj}\frac{d^2\eta_j}{dt^2} - B_{kj}\frac{d\eta_j}{dt}], \quad k = 1...6 \tag{2.20a}$$

$$A_{kj}(\omega) = \mathbb{R}[\rho\int_{S_{0B}} \varphi n_k dS] \tag{2.20b}$$

$$B_{kj}(\omega) = -\Im(z)[\rho\int_{S_{0B}} \varphi n_k dS] \tag{2.20c}$$

Equation 2.20 shows that a time dependent excitation force is dependent on frequency dependent added mass and damping coefficients.

2.2.3.1.3 Limitations

The limitations of using a pure LPT method roots back to the LPT limitations in Section 2.2.2.2. For instance is LPT based on a constant water plane area, and this is not always the case when it comes to complex structures. Furthermore, higher order effects are not included in the velocity potential.

2.2.3.2 Morison's Equation Formulation

Morison's equation is another method to determine the hydrodynamic loads on a floating structure. Morison's method simplifies the radiation and diffraction term, such that it is only applicable for a limited number of structural designs. The theory is applicable for slender elements piercing the sea surface vertically, where the diameter of the cylinder is small compared to the wavelength.

The excitation force that arises from Morison's equation is shown in Figure 2.21a. It consists of an inertia and a drag term[15].

$$\mathbf{F}^{\text{Hydrodynamic}} = \mathbf{F}_{\text{Inertia}} + \mathbf{F}_{\text{Drag}} \tag{2.21a}$$

$$\mathbf{F}^{\text{Hydrodynamic}}(t) = \rho V \mathbf{a} + \rho C_a V(\mathbf{a} - \ddot{\eta}) + \frac{\rho}{2} C_D A |\mathbf{v} - \dot{\eta}|(\mathbf{v} - \dot{\eta}) \tag{2.21b}$$

Equation 2.21b is derived from the general formula for a structure which is moving in its 6 DOF's, η. The variables **a** and **v** are respectively the fluid particle velocity and acceleration, gathered from the velocity potential. ρ is the density of water, V is the displaced volume, A is the cross section, C_A is an added mass coefficient and C_D is the drag coefficient. The inertia term can be seen as the added mass term, while the drag term can be look as the diffraction term. The added mass term is not dependent on the frequency. It is in addition seen that the hydrodynamic force does not have a damping term.

2.2.3.2.1 Limitations

The limitations with Morison's theory is directly found from its area of applicability. If the structure is characterized as large volume (not slender) outgoing fluid (radiation) will be of great importance, which Morison's theory does not capture[15]. This means that constant added mass will be wrong because added mass is strongly dependent on oscillating frequency for large volume structures.

To summarize does Morison's Equation not include potential damping (frequency dependent damping) or frequency dependent added mass, which leads to errors in calculating the hydrodynamic force for large volume structures.

2.2.4 Nonlinear Hydrodynamic Loading

Higher orders must be included, for a correct representation of nonlinear hydrodynamic forces. However, these effects are difficult to implement and solve, meaning that general observation of nonlinear hydrodynamic phenomena is of interest.

The nonlinear hydrodynamic loading will consider an unmoored structure which is designed with a torus and heave plates.

2.2.4.1 Torus

A torus is a freely floating ring which is submerged with half of the torus diameter. A torus has a constant water plane area when it is freely floating, but when it moves due to incident waves or the wind will the water plane change. Linear theory assumes constant water plane area, and the effect of nonconstant water plane area leads to a nonlinear formulation.

An important nonlinear effect for a torus is the moving in and out of the sea surface, leading to an added mass and damping that may be larger or smaller than assumed in linear theory. A submerged torus is shown in Figure 2.4.

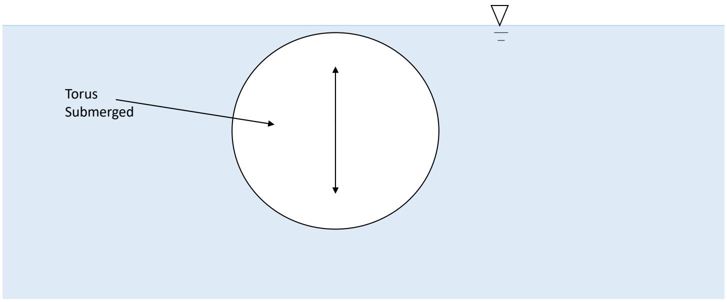

Figure 2.4: Submerged torus

The torus represented in the figure can either oscillate below the sea surface or in and out of the sea surface. Thus will a submerged torus in most cases acceleration towards the sea surface due to the large buoyancy force. As the torus reaches the sea surface, lots of waves are generated from the structure, which leads to higher order damping effects.

The same nonlinear phenomena are also similar to the slamming events, which is connected to a nonlinear representation of added mass. The energy that accelerates the structure and decelerates the fluid is the nonlinear added mass term. The added mass depends on many variables and is challenging to estimate [38]. It depends on the structural motion before impact, the displacement characteristic of the structure, and the duration of the impact.

The added mass and damping are for linear theory calculated from small responses and deformation. The nonlinear added mass and damping due to torus submergence, on the contrary, is strongly connected to higher order effects.

Nonlinear loads arise on the torus when it is exposed to regular waves. One nonlinear effect is when the waves go over the torus, shown in Figure 2.5.

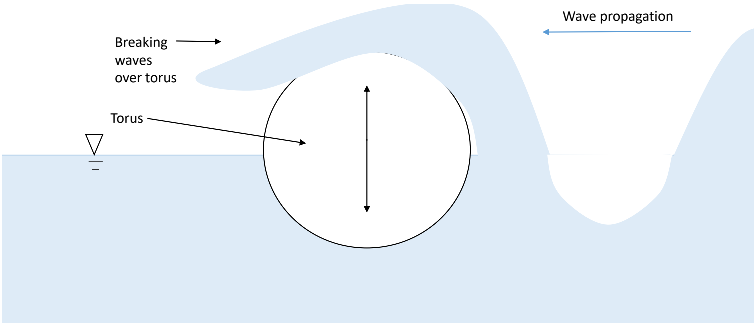

Figure 2.5: Slamming over torus

The drag and mass coefficient changes, due to this effect. The drag term is not only contributed by half the torus circle but now on the upper side as well. This additional contribution to both added mass and drag is iimportant to notice in nonlinear analysis.

2.2.4.2 Heave Plates

Heave plates for a structure are used for floating wind turbines to lower the center of gravity, increase the inertia mass and increase the added mass. The latter contribution, the increase of added mass, is the main contribution from heave plates. A heave plate attached to a torus cross-section is shown in Figure 2.6.

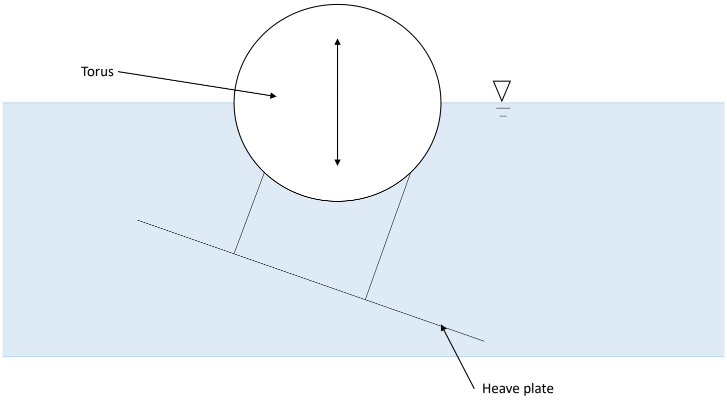

Figure 2.6: Heave plates

A reliable analysis for heave plates is when a structure oscillates with small motions, i.e. linear motions. The added mass do not conflict with linear theory unless the motions are too great. For instance, nonlinear phenomena will occur when the heave plate approaches the sea surface, and especially if it exits the splash zone.

Attached heave plates result in lower hydrodynamic loads, but the exact contribution is difficult to establish due to many uncertainties when a structure oscillates.

2.3 Aerodynamic Loading

The aerodynamical loading on a WT depends on various elements, and there exist two main theories to solve this problem. The blade element momentum (BEM) theory governs steady loads, while Generalized Dynamic Wake (GDW) theory governs dynamical loads. These two theories will be investigated thoroughly in this section. The final part will investigate a well-known unsteady BEM model which is often applied for WT analysis.

2.3.1 Blade Element Momentum

The BEM theory is a simplification to the aerodynamical problem. BEM theory is based on two fundamental theories, blade element theory, and moment theory [37].

The blade element theory is based on regular finite element theory (FEM). A blade can be divided into a selected number of smaller elements, calculate the associated forces and moments of each element and integrate these over all blades, to establish the total force/moment. Each element can, therefore, be approached as a 2D problem, as long as the number of elements is sufficiently large. The moment theory assumes that the change in pressure across the rotor is only due to the work done by the rotor blade itself. This leads into five main limitations [22], [37]:

- No radial dependency - what happens at one element does not affect another element along the blade.
- The force on each blade is constant for the whole angular rotation, which corresponds to an infinite number of blades.
- Only steady flow - Inherited time lag and the dynamic wake is not included.
- Large deflections of blades are not accounted for.
- No tip or hub influence

On behalf of the statements listed above breaks the BEM method down to a simplified procedure to calculate the forces and moments. The figures in Figure 2.7 summarizes the general BEM theory.

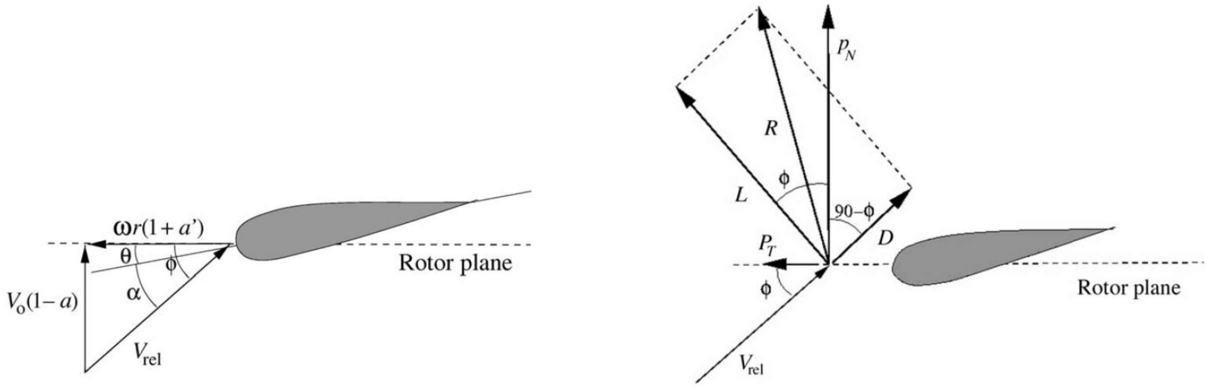

(a) Velocity at the rotor plane

(b) Loads on the 2D blade

Figure 2.7: Induced velocities and loads according to BEM theory (Taken from [22])

Figure 2.7a shows the method for calculating the relative velocity working on the blade, V_{rel}. This is dependent on the induced velocity factor, a, and rotational factor, a' and the rotational speed ω. A more thorough description of values a, a' and induced velocities can be seen in [37] and [22]. Furthermore, the inflow angle, ϕ, is the sum of local pitch angle and angle of attack. The inflow angle are establish in Equation 2.22, and the relative velocity can also be established by:

$$\tan\phi = \frac{V_0(1-a)}{\omega r(1+a')} \tag{2.22}$$

where r is the distance from the hub to the selected element. The steady state property is useful when calculating the torque and thrust, which is used for the external load. Figure 2.7b visualizes the method for establishing these forces. Equation 2.23 goes into specific detail in order to establish the torque and moment.

$$dT = Bp_N dr = B(L\cos\phi + D\sin\phi)dr \tag{2.23a}$$

$$dM = rBp_T dr = Br(L\sin\phi - D\cos\phi)dr \tag{2.23b}$$

There exist some methods for improving a numerical model that uses BEM theory. Some of these methods are the prandtl's tip loss factor and the Glauert Correction for high values of an induced velocity factor. Another method is the Generalized Dynamic Wake, which is described in the next section.

2.3.2 Generalized Dynamic Wake

The Generalized Dynamic Wake (GDW) method is an improved method, related to BEM theory, for calculating loads on a WT. The method has a significant computational time compared to BEM method, due to iterations and integration within the method. The method is used for higher wind speeds, especially for wind speeds greater than 8 m/s [37].

The main understandable difference from BEM is that GDW establishes a more realistic pressure field along the rotor. The thoeries are based on potential flow theory and must fulfill the Laplace Equation (somewhat similar to LPT theory). The pressure found from the GDW includes the contribution from the dynamic wake effect, tip losses, and skewed wake effects at time instant t, due to a pressure field up to time t. The method for establishing the GDW pressure and loads are through time- and space-dependent induced velocities and are furthermore quite complex. A detailed description for implementing GDW can be seen in [37].

2.3.3 Unsteady BEM model

An unsteady BEM model is often used for representing a numerical model. The unsteady BEM model takes dynamic inflow and yaw errors into consideration, and can be looked like a combination of BEM and GDW theory.

An unsteady BEM model is a realistic numerical model that computes realistic aeroelastic motions. It is necessary to create several fixed coordinate systems along the WT, to see the difference between the initial and dynamical position. The most convenient and general setup of coordinate systems is shown in Figure 2.8.

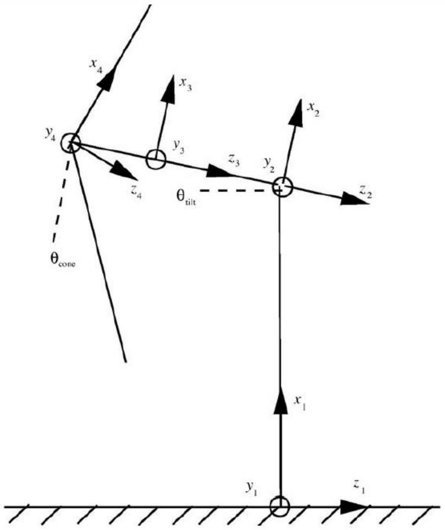

Figure 2.8: Unsteady BEM model (Taken from [22])

This coordinate system consists of 4 fixed coordinate systems. With transformation matrices, it is possible to understand the motion between the different coordinate systems.

The method for establishing the dynamic inflow is by supernate the relative wind into the steady wind speed, rotational speed and the induced velocities, Equation 2.24 [37].

$$\mathbf{V}_{\text{rel}} = \mathbf{V_0} + \mathbf{V}_{\text{rot}} + \mathbf{W} \tag{2.24a}$$

$$\begin{pmatrix} V_{\text{rel,y}} \\ V_{\text{rel,z}} \end{pmatrix} = \begin{pmatrix} V_y \\ V_z \end{pmatrix} + \begin{pmatrix} -\omega c \cos\theta_{\text{cone}} \\ 0 \end{pmatrix} + \begin{pmatrix} W_y \\ W_z \end{pmatrix} \tag{2.24b}$$

$\mathbf{V_0}$ is found by general BEM theory and **W** is found later in this section, and when this is known, it is possible to establish the angle of attack, ϕ (Figure 2.7a).

These induced velocities are further included into the dynamic wake model by two differential equations, shown in Equation 2.25[37].

$$W_{\text{int}} + \tau_1 \frac{dW_{\text{int}}}{dt} = W_{\text{qs}} + k\dot{\tau}_1 \frac{dW_{\text{qs}}}{dt} \tag{2.25a}$$

$$W + \tau_2 \frac{dW}{dt} = W_{\text{int}} \tag{2.25b}$$

where W_{qs} is the induced velocities from Equation 2.24, W_{int} an intermediate value, W as the dynamic wake related induced velocity and k is a constant. τ_1 and τ_2 are time constants. This method is proposed from S. Øye and can be explored in detail in [37].

The yaw error is accounted for in the unsteady BEM model by the standard Glauert model. The yaw problem is related to different wind speeds on the blade downstream compared to the blade upstream during yaw motion. The blade upstream will be exposed to a higher wind speed relative to the blade downstream, since the blade downstream is deeper within the wake. Higher wind speeds lead to higher loads, such that the blades will produce a beneficial yawing moment that will force the turbine to move back to its initial position. This effect is accounted for using Equation 2.26 [37].

$$\mathbf{W} = \mathbf{W_0}(1 + \frac{r}{R}\tan\frac{\chi}{2}\cos(\theta_{\text{wing}-\theta_0})) \tag{2.26}$$

where r is the distance to the selected element, R is the radius of the rotor, χ is the wake skew angle, θ_{wing} is the rotation of the blade and θ_0 is the angle where the blade is deepest into the wake.

The method listed in this section is directly connected to the improvement of the inflow velocity, and by implementing this general BEM theory, it is usable for establishing the excitation forces from the rotor. A thorough explanation of the excitation force will not be investigated in this Master's thesis, so the excitation force for the rotor is not written out in Equation 2.27.

$$F^{\text{Rotor}} = F^{\text{Torque}} + F^{\text{Moment}} \tag{2.27}$$

2.3.4 Drag on tower

The wind oscillation toward a tower structure may excite structural motions if the structure oscillates in the frequency of excitation. The wind oscillation period goes under the term slowly-varying, which has a period of 1 to 2 minutes [21]. This excitation force is shown in Equation 2.28[21].

$$F^{\text{Tower,drag}} = \frac{1}{2}\rho_{\text{air}} C_D \bar{U}^2 + \rho_{\text{air}} A \bar{U} u' \tag{2.28}$$

where ρ_{air} is the density of air, C_D is the tower drag coefficient, $\bar{U}$ and u' is respectively the mean and fluctuating wind speed.

2.4 Mooring Lines Loading

The mooring lines for a moored structure is shown in Figure 2.9.

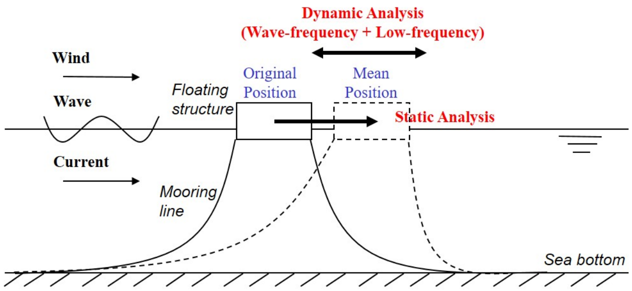
Dynamic Analysis
(Wave-frequency + Low-frequency)
Wind
Wave
Current
Floating structure
Original Position
Mean Position
Static Analysis
Mooring line
Sea bottom

Figure 2.9: Motions of a moored structure (Taken from [18])

The loads acting on the structure consist of waves, wind, and current. The waves are split into two; first order wave loads (linear) and second order wave loads (nonlinear). The first order wave loads can be determined by LPT, while the second order wave load consider the difference frequency between two adjacent frequencies.

Based on the figure above, the excitation force for a moored structure can be established, and divided into first and second order wave loads [18], as in equation 2.29.

$$F^{\text{Mooring Lines}} = -B_1\dot{\eta} - B_2 f(\dot{\eta}) - K(\eta)\eta \tag{2.29a}$$

$$\eta = \eta_{WF} + \eta_{LF} \tag{2.29b}$$

In the above equation, X_{WF} describes the motion from wave frequency (linear), while X_{LF} describes the motion from the low frequency (nonlinear). The two damping terms shows the first and second order damping coefficients, while K is the mooring stiffness matrix as function of displacement.

2.5 Structural Loading

The structural loading arises from the environmental loads. The structural deflections and rotations from the exposed loads depend on the diameter, thickness, and shape of one element and how this element interacts with other elements with the same or different property. The structural loading is useful to establish stresses and forces which can be further post-processed.

This section will outline how the structural elements are formulated. In addition, the structural mass matrix and the structural damping matrix will be outlined.

2.5.1 Nonlinear Beam Element Theory

All elements of the OFWT are defined as beam elements, in a pure Morison's model. Deflections and rotations of all elements are calculated by nonlinear beam element theory (BEM). The nonlinear BEM is essential to understand, to solve the internal strains/stresses for vital parts of a floating wind turbine. A beam is defined as a long, slender structural element that is subjected to transverse loading that gives a significant bending effect compared to twisting and axial stress [30]. The linear beam element theory (Euler-Bernoulli theory) assumes the following [7], [30]:

- Plane cross sections perpendicular to the longitudinal axis of the beam remains plane and perpendicular to the longitudinal axis after lateral loading.
- There are no shear deformations due to lateral loading (in contrary to the Timoshenko Theory)
- The lateral contraction due to axial elongation is negligible
- Internal strains are small

To use the linear BEM on a nonlinear problem, a co-rotated (CR) coordinate element system is introduced. A CR element system is shown in Figure 2.10.

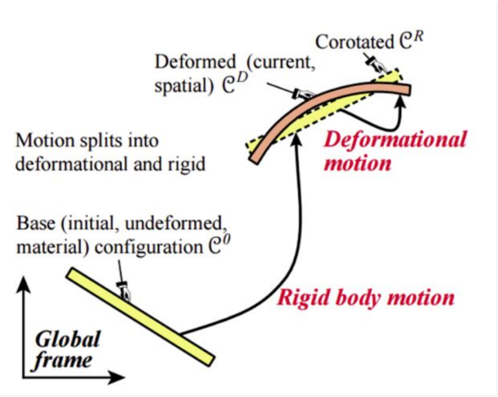
Corotated $\mathcal{C}^R$
Deformed (current, spatial) $\mathcal{C}^D$
Motion splits into deformational and rigid
Deformational motion
Base (initial, undeformed, material) configuration $\mathcal{C}^0$
Rigid body motion
Global frame

Figure 2.10: Co- rotated coordinate system (Taken from [16])

The idea behind the CR approach is to develop a ghost frame rigid body system that follows the elements rotation and displacement. The elements translation is then expressed in terms of the CR coordinate system. This results into small displacements and rotations within the ghost frame, while large displacements and rotations within the global frame. The linear theory is, therefore, applicable within the ghost frame, and for the whole problem. Two important facts should be notified: There cannot be any thickness deformation of the element, and the element resolution must be sufficiently large. A more detailed approach can be seen in [16].

2.5.1.1 Time-domain - Finite Element Method

The inertia forces, damping forces and restoring forces are based on the hypothesis that the internal forces are to be equal to the external forces[7]. This is represented in Equation 2.30.

$$\mathbf{M}_{\text{structure}}\ddot{\eta}(t)+\mathbf{B}_{\text{structure}}\dot{\eta}(t)+\mathbf{R}^{int}=\mathbf{F}^{ext} \tag{2.30}$$

The external energy in this manner are forces and moment which arises from the static and dynamic load, presented in the previous sections. The internal energy is computed as the change in strain, or the systems possibility to restore the forcing energy. The internal energy for a linear elastic system is defined to be[7]:

$$\mathbf{R}^{int}=\mathbf{K}_{\text{global}}\eta(t) \tag{2.31}$$

Where **K** is the global restoring matrix, where global is denoted as the sum of all restoring coefficients. Thus may **K** in a nonlinear analysis be dependent of $\eta(t)$ (for instance in mooring lines), such that the equation of motion must be solved through iteration. This is seen in Section 2.6.2.

2.5.2 Inertia and Damping Loads

The mass matrix consists of two parts: the foundation and the tower. The mass matrix of a structural system with interconnected elements can be arranged in alternative ways. Among these are lumped and consistent mass matrix the most relevant. Lumped mass matrix is diagonal and useful in explicit time iteration. Consistent mass matrix is accurate.

Structural elements that are subjected to vibrations will dissipate energy through three sources: nonlinear restoring forces, energy radiation, and damping in the structure. This section will consider the structural damping term **B**. The structural damping is due to the interaction between the elements and will influence the vibrational response. Rayleigh damping method is often used for solving this problem since it is easy and takes both the stiffness and mass into consideration[10]. The mass matrix is the total mass, while the stiffness matrix is gathered from hydrostatic and mooring coefficients. The Rayleigh structural damping is shown in Equation 2.32[10].

$$B_{\text{structure}} = \alpha M_{\text{global}} + \beta K_{\text{global}} \tag{2.32}$$

where α and β are constants with the units of s^{-1} and s, respectively. These constants are determined from laboratory tests in order to get the correct damping. Another approach is that the structural damping coefficients, α and β, depends on the structural motion modes (from the 7 DOF and higher). These can be solved by determination or by an eigenvalue analysis. The following method uses the modes, 7->, through an eigenvalue analysis in order to determine the damping coefficients[10]:

$$\zeta_i = \frac{\alpha}{2\omega_i} + \frac{\omega_i \beta}{2} \tag{2.33}$$

where ζ_i is the damping ratio in each mode, j, and ω_i is the natural frequency in the same mode.

The major advantage of using the Rayleigh damping method is that it uses an orthogonal transformation of the structural mass and stiffness. This implies that a n body system is reduced to n equation, with n unknowns. This saves computational time.

2.6 Motions

The structural motions consist of displacement, velocity, and acceleration. These motions can be expressed either by flexible elements or rigid body elements. Flexible elements obtain the loads on a discretized element, where local motions can be obtained through forces and moments. These motions can be integrated over the whole body to give the global motions. The global motions can also be related to the rigid body motions, where the rigid body motions are established by rigid elements. The motions of the structural elements is found by multiplication of the length from the MSL. Rigid elements have an infinitely stiff cross-section such that local moments and forces are not possible to obtain. The different application of flexible and rigid elements arise from whether a Morison's or LPT is used to establish the external forces and moments. An LPT formulation obtains the total force by integrated the pressure along the whole sea surface before the total load is applied at one point. The Morison's formulation integrates the load for all discretized elements, to establish the global motions.

Disregarding whether Morison's or LPT is used for establishing the external loads, can the global motions be expressed as an N DOFs system. A random floating wind turbine oscillation in its six rigid DOFs is shown in Figure 2.1.

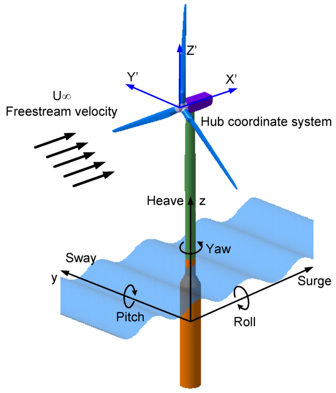

Figure 2.11: Degrees of freedom for a floating wind turbine(Taken from [19])

Table 2.1: Degree of Freedom

Translation	**Symbol**	**Degree of Freedom, j**
Surge	η_1	1
Sway	η_2	2
Heave	η_3	3
Roll	η_4	4
Pitch	η_5	5
Yaw	η_6	6

The number of DOFs has a minimum of 6, but it is possible to have even more. This is seen for instance for a double body, where the global motions are expressed by 12 DOFs. The equation of motion related to the forces for a 6 DOFs system follows newtons second law:

$$\sum \mathbf{F} = \mathbf{M} \cdot \ddot{\eta} \tag{2.34a}$$

$$\sum \mathbf{F} = \mathbf{F}^{\text{External}} + \mathbf{F}^{\text{Internal}} \tag{2.34b}$$

$$F^{\text{Internal}} = F^{\text{Structure/Resistance}} \tag{2.34c}$$

$$F^{\text{External}} = F^{\text{Hydrostatic}} + F^{\text{Hydrodynamic}} + F^{\text{Aeordynamics}} + F^{\text{Mooring}} \tag{2.34d}$$

where $\mathbf{M}$ is the mass matrix and $\sum \mathbf{F}$ is the external and internal forces and moments due to the environmental conditions and the structural resistance, respectively. Forces are applied for the displacement translations (surge, sway and heave), while moments are applied for the rotational translations (Roll, Pitch, and Yaw). The external loads consist of a contribution from hydrostatic, hydrodynamic, aerodynamic and mooring. These loads are presented in Section 2.2.1, Section 2.2.3, Section 2.3 and Section 2.4. The internal loads arises from Section 2.5. With the external and internal loads defined it is possible to establish the Equation Of Motion (EOM), which will be presented in the next section.

2.6.1 Equation of Motion in Frequency- and Time-Domain

It is possible to represent the EOM in frequency or time-domain, and this is dependent on which theory the hydrodynamic loading arises from. The LPT is based on frequency dependent coefficients, while Morison's theory is represented in time-domain.

2.6.1.1 Frequency-Domain

The frequency-domain is often used for Response Amplitude Operator (RAO) analysis, where the frequency is constant for each run. LPT is initially frequency formulated, seen by the diffraction and radiation problem in Section 2.2.3.1. An example of a frequency formulated equation of motion for hydrodynamical and structural loads is shown in Equation 2.35.

$$\eta = Y(\omega)e^{i\omega t} \tag{2.35a}$$

$$F(t) = F(\omega)e^{i\omega t} \tag{2.35b}$$

$$[-\omega^2(M_{\text{global}} + A(\omega)) + i\omega(B_{\text{global}} + B(\omega)) + C_{\text{global}}]\,Y(\omega) = F^{\text{External}}(\omega) \tag{2.35c}$$

where the global notation gives the sum for foundation, tower and rotor, and the external force is due to the Froude Kryloff, drag and aerodynamic forces and moments. Thus, it is in most practical cases most interesting to do time-domain simulation. Time-domain simulations corresponds to real life situation, and takes for instance phase differences into consideration. The solution is to go from frequency-domain to time-domain, by inverse Fourier transformation.

The method for doing a frequency to time formulation is described in [17] and [25]. The main parts of the method are to represent the frequency dependent added mass and damping as a convolution integral or an impulse-response function. Out of importance for later sections is the frequency dependent added mass and damping solution shown in Equation 2.36[17].

$$\mathbf{A}(\omega)\ddot{\mathbf{x}}(\mathbf{t}) + \mathbf{B}(\omega)\dot{\mathbf{x}} \tag{2.36a}$$

$$\mathbf{A}_\infty\ddot{\mathbf{x}}(\mathbf{t}) + \underbrace{\int_{-\infty}^{\infty}\kappa(t-\tau)}_{\text{Retardation function}}\ \dot{\mathbf{x}}(\tau)\,d\tau \tag{2.36b}$$

$$\kappa(\tau) = \frac{1}{\pi}\int_0^\infty \big(\mathbf{b}(\omega)\cos(\omega\tau) - \omega\mathbf{a}(\omega)\sin(\omega\tau)\big)\,d\omega \tag{2.36c}$$

Equation 2.36 represents the frequency dependent added at infinite frequency and frequency dependent within a convolution integral. The frequency dependent potential damping, on the other hand, is only included within the convolution integral. The equations in Equation 2.36 makes it possible to represent frequency dependent coefficients in time-domain, which is necessary for representing LPT in time-domain for this Master's thesis.

2.6.1.2 Time-Domain

LPT and Morison's theory can now be represented in the time-domain. This is due to the impulse-response technique shown in Equation 2.36.

The EOM with the Morison's hydrodynamic formulation is shown in Equation 2.38.

$$M_{\text{global}}\ddot{\eta}(t) + B_{\text{global}}\dot{\eta}(t) + C_{\text{global}}\eta(t) = F^{\text{Inertia}}(t) + F^{\text{Drag}}(t) + F^{\text{Aero}}(t) \tag{2.37a}$$

$$M_{\text{global}} = M_{\text{foundation}} + M_{\text{WT}} \tag{2.37b}$$

$$B_{\text{global}} = \underbrace{\alpha M_{\text{global}} + \beta C_{\text{global}}}_{\text{Rayleigh Damping}} + B_{\text{Mooring}} \tag{2.37c}$$

$$C_{\text{global}} = C_{\text{Mooring}}(\eta) + C_{\text{Hydrostatic}} \tag{2.37d}$$

The coefficients and terms are mentioned in previous sections, and can be defined in the Nomenclature. This EOM is based on constant added mass (from the inertia force) coefficients and a external damping term only dependent on the drag and mooring lines.

The EOM with the LPT hydrodynamical formulation is shown in Equation 2.38.

$$(M_{\text{global}}+A_{\infty})\ddot{\eta}(t)+B_{\text{Global}}\dot{\eta}(t)+\underbrace{\int_{-\infty}^{\infty}\kappa(t-\tau)}_{\text{Retardation function}}\dot{\eta}(\tau)d\tau+C_{\text{global}}\eta(t) = F^{\text{Diffraction}}(t)+F^{\text{Drag}}(t)+F^{\text{Aero}}(t) \tag{2.38}$$

The $_{\text{global}}$ terms in Equation 2.38 has the same setup as presented in Equation 2.37. The difference between the LPT formulated EOM is that the frequency dependent damping term (Retardation function) and added mass.

2.6.2 Time - Integration: HHT- α method

The Morison's or LPT formulated EOM can both be solved by using a time-integration called generalized-α method [20]. This method makes it possible to solve the EOM for nonlinear terms, for instance if the associated mooring line stiffness is dependent on the displacement. The solution is to use a temporal integration method for determining the next terms in the EOM. There exist different ways to solve this, where Hilber-Hughes-Taylor (HHT) method is a combination of the implicit Generalized-α method and the implicit Newmark scheme [40]. The HHT method reduces to the Newmark scheme if α is zero. The EOM, with the HHT-method is now shown in Equation 2.39[20]:

$$M\ddot{\eta}_{i+1} + (1-\alpha)C\dot{\eta}_{i+1} + \alpha C\dot{\eta}_i + (1-\alpha)K\eta_{i+1} + \alpha K\eta_i = (1-\alpha)f^{ext}_{i+1} + \alpha f^{ext}_i \tag{2.39}$$

where the coefficients are the same as determined before. This equation is exactly the same as the EOM for the Newmark scheme, only with the added condition that the acceleration is constant within a time step. The integration process follows in the two next equations[20]:

$$\eta_{i+1} \approx \eta_i + \delta t\dot{\eta}_i + \delta t^2[(0.5-\beta)\ddot{\eta}_i + \beta\ddot{\eta}_{i+1}] \tag{2.40a}$$

$$\dot{\eta}_{i+1} \approx \dot{\eta}_i + \delta t[(1-\gamma)\ddot{\eta}_i + \gamma\ddot{\eta}_{i+1}] \tag{2.40b}$$

where δt is the time step, β, and γ are constants. The HHT-α second order accurate and unconditionally stable if:

$$0 \leq \alpha \leq \frac{1}{3}, \qquad \text{and} \tag{2.41a}$$

$$\beta = \frac{(1+\alpha)^2}{4}, \qquad \text{and} \tag{2.41b}$$

$$\gamma = 0.5 + \alpha \tag{2.41c}$$

This time-integration method makes it possible to perform short or long-term analysis for a numerical model.

2.7 Time-Domain Response Analysis

The time-domain response analysis can be described as the investigation of loads and its contributions for different lifetime conditions. The load contribution to the structural responses is due to the environmental loads from wind and waves, where certain environmental loads may dominate for specific conditions. The response analysis can be pictured as in Figure 2.12, which gives an overview of the induced loads for its associated frequency.

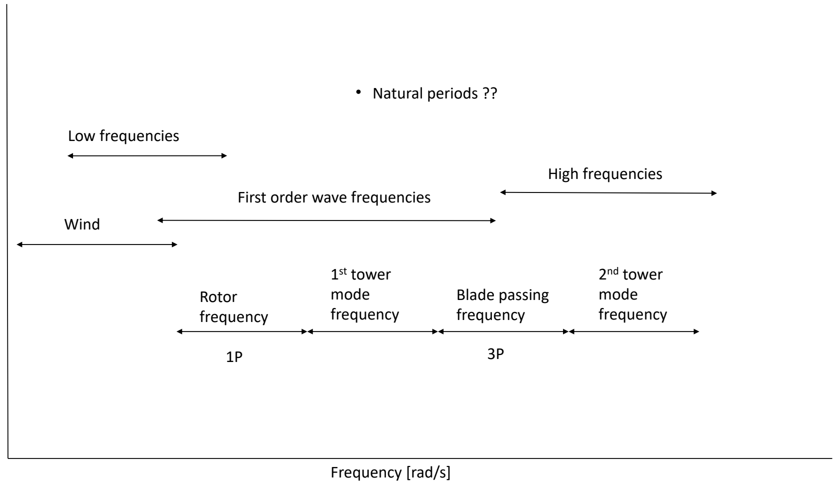
• Natural periods ??
Low frequencies
High frequencies
First order wave frequencies
Wind
Rotor frequency
1st tower mode frequency
Blade passing frequency
2nd tower mode frequency
1P
3P
Frequency [rad/s]

Figure 2.12: Relevant excitation frequencies for a floating wind turbine

No values are applied in Figure 2.12, since this figure is meant to be valid for all floating wind turbines. This figure represents the excitation frequency for waves (Low, first order and high wave frequencies) and wind loads. The resonant frequencies for the rigid and flexible body are described as the natural periods and the rotor and tower modes frequencies. The explanation and relationship between these frequencies and the content of Figure 2.12 will be presented in the next sections.

2.7.1 Rigid Body Resonant Frequencies

The natural periods for a rigid body structure is calculated by:

$$T_{nn} = \sqrt{\frac{M_{nn} + A_{nn}}{C_{nn}}} \tag{2.42}$$

where n is the degree of freedom. The natural periods gives a good prediction on how a structure will oscillate during linear and nonlinear waves. It is for all designs necessary to have natural periods that are outside the 1^{st} order wave frequency interval, in order to minimize the structural motions due to waves.

The natural periods in the rotational direction (3,4,5) are often the natural periods of concern when linear waves are analyzed. If the natural periods are outside this interval is this a good base for further development. The natural period in the horizontal direction (1,2,6) are often excited for nonlinear wave periods (low and high frequencies) such that large excitation can occur for these directions as well.

2.7.2 Flexible Body Resonant Frequencies

The flexible body resonant frequencies are mainly due to the rotor and tower contribution. The rotor contribution to resonant frequencies is due to the rotational speed of the rotor. Induced wind loads will create a moment at the top of the turbine tower, which gives a rotor and blade passing resonant frequency. These frequencies are also denoted as the 1P and 3P resonant frequency, which may be significant since these are often within the first order wave interval.

Resonant frequencies for first and second tower mode can be obtained through an eigenvalue analysis for the wind turbine. The excitation loads from these frequencies are often determined from the rotor, and can not be changed unless the tower and rotor are changed.

2.7.3 Coupling

A full time-domain response analysis includes the coupling effects between winds and waves.

The structural motions are often wave- or wind-dominated. This determination can often be assembled through spectral analysis for certain conditions. However, the wind loads may reduce global motions, compared to a structure exposed to only waves. The clearest example can be seen in Figure 2.13 for an operating turbine, where the rotor has a thrust force.

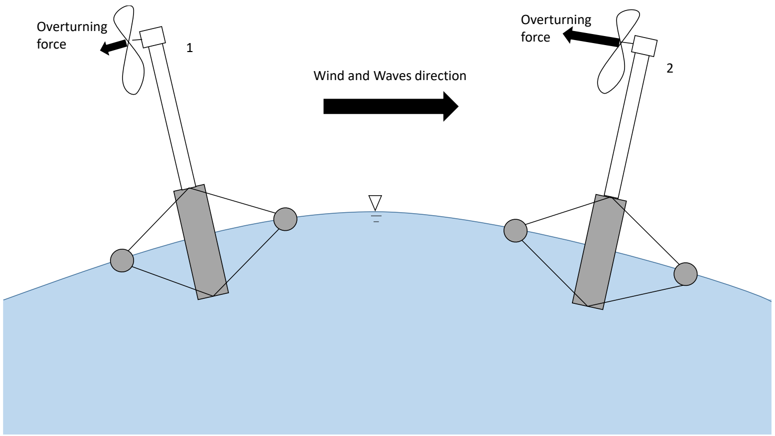

Figure 2.13: Damping contribution from rotor

Figure 2.13 illustrates a pitch damping due to the thrust from the rotor, if the thrust shall be constant during operation. The incident wind speed will be lower when the structure pitches downwind, such that the rotor rotates faster. This results in a larger thrust force, and a beneficial counteracting moment. The incident wind speed will be higher, if the structure pitches front wind, such that the rotor rotates slower. This results in a smaller thrust force, which is also beneficial.

Further, a detailed coupling effects for fault and the pitch controller (in addition to the mentioned conditions) will not be investigated in this Master's thesis.

2.8 Design Checks

The structural load effects, regarding internal forces and stresses raised from structural motions, must be checked for design requirements for all WTs. There exist design requirements for all possible situations, which may lead to a failure. The most relevant situations during the lifetime for an OFWT are categorized through four limit states. These limit states are the fatigue limit state (FLS), ultimate limit state (ULS), serviceability limit state (SLS) and accidental limit state (ALS). These limit states set requirements for the structural stability. All design checks for a floating wind turbine is gathered from DNV's Recommended Practice (DNV-RP), and the specific DNV-RP for a particular check will be outlined continuously in this section. The most critical design checks, FLS and ULS, will be considered in this Master's thesis.

2.8.1 Fatigue Limit State

A beam is not smooth along the surface. Beams are welded together and have internal imperfections which over time leads to cracks [7]. Cracks will lead to fractures, which is what defines a fatigue problem. Fatigue occurs when a beam is subjected to loading and offloading over a long period of time. The fatigue load or the stress range $\Delta\sigma$, is lower than the material strength (yield). The fatigue calculations are therefore expressed as the number of stress range occurrences to failure, N, and the stress range, $\Delta\sigma$/ S. This results into S-N curves. The basic design S-N curve is given as:

$$logN = loga - mlog\left(\Delta\sigma\left(\frac{t}{t_{ref}}\right)^{k}\right) \tag{2.43}$$

where constants a, m, σ and t_{ref} are empirical parameters found from testing. Different types of coefficients should be selected for different types of structural elements and for different number of stress range occurrences to failure (N). These constants are found from DNV-RP-C203[2].

The stress orientation of the relevant forces and moments for the bottom of the tower for an OFWT (tower base) are shown in Figure 2.14.

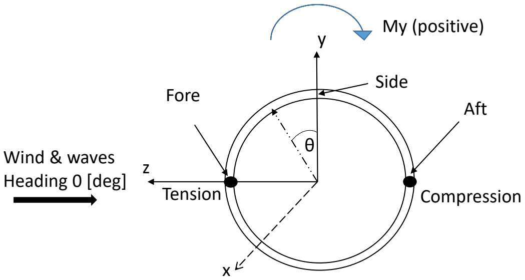

Figure 2.14: Orientation of coordinate system at tower base, forces and moments during a FLS analysis (based on [7])

This figure shows that if the waves and wind oscillate in the given direction, and the moment about the y - axis is positive will the front and the back of the cross-section (Fore and Aft) have respectively tension and compression over the cross-sectional thickness. The reason for this determination can be seen through Equation 2.44, where the stress is established for different angles around the cross section.

$$\sigma_x(t) = \frac{N_x(t)}{A} + \frac{M_y(t)}{I_y} sin(\theta) + \frac{M_z(t)}{I_z} cos(\theta) \tag{2.44}$$

N_x, M_y and M_z are all output from a numerical model solver at a certain time, while A, I_y and I_z are respectively the area and moment of inertia about y- and z-axis for the tower base section. θ can vary from 0 to 2π radians to establish the stresses along the cross section. Thus, it is in most cases most relevant to establish the time series of the stress distribution for $\pi/2$, 0 and $-\pi/2$ to evaluate the fore, side, and aft stress distribution respectively.

The next step, in a fatigue analysis, is to analyze the stress time series with the Rainflow cycle method (RFC), to establish the fatigue damage for a certain sea state. This method was proposed by Matsuishi and Endo [36], and is verified to be the best method [13, 12].

The damage is then calculated by Equation 2.45. This equation is called the Palmgren - Miner's rule. K is the material property and m is the appropriate slope from the SN curve[2].

$$D_{RFC} = \sum_{i=1}^{n} K^{-1} n_i S_i^m \tag{2.45}$$

Equation 2.45 is expressed by a linear SN curve, but can be extended to a bi-linear SN curve. This means that a separate m and K is valid for each line in the bi-linear curve. The second part of the bi-linear SN curve appears after 10^7 cycles. The bi-linear values listed in Equation 2.45 can be establish, for instance for tower base, from Table 2-1 and Table 2-2 in DNV-RP-C203[2].

Table 2.2: Variables (Found in [2])

Location	tref	thk	Stresslim	m_1	m_2	$\log(K_1)$	$\log(K_2)$	Category
Tower Base	0.025	0.045	52.63	3	5	-12.164	-15.606	D, in air

A complete description of all sea states for a specific site must be defined to establish the associated stress time series, which again can be used to determine the environmental fatigue damage. This fatigue damage is compared with the design requirement. The total fatigue damage for k different sea states and the design requirement are listed in Equation 2.46.

$$D_{\text{20 year}} = \sum_{j=1}^{k} D_{\text{sea state j (20y)}} \cdot P_j \tag{2.46a}$$

$$D_{\text{20 year}} \leq 1 \tag{2.46b}$$

$D_{\text{sea state j (20y)}}$ and P_j are respectively the 20-year cumulative fatigue damage for a given sea state, j, and the probability of having such a sea state.

2.8.2 Ultimate Limit State

The design checks for Ultimate Limit State(ULS) requires that the maximum environmental load must be smaller than the maximum load carrying resistance. The maximum environmental loads are taken as the load which has a return period of 50 years, i.e. the highest load that occurs during 50 years for a certain sea state. The maximum load-carrying resistance is defined on behalf of the material property. The design requirement in all ULS calculations must be satisfied by:

$$\sigma_{Sd} \leq \sigma_{Rd} \tag{2.47}$$

where the design resistance of the material, σ_{Rd}, must be larger than the external design stress, σ_{Sd}. The design loads are multiplied with certain load combinations to account for uncertainties in the obtained loads and to include a safety factor. The safety factors and load combinations are shown in Table 2.3.

Table 2.3: Action factors for design loads in ULS (Found in [6])

Action combination	Permanent action	Environmetal action
a	1.25	0.7
b	0.9	1.35

The load combination (a or b) that gives the largest load is the relevant design load for the ULS calculations. The permanent action is the static loads on the turbine, while the environmental loads are due to the loads from the environment. Table 2.3 is only an excerpt from the DNV-RP-J101 [6], and a more detailed analysis which includes, for instance, failure can be seen in the same document [6].

The ULS condition contains various checks, and this Master's thesis will only focus on the yield and buckling conditions. This will be investigated in the next sections.

2.8.2.1 Yield

The design check regarding yield is performed according to DNV-RP-J101[6], and requires that the maximum design tension stress is smaller than the characteristic material yield strength. The time represented stresses are computed using Equation 2.44, where the maximum load is determined as the maximum tension stress during a time-domain simulation. The maximum loads are represented as design loads. The yield check requirement is shown in Equation 2.48.

$$\sigma_{\text{perm}}\gamma_{\text{perm}} + \sigma_{\text{env}}\gamma_{\text{env}} \leq \frac{f_y}{\gamma_{\text{m}} \cdot A} \tag{2.48}$$

In Equation 2.48 is f_y the material yield strength and γ_m a material safety factor. For most steel structures is the yield strength 250 Mpa, while the material safety factor is 1.1.

Equation 2.48 must be fulfilled to meet the requirement regarding yield.

2.8.2.2 Shell and Column Buckling

Buckling of shells occurs if the structure is subjected to a significant high load of axial compression, bending, circumferential pressure, torsion, shear or a combination. The stability requirement for buckling is performed according to DNV-RP-C202 [4]. The shell buckling requires that the maximum design compression stress is smaller than the characteristic buckling strength. The buckling requirement is formulated differently for different buckling modes. It is, for instance, different buckling requirements for beams, shells, and plates. The explanation of the difference will not be investigated in this Master's thesis, but out of later importance will only shells be outlined. The stability requirement for all types of buckling is given in Equation 2.49 [4].

$$\sigma_{j,Sd} \leq f_{ksd} \tag{2.49}$$

The development of these two parameters in Equation 2.49 is a detailed process, and will be shown in Appendix B.

The column buckling requirement is also performed according to DNV-RP-C202 [4]. The column buckling improvement shall be assesed if:

$$\frac{kL_C}{i_c} \geq 2.5\frac{E}{f_y} \tag{2.50}$$

where:

k = effective length factor, (equal to 1 for this case)

L_C = Total cylinder length (defined in the previous section)

i_C = $\sqrt{\frac{I_C}{A_C}}$, where I_C and A_C are respectively the moment of inertia and area of the cross section (defined by the cross section)

Chapter 3

Full-Scale and Model-Scale Model Presentation

This chapter consists of information and post-processing work performed in the project thesis [32] and during this Master's thesis. The concept information is related to a full description of experimental and full-scale model (from the project thesis), while the post-processing is related to the finalizing the experimental data for comparison study in Chapter 5 and 6 (Master's thesis). The latter part of this chapter consists of observations and problems, established in the project thesis.

This chapter consists of the main dimensions for the experimental and numerical model. The established Froude scaling factor from the project thesis [32], will also be mentioned. The setup of the tank facility, post-processing, and observations during experimental tests will also be outlined.

3.1 Presentation of Models

This section will present the models in full-scale and model-scale (experimental model).

3.1.1 Full-Scale Numerical Dimensions

The full-scale numerical model is shown in Figure 3.1.

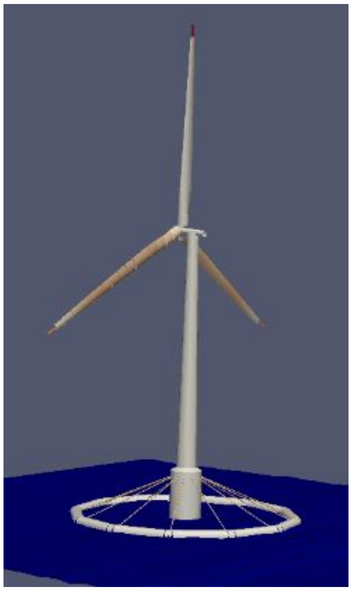

Figure 3.1: Full-scale numerical model

The full-scale numerical model consists of a spar column, a torus, spokes and heave plates. The spar column is shorter than for a regular spar structure since the torus contributes to the global stability. The spokes are interconnected pre-tensioned wires between the torus and the spar column. The heave plates are attached around the torus, to reduce the acceleration of the structure. These are below the sea surface in Figure 3.1

The full-scale dimensions are based on the initial input dimensions given from FO. It is seen, from Figure 3.1, that the numerical model has the full rotor attached. For some cases will an equivalent nacelle mass be applied, seen in Chapter 5 and 6.

The full-scale structure has the property steel, with a density of 8500 kg/m^3. The structural dimensions are listed in Table 3.1.

Table 3.1: Some full-scale structural dimensions

Structural dimensions	**Full-scale dimensions**
Column height	30 m
Column diameter	10 m
Torus large diameter	70 m
Torus diameter	3.7 m
Structural mass	2.11E+06 kg
Nacelle mass	400E+03 kg

3.1.2 Experimental Dimensions

The experimental model is designed on behalf of the numerical structural dimension in Table 3.1. The experimental model in the tank facility is shown in Figure 3.2. The experimental model w/ heave plates is not pictured in this figure.

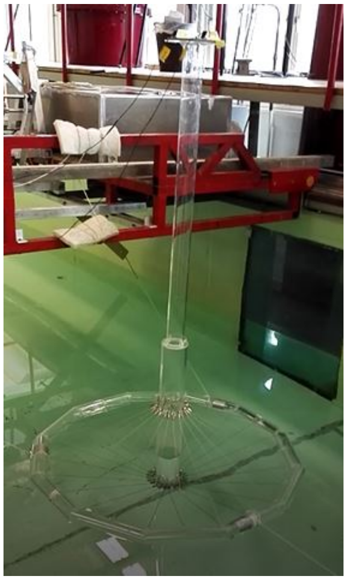

Figure 3.2: Experimental model

It is seen from Figure 3.2 that the numerical rotor with blades is replaced with an equivalent mass at the nacelle. The tower, column and the torus are all produced with the material plastic, while the spokes are modeled with steel. The connection points for the spokes are also steel.

The equivalent nacelle mass consists of steel plates. The structural dimensions are shown in Table 3.2.

Table 3.2: Experimental model dimensions

Structural dimensions	**Model-scale**
Column height	421.5 mm
Column diameter	90 mm
Torus large diameter	940 mm
Torus diameter	50 mm
Structural mass	4.024 kg
Nacelle mass	0.913 kg

The experimental model is not geometrical scaled according to the full-scale dimensions, as presented in the introduction of this Master's thesis. Previous work regarding the validity of the geometrical scaling factor is shown in Appendix C.2, based on Froude Scaling method (Appendix C.1.1). On behalf of the given dimensions for the full-scale structure, and dimensions of the experimental model is the Froude scaling factor established to be 74.

3.2 Tank Facilities

The experimental model floating in the tank is shown in Figure 3.3.

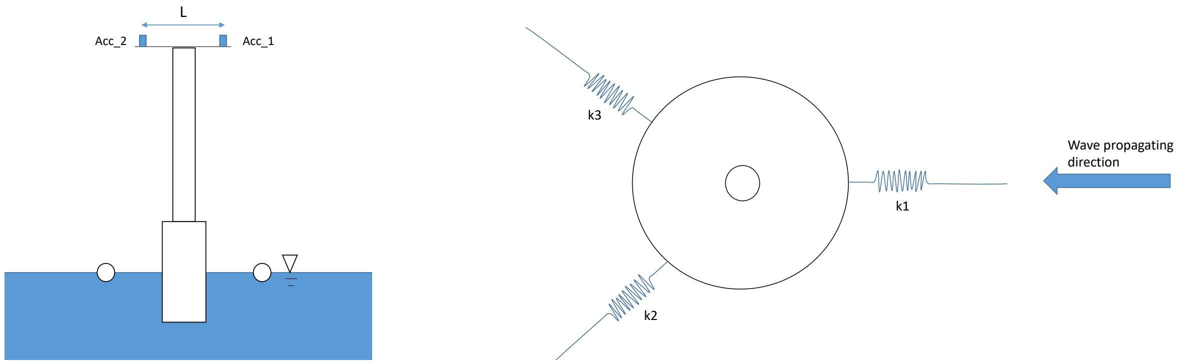
L
Acc_2
Acc_1
k3
k1
k2
Wave propagating direction

(a) Accelerometers

(b) Spring system

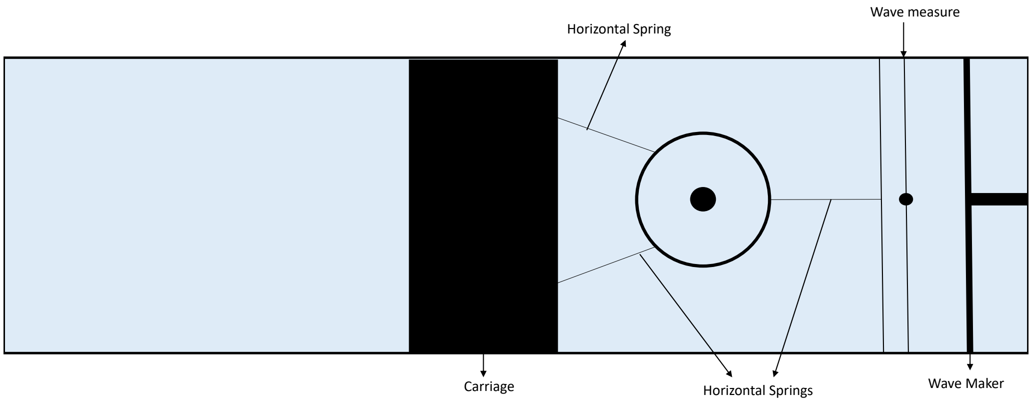
Horizontal Spring
Wave measure
Carriage
Horizontal Springs
Wave Maker

(c) Tank dimensions

Figure 3.3: Experimental model setup (Taken from [32])

During the experimental test was the experimental model utilized with two accelerometers that measured the acceleration in vertical directions, seen from Figure 3.3a. The model is moored with three horizontal spring stiffnesses, Figure 3.3b, where the associated stiffnesses are shown in Appendix C.4. The tank facility and the experimental model location within the tank is shown in Figure 3.3c. The wave generator has only the possibility to generate regular waves. The tank dimensions can be seen in Appendix C.4.

3.3 Post-Processing of Experimental Results

The experimental results were computed during the project thesis, but the post-processing of these results was only done with limited care. A fine post-processing of the experimental results was performed in this Master's thesis, which includes a fine filtering of the experimental result and better representation of the comparison with numerical results. The filtering method was done using a high pass filtering method. The experimental results were represented in a more user-friendly matter, explained in Appendix D.3.1.

Finalization of the data processing makes it possible to perform a comparison study.

3.4 Problems and Observations for the Experimental Model

The experimental model and the tank tests were respectively not designed and performed optimally. This section will address some of these problems and the underlying uncertainty.

The correlation between the full-scale and model-scale model is not correct according to the Froude scaling method. A correct scaling factor is important to establish, to have meaningful values in a comparison study. The Froude scaling method itself has disadvantages and with an uncertain scaling factor, increases this uncertainty.

The measurement system is also insufficiently setup, regarding the magnitude of measurements. This setup has two vertical heave accelerometers at the top of the nacelle, which makes pitch motions useless for nonlinear motions.

The structural oscillation combined with regular waves leads to uncertainties of regular waves. The internal fluid within the torus disturbs the flow field, such that the waves can be expressed as irregular in reality.

Chapter 4

Numerical Modeling

This chapter will go into detail of the numerical modeling, with the relevant software in focus.

The first section, Software Flowchart, will give a brief introduction to the software used in this Master's thesis.

The next sections formulate numerical modeling, in terms of internal and external loads, where the hydrodynamic loads are specified respectively for a Morison's and LPT formulation. The numerical modeling also consists of a determination study of hydrodynamic and structural coefficients. The numerical modeling in term of response formulation will also be presented. In the end, a summary of the numerical modeling will be outlined.

4.1 Software Flowchart

DNV Sesam, 3DFloat and MATLAB are the three programs used in this Master's thesis. The software flowchart is shown in Figure 4.1.

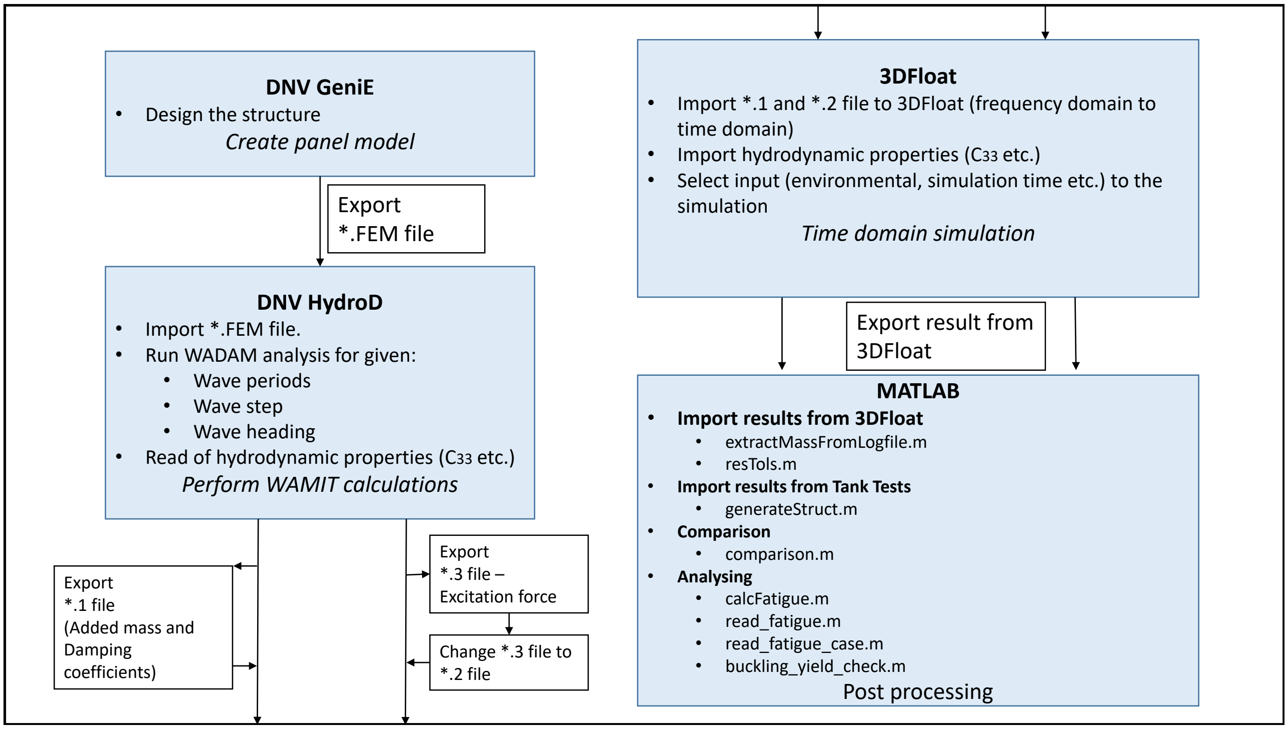
DNV GeniE
Design the structure
Create panel model
Export *.FEM file
DNV HydroD
Import *.FEM file.
Run WADAM analysis for given:
Wave periods
Wave step
Wave heading
Read of hydrodynamic properties (C33 etc.)
Perform WAMIT calculations
Export *.1 file (Added mass and Damping coefficients)
Export *.3 file – Excitation force
Change *.3 file to *.2 file
3DFloat
Import *.1 and *.2 file to 3DFloat (frequency domain to time domain)
Import hydrodynamic properties (C33 etc.)
Select input (environmental, simulation time etc.) to the simulation
Time domain simulation
Export result from 3DFloat
MATLAB
Import results from 3DFloat
extractMassFromLogfile.m
resTols.m
Import results from Tank Tests
generateStruct.m
Comparison
comparison.m
Analysing
calcFatigue.m
read_fatigue.m
read_fatigue_case.m
buckling_yield_check.m
Post processing

Figure 4.1: Flowchart of software

The relevant programs and what these do are illustrated by respectively the bolded and emphasized text, seen from Figure 4.1. The flow chart for a pure Morison's model can be seen by only looking at the right-hand side of Figure 4.1, and not include the WAMIT results.

The LPT formulation uses DNV software GeniE and HydroD to compute the relevant input for hydrodynamic loads in 3DFloat. The panel model, created in GeniE, is exported to DNV HydroD, to calculate the hydrostatic loads and the frequency dependent hydrodynamic loads. The frequency dependent hydrodynamic loads are exported to 3DFloat and transformed such that it is represented by time, such that 3DFloat can run. The hydrostatic coefficients and the relevant environmental input are imported and selected to run a purposeful simulation. A purposeful simulation is a simulation that for instance computes a particular regular wave, decay or irregular wave test. The last program, MATLAB, is used for post-processing the results established in 3DFloat.

A further explanation of the different software and a detailed implementation can be seen in Appendix D.

4.2 Environmental Representation

The waves can either be chosen to be incident regular waves or irregular waves. Regular waves are used for numerical comparison with experimental results from the project thesis [32]. An initial improvement had to be done, in the comparison study. The wave probe was monitored a distance in front of the model-scaled WT during the model test, and this distance should be included in the comparison study. This distance was added as a phase shift to the experimental sea elevation to align the experimental and numerical sea elevation.

The irregular wave representation is used for long-term analysis (FLS and ULS) and is defined by a sea spectrum (Section 2.1.1). The significant wave height H_s and spectral peak period T_p are input to the JONSWAP spectrum, which 3DFloat uses.

The wind representation, described in Section 2.1.2, can either be expressed as uniform or turbulent. Turbulent wind represents the ocean wind best and has been used in 3DFloat for long-term analysis (FLS and ULS), to establish numerical responses. The numerical response comparison with experimental results is performed without wind, to replicate the environmental conditions during tank tests.

The water depth for all numerical analysis in 3DFloat and HydroD is set to be 70 m.

4.3 Hydrodynamic Formulation

The hydrodynamical formulation can either be Morison's or LPT, for the structure w/ and without heave plates. Thus will the focus be for the LPT formulation, since this is the proposed solution to the hydrodynamic problem the foundation faces.

4.3.1 Morison's Formulation

The numerical Morison's formulation is related to the Morison's equation, with elements defined as pure Morison's elements. Each structural element is discretized into many Morison's elements (Gauss points), such that it is possible to establish the forces on each element. These elements are integrated over the whole structure to establish the total load. A finer discretization of the Morison's elements gives a more accurate load, thus increases computational time. The hydrostatic coefficients are also established by 3DFloat calculation, i.e. not an input to the software (in contrary to LPT formulation). Inertia, diffraction and drag loads are computed for all Morison's elements, and the associated coefficients are shown in Table 4.1.

Table 4.1: Definition of hydrodynamic coefficients for Morison's formulation

Drag coefficients	**Torus**	**Colum**	**Heave Plate**	**Connector Tube**
C_{Da}	0.01-0.02	3	1.12	1.12
C_{Dn}	0.9-1.1	0.7	1	1
C_{Ma}	2	2	1.6366	2
C_{Mn}	2	2	1.5	1.5

The connector tube, from Table 4.1, is the element from the torus to the heave plate, C_{Da}, C_{Dn} are respectively drag coefficients in axial and transverse direction, and C_{Ma}, C_{Mn} are the respectively mass coefficients in axial and transverse direction. The C_{Da} and C_{Dn} coefficients for the torus, heave plate and the connector tube is found respectively from [34], [5] and [5].

4.3.2 Linear Potential Theory Formulation

The numerical model with hydrodynamic loads based on LPT uses GeniE and HydroD to establish the hydrodynamic loads. The difference from Morison's contribution compared to the LPT contribution can be seen in Section 2.6.1.2. This formulation uses a combination of Morison's elements, static and dynamic results from HydroD (Uses core program WAMIT). The structural elements are expressed as Morison's elements since drag of each element must be included in the external loads. This means that the drag coefficients from Table 4.1 is included, while the mass coefficients are included from the WAMIT calculations.

The numerical model is created in GeniE on behalf of the input file to 3DFloat. The panel model generator divides the structure into n number of panels, which is the number of panels that hydrodynamic loads will be calculated on. The mesh size and structural properties for the GeniE model are shown in Table 4.2.

Table 4.2: Parameters for GeniE calculations without heave plates

	Tower	**Torus**	**Column**$_{lower}$	**Column**$_{upper}$
Mesh	0.5 m^2	1 m^2	1 m^2	1 m^2
Thickness	45 mm	45 mm	51 mm	45 mm
Total mass			2.3E6 kg	
Center of Gravity			23.95 m (z-axis)	

The total mass of the structure must be evaluated with the buoyancy force, according to Archemides law. The plate thickness on the lower part of the column is therefore changed from 45 mm to 51 mm to achieve equilibrium at the sea surface. The change in plate thickness is to account for not taking the spokes into consideration, explained in Appendix D.1. The hydrodynamic and hydrostatic loads varies for a structure w/ and without heave plates. A panel model in GeniE for a structure w/ and without heave plates must be designed in order to perform time-domain analysis. The structure w/ heave plates follows more or less the same values as in Table 4.2.

The hydrostatic and hydrodynamic loads are calculated by WADAM (DNV sub-program), which uses the WAMIT core program to calculate the static and dynamic load coefficients. These models are shown in Figure 4.2.

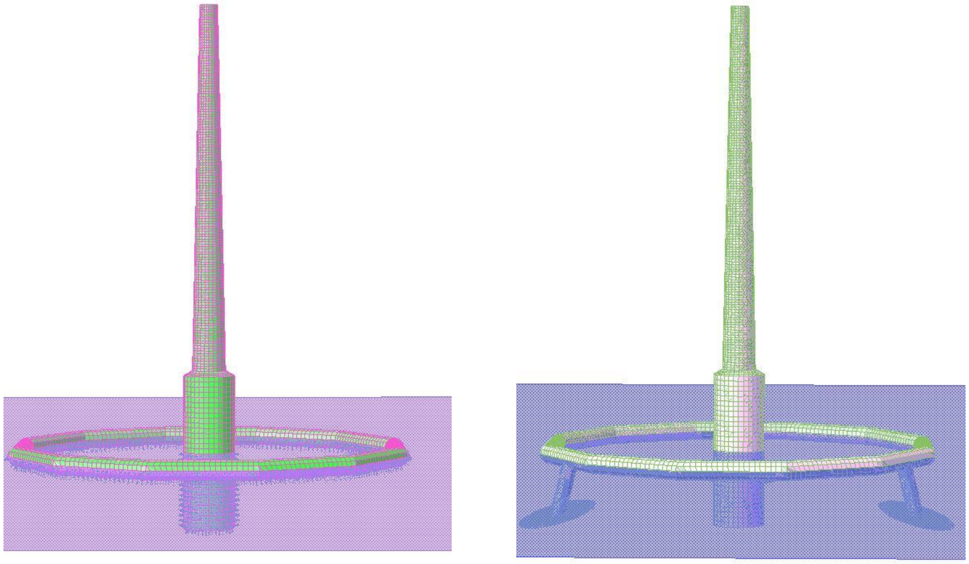

(a) Model

(b) Model with heave plates

Figure 4.2: GeniE/HydroD model with and without heave plates

The establishment of the hydrostatic and frequency dependent hydrodynamic coefficients can be seen in the next two sections.

4.3.2.1 Hydrostatic Coefficients

The hydrostatic coefficients are explained in Section 2.2.1. The water plane stiffness, C_{33}, roll and pitch moment stiffness, C_{44} and C_{55}, are exported from HydroD to 3DFloat and applied at the center node of the FO OFWT center node. The center node is at MLS (0,0,0) for the structure in 3DFloat. The coefficients are approximately the same for the structure w/ and without heave plates, and are listed for both structures in Table 4.3.

Table 4.3: Hydrostatic coefficients

	$\mathbf{C_{33}}$	$\mathbf{C_{44}}$	$\mathbf{C_{55}}$
Without heave plates	9e6 [N/m]	5.1e9[N/deg]	5.1e9[N/deg]
With heave plates	8.9e06 [N/m]	5.04e09[N/deg]	5.04e09[N/deg]

4.3.2.2 Hydrodynamic Coefficients

The hydrodynamic coefficients consist of the frequency dependent radiation and diffraction force. The radiation force consist of frequency dependent added mass and damping forces, while the diffraction force depends on the incident velocity potential and the scattered diffraction potential. This is respectively explained in Section 2.2.3.1.2 and 2.2.3.1.1. The problem with frequency dependent coefficient must be solved for usefulness in the time-domain generator 3DFloat. The Laplace transformation is introduced, seen by Equation 2.36, to go from frequency-domain to time-domain.

The numerical model from GeniE is exposed to numerous wave test in HydroD to cover the frequency dependent hydrodynamic coefficients for all wave periods and heading angles. The numerous wave tests used for this Master's thesis are shown in Table 4.4.

Table 4.4: Wave cases in HydroD

	Start	**Stop**	**Increment**
Wave periods [s]	0.1	40	0.1
Heading angles [deg]	0	345	15

The hydrodynamic coefficients for these runs are calculated by the WAMIT software and exported to a *.1 (radiation) and *.3 (diffraction) file. The necessary input to 3DFloat can only be the excitation force (diffraction) based on the velocity potential from the haskind relation, denoted as *.2 file. The excitation force is according to [21] independent on whether the diffraction velocity potential or the haskind relation is used to solve the diffraction problem. Since either method solve the problem, was the solution to change the *.3 file to a .*2 file. The setup of these two output files from 3DFloat are the same.

The added mass coefficients at infinite frequency cannot be established in HydroD, but an approximation has been used by running a wave case with $\omega = 150$ rad/s. The added mass matrices at infinite frequency, w/ and without heave plates, are shown in Appendix D.5.

4.3.3 Determination of Constant Hydrodynamic Coefficients

The constant hydrodynamic coefficients consist of drag, linear damping, and quadratic damping coefficients. The drag coefficients are determined based on knowledge for the torus and the column, while the linear and quadratic damping coefficients are determined randomly.

The drag coefficients interval for the torus was introduced in Table 4.1, and are established through e-mail correspondence with Professor Trygve Kristiansen [34]. The transverse drag coefficients should be in the range of 0.9-1.1, while the axial drag coefficient should be in the range of 0.01-0.02. The axial drag coefficient at column base and the axial drag coefficient for heave plate are held constant during the variation of other hydrodynamic coefficients. The axial drag coefficient at tower base is established to be 3, based on [9].

A nonlinear system does not capture all loads exposed to the structure. The external loads and the structural motions are assumed to be too great, and the solution is to reduce these loads by applying linear and quadratic damping coefficients. These linear and quadratic damping coefficients are dependent on respectively the velocity and the velocity squared. The damping coefficients are applied to the MSL point with random values. The constant hydrodynamic coefficients are established on behalf of a heave decay test, Section 6.1.1.1, where the combination of the hydrodynamic coefficients that gives the best correspondence with experimental results are chosen.

A thorough establishment of the hydrodynamic coefficients can be seen in Appendix D.6.1. The finalized values are shown in Table 4.5.

Table 4.5: Constant hydrodynamic coefficients

	$\mathbf{C_{Da}}$	$\mathbf{C_{Dn}}$
Torus	0.01	0.9
Column	3	0.7
Connector tube	1	0.7
Heave plates upper	0	0.7
Heave plates lower	1.16	0.7
Spokes	0.7	1.1
	$\mathbf{B}_{\text{linear}}$	$\mathbf{B}_{\text{quadratic}}$
Heave	9e5 [Ns/m]	9e5$[Ns^2/m^2]$
Pitch/Roll/Yaw/Surge/Sway	0	0

The axial drag coefficient for the heave plates is shown to be divided into an upper and lower drag coefficient, Table 4.5. It is due to the heave plate length of 40cm, and by applying a drag force on both sides would lead to double amount of drag forces from the heave plate.

4.4 Aerodynamic Formulation

The aerodynamic loading in 3DFloat uses an unsteady BEM model (Section 2.3.3) to establish torque and moment at the rotor. The unsteady BEM model takes dynamic inflow and yaw errors into consideration, making the aerodynamic formulation accurate.

The wind turbine in 3DFloat uses codes from the IEA OC3 project for a 5MW rotor created by NREL [40]. The wind turbine model in 3DFloat is based on studies done in [25] at NREL. A very detailed description of the blades and the rotor are defined in the input file, based on the work done in [25]. The 5MW turbine can, according to [25], produce 5MW of power, and has a cut-in, rated and cut-out wind speed of respectively 3 m/s, 11.4 m/s and 25 m/s. The wind turbine consists of three blades and has a rotor diameter of 126 m.

The pitch controller is also created by the OC3 project that uses a variable-blade-pitch-to-feather

[24] controller, that pitches the blades such that the optimal amount of power is generated. The thrust force is, furthermore, dependent on the pitching angle.

4.5 Mooring Line Formulation

The mooring lines were not modeled as catenary mooring lines during experimental tests[32], but as springs in the horizontal direction. This means that during linear motions are all stiffness coefficients the spring stiffness. The author wanted to replicate the experimental setup as good as possible, and the mooring lines during numerical analysis are, therefore, applied as virtual springs. The mooring line formulation can be seen in Figure 4.3.

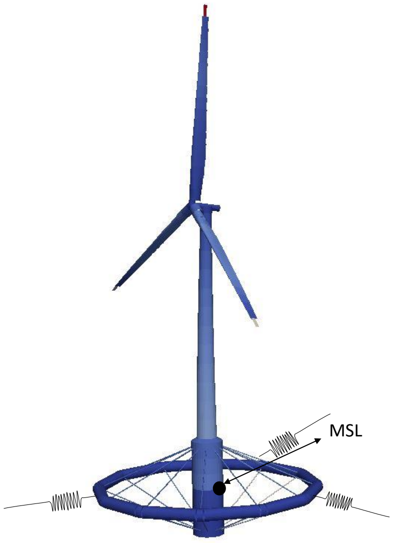

Figure 4.3: Mooring line formulation of the numerical model

The external force that arises from the applied mooring lines in 3DFloat are shown in Equation

4.1a. The stiffness coefficients in **K** are based on the spring stiffnesses in Eqns. 4.1b - 4.1f.

$$\mathbf{F}^{\text{Mooring Lines}} = -\mathbf{K}\eta \tag{4.1a}$$

$$k_{11_x} = 17201[N/m] \tag{4.1b}$$

$$k_{22_x} = 11749[N/m] \tag{4.1c}$$

$$k_{22_y} = 20350[N/m] \tag{4.1d}$$

$$k_{33_x} = 11749[N/m] \tag{4.1e}$$

$$k_{33_y} = 20350[N/m] \tag{4.1f}$$

These stiffness coefficients are based on that the structure will have a natural period of 60 s in surge and sway. That is why the mooring contribution to the stiffness matrix, Table 4.1, are established to have these values. The stiffness for the model-scale and full-scale horizontal mooring lines are shown in Table C.5 in Appendix C.4.

4.6 Structural Formulation

The structural calculation is done by the program 3DFloat. Responses to structural elements are based on nonlinear beam theory, where 3DFloat defines an element as a Euler-Bernoulli beam with 12 DOFs [40]. This is the case for a numerical model that contains pure Morison's elements. External loads are computed at each Morison's discretized element, such that there exist a deflection and rotation. However, this is not the case for a structural model based on LPT. 3DFloat turns buoyancy off for all elements, such that internal deflections and rotations are useless for the 3DFloat calculations on these elements. However, the tower, nacelle, rotor, and blades are modeled as flexible, making the loads at these parts analyzable. This makes it, for instance, possible to calculate fatigue for the tower base, as will be done in Chapter 7.

A disadvantage of modeling the whole structure as flexible is that structural damping must be included. The structural damping is established by Rayleigh damping method, which is a combination of the mass and stiffness matrix, explained in Appendix D.6.2. The factors which are multiplied with the mass and stiffness matrix can be obtained either by a Eigenvalue analysis or by a determination study. In Appendix D.6.2 are the structural damping coefficients determined from a regular wave case with wave height of 1.8 meters and wave period of 10 seconds. The Rayleigh damping coefficients that gives the best correspondance with experimental results are shown in Table 4.6.

Table 4.6: Structural damping coefficients

α	β
0	0.016

4.7 Response Formulation

The response formulation carries out how the equation of motion is solved, and how the design checks are performed.

4.7.1 Equation of Motion

The equation of motion is obtained by requiring equality between the external and internal loads. The equation of motion is represented in time by using the retardation function, explained in Section 2.6.1.1. The time-domain simulation uses a HHT-α method for establishing the new responses after a time step dt. This method is described in Section 2.6.2.

4.7.2 Design Checks

The structural stability requirements for FLS check is described in Section 2.8.1. The FLS study requires that the cumulative damage shall be computed for the operational lifetime. The lifetime is often represented by various sea states, k, which describes the sea condition for a specific site. The fatigue damage D_k is established as the mean of two simulations, to account for the statistical variation between two sea states with the same environmental input. The cumulative fatigue damage is calculated using the Wave Analysis Fatigue and Oceanography (WAFO) package, based on Rainflow counting method, in the script read_fatigue.m.

The structural stability requirements for ULS check is described in Section 2.8.2. In ULS calculations are all loads in the requirements defined by design loads. In this Master's thesis are the permanent load taken as the load from when the structure is freely floating on the sea surface (static load), while the environmental load is considered as the environmental load minus the mean static load. The combination of the design load that gives the largest load is used in ULS calculations. The largest response, input to the design loads, is established by performing a time-domain simulation for several worst sea states. A 3-hour simulation is often sufficient for establishing the maximum load, for the worst sea state. Thus, it is not sufficient to compute 1 simulation since there exist statistical variation between different numerical runs with the same input. The 3-hour simulation can, therefore, be run several times in order to establish a mean maximum load, based on the number of tests performed. It is in most cases sufficient for 5 cases, to establish the mean maximum load.

4.8 Summary

The creation of the numerical model had the focus of implementing LPT. Thus are the Morison's formulation expressed as well, due to the comparison study in Chapter 5. The numerical LPT model represents the diffraction/radiation problem better, which is the main advantage for this numerical model. The mooring lines are modeled as virtual spring for comparison and long-term analysis, even though this mooring line setup is only meant for comparison study. In other words, the catenary mooring lines should be used for long-term analysis. The rotor, on the other hand, is represented as an equivalent top mass and the full NREL-5MW for comparison and long-term analysis, respectively. The rotor formulation represents in a way what the mooring lines do not. The reason for modeling this way is due to the many uncertainties, regarding fatigue for the lines, of having a catenary mooring line system. The rotor works in a more simple way.

This Master's thesis takes the experimental and the numerical *start-up* dimensions as the final dimensions for further analysis. This assumption is chosen, since this was the only possible knowledge base without performing any design changes.

The design checks are performed according to the DNV recommended practice, and are established in Chapter 7 and 8.

Chapter 5

Comparison of Numerical Morison's Model and Experimental Model

This chapter will outline a comparison study between the numerical Morison's model and the experimental model, where the numerical model is formulated with pure Morison's elements. The aim of this chapter is to observe the discrepancies between the numerical Morison's model and the experimental model, to judge the numerical model, presented in Chapter 6. On behalf of previous work and the well-known discrepancies will the comparison be made briefly.

The numerical model formulation is described in Section 4.3.1, for flexible elements (Morison's). The numerical model obtains the loads on each flexible element, and the hydrodynamic excitation forces consist of the inertia and drag force, as presented in Section 2.2.3.2.

This chapter includes a comparison of one heave decay test and three regular wave tests. These will be compared with experimental tests for decay and regular waves performed by respectively FO and the author. The comparison of the experimental and numerical results will be based on theory for the numerical model and visual observations for the experimental model.

5.1 Decay Test

Decay tests are seen as the most important test for numerical and experimental comparison. It is because it investigates the general behavior of the structural motion and it establishes the structural natural period.

It is of great importance that the numerical and experimental natural periods corresponds well, since this means that the software is implemented correctly. It is in addition important for comparison of RAO's and regular waves in further comparison study. The natural periods established in the project thesis [32] for heave and pitch (linear and nonlinear) are shown in Table 5.1.

Table 5.1: Natural periods for the FO OFWT concept (Taken from [32])

$\mathbf{T_{nn}}$	**Linear exp. [s]**	**Nonlinear exp. [s]**	**Lin/nonlin num. [s]**
Heave	3.4	4	4.62
Pitch	8.2	9.6	7.5
Heave with heave plates	6.9	10.6	-

It is observed that natural periods in heave w/ heave plates and pitch without heave plates are within 1^{st} order wave frequency interval. The natural period for pitch has many uncertainties due to many uncertainties in the measurement system, described in Section 3.4. This is why the pitch natural period w/ heave plates is not included.

5.1.1 Heave Nonlinear

The decay test comparison in heave for nonlinear motions with a Morison's representation is outlined in this section. The experimental test is performed by FO and the associated measurement uncertainties and limitations are unknown. The heave decay acceleration for the numerical and experimental model is shown in Figure 5.1.

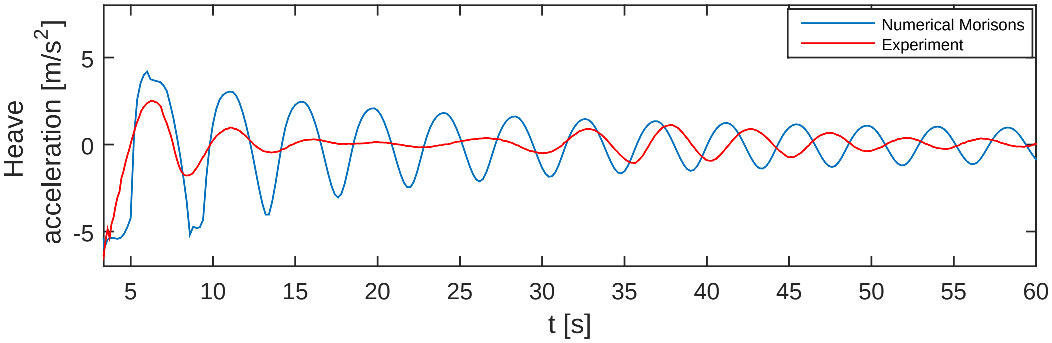

Figure 5.1: Heave nonlinear decay analysis done by Fred. Olsen

It is observed that the numerical results represent the experimental heave acceleration poorly during this decay analysis. The natural period is established to be 4.2 s for the numerical model, while 3.8 s for the experimental model, which differs from the Table 5.1. The damping for the experimental model is significant, and the numerical model does not capture this effect. The heave acceleration for the numerical model seems to have a constant damping ratio since the correlation between two adjacent peaks is more or less the same. The experimental decay test has a significant damping before it increases (time 30s - 50s), which is also noted. The numerical model does not account for this observation. The peaks for the experimental and numerical models are aligned to some degree for the first two peaks, while the peaks for oscillation from 30 to 60 s are shifted to the right.

5.2 Regular Wave Test

The numerical Morison's formulation will be compared to the experimental results for regular wave motions. The heave acceleration and the sea elevation are the two parameters that will be considered. The heave acceleration from the experimental tests is not influenced by the scaling factor, and the sea elevation is used for aligning the numerical heave acceleration with the experimental heave acceleration. This is is valid for Chapter 6 as well.

The numerical Morison's model will be compared with three experimental regular wave tests. These three regular wave tests are selected out from a set of five regular wave tests since these three tests illustrate a linear, semi-linear and a very nonlinear case. The rest can be found in Appendix E. A comparison study w/ heave plates for the numerical and experimental model will not be presented for the Morison's formulation.

5.2.1 Case 1 - Linear

Case 1 is a regular wave test with a wave height of 1.05 m and wave period of 14.5 s. Heave acceleration and the sea elevation are shown in Figure 5.2.

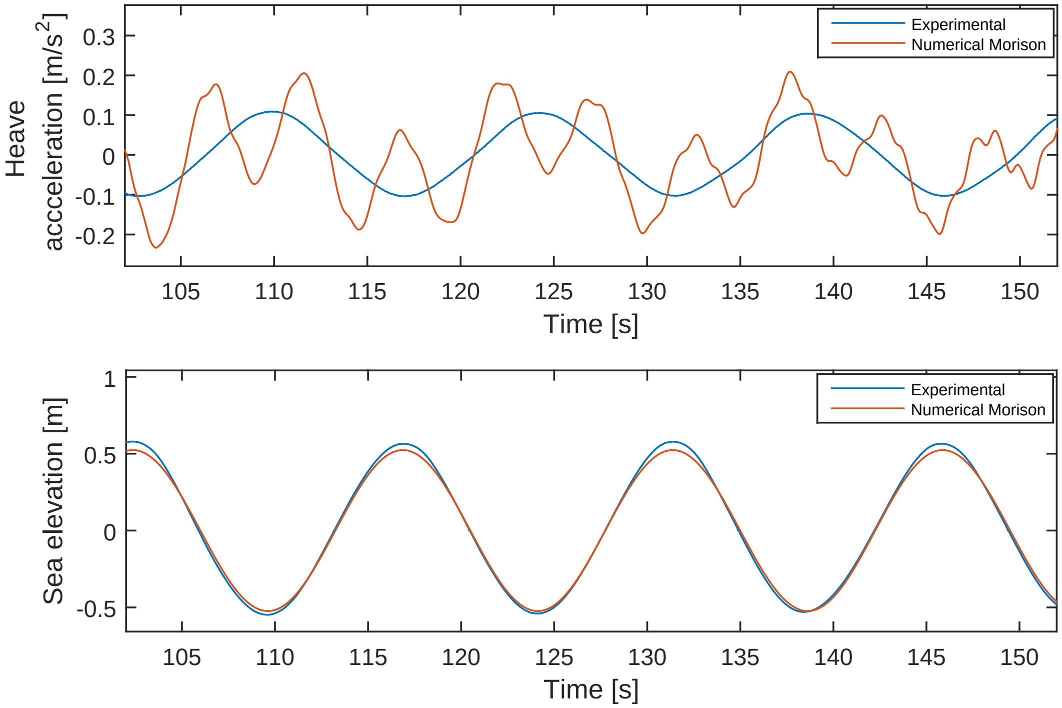

Figure 5.2: Comparison of case 1

The comparison case, illustrated in Figure 5.2, represents a linear case due to the small wave height and a long wavelength. The heave acceleration is observed to have a distinct offset, oscillating around the experimental heave acceleration. The heave acceleration peaks are also too large, compared to the experimental heave acceleration.

5.2.2 Case 2 - Semi linear

Case 2 is a regular wave test with a wave height of 1.8 m and wave period of 10 s. Heave acceleration and the sea elevation are shown in Figure 5.3.

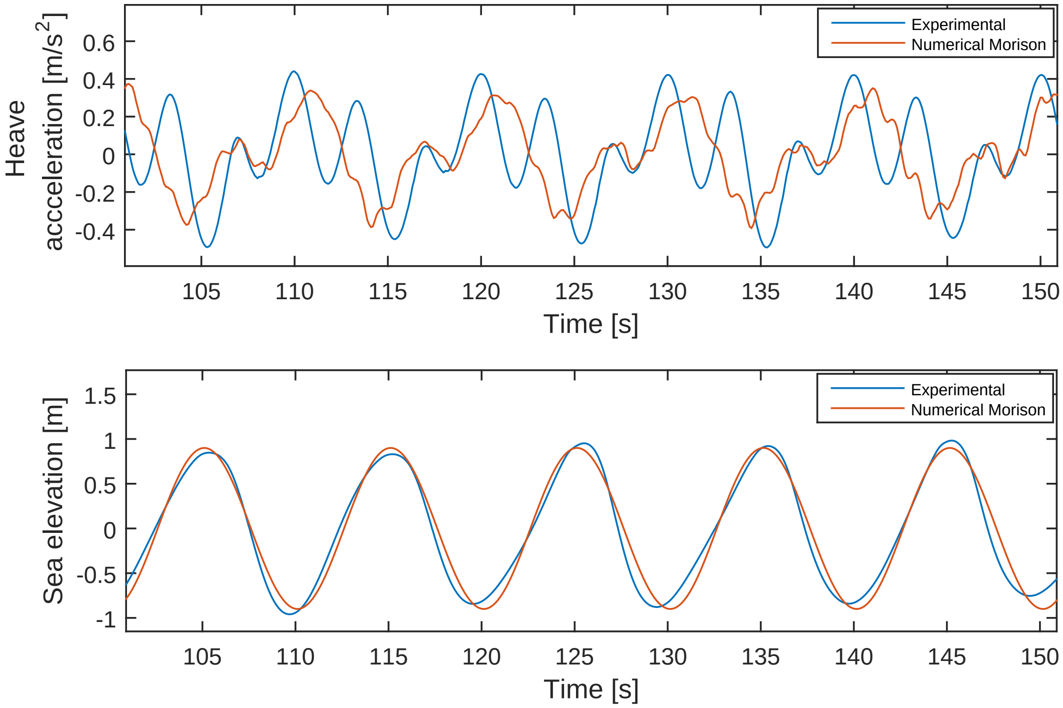

Figure 5.3: Comparison of case 2

The comparison case, shown in Figure 5.3, represents a semi-linear case. It is observed that the numerical heave acceleration differs from the experimental heave acceleration. The maximum numerical acceleration is approximately 16.5 % less than the experimental maximum heave acceleration. The experimental heave acceleration observes three peaks (107s,110s,114s) where the numerical heave acceleration only observes two (107s,112s). The max peak accelerations are also delayed with 1.5-2 seconds, seen from the shift to the right of the maximums.

5.2.3 Case 3 - Nonlinear

Case 3 is a regular wave test with a wave height of 6.2 m and wave period of 9 s. Heave acceleration and the sea elevation are shown in Figure 5.4.

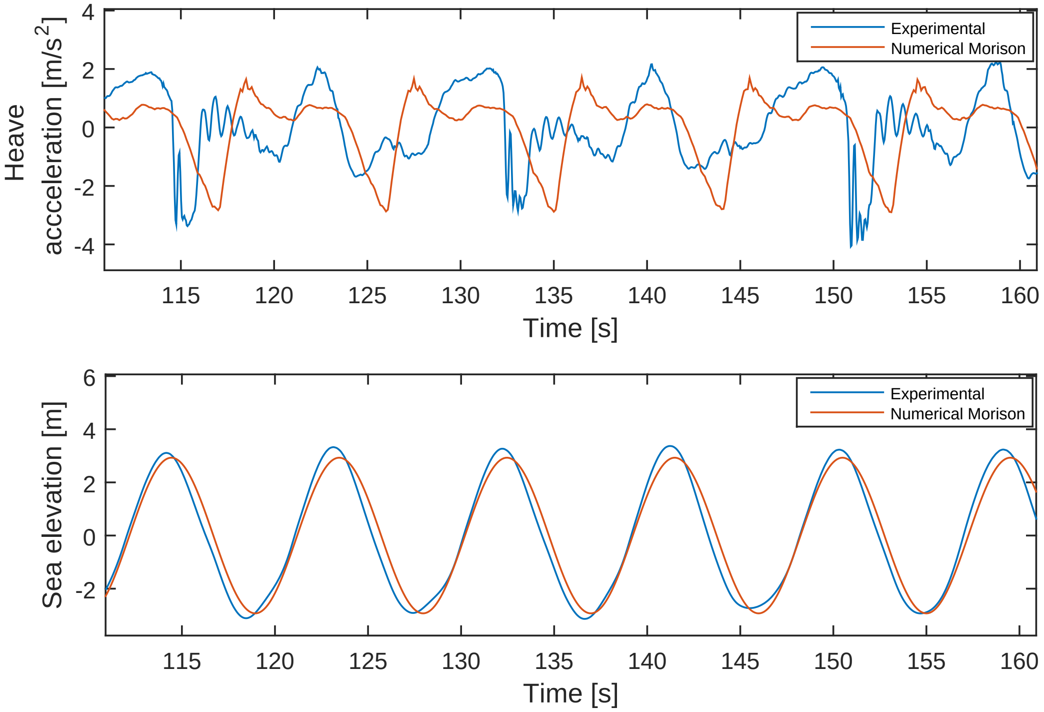

Figure 5.4: Comparison of case 3

The comparison case, shown in Figure 5.4, represents a nonlinear case. It is observed that the numerical heave acceleration has the same maximum and minimum magnitude as the experimental test, even though it differs to a great extent. The numerical behavior does not match the experimental behavior for heave acceleration, where the minimums and maximums are shifted to the right. It is observed from the figure that the experimental model is exposed to vibration at 117, 135 and 154 s, where the experimental structure most likely undergoes large damping. It is observed that the numerical model does not account for this effect since the numerical model peaks are at a larger magnitude.

It is observed that the experimental heave acceleration oscillates with double the numerical period. This oscillation is most likely due to the nonlinear effects during experimental oscillation. This effect is not included with the numerical Morison's heave acceleration either, where it is seen that the same acceleration repeats for each regular wave period.

5.3 Discussion

The Morison's representation for hydrodynamic loads are often used for structures with a small cross section compared to the wavelength, as presented in Section 2.2.3.2. This structure does have a small cross section relative to the wavelength, but the total volume close to the sea surface is large for this model. The initial thought of using Morison's equation for establishing the hydrodynamic loads was that it would differ from the real representation, and the previous sections within this chapter confirm this thought.

The heave decay test was compared with experimental data performed by FO. There lie uncertainties behind these measurements, but since their measurement system is only used for comparison one time, will these uncertainties be discarded. The numerical heave decay test was observed to differ from the experimental results. There are two reasons for this occurrence: The added mass is not frequency dependent, and there is no potential damping. This is seen directly from Morison's equation (Section 2.2.3.2), where the inertia force (added mass) is dependent on the fluid particle acceleration of time, and the damping is dependent on the difference between the fluid particle velocity and the structural velocity of time (drag). The natural period in heave differs with approximately 0.4 seconds, due to the incorrect calculation of hydrodynamic loads. The large damping during the first oscillation and the increase of acceleration later in the time series, seen from Figure 5.1, is clearly due to the lack of potential damping and frequency dependent added mass. The potential damping implementation to the numerical model will play a significant role in obtaining a better correspondence with the experimental results. The heave acceleration for the Morison's representation reduces percent wise through each cycle, i.e. the damping ratio is constant. A constant damping ratio is valid for structures such as spars, but where the radiation of waves from a structure becomes important will a constant damping ratio be insufficient.

The regular wave comparison cases have a direct connection to the decay tests. If the decay test comparison is good, is the regular wave comparison good. The regular wave case comparison is not okay, and the reason is connected to the reasoning in the latter paragraph. The numerical heave acceleration of case 1, the linear case, has an oscillation around the experimental line, which is a clear sign that Morison's formulation is a poorly formulation to the linear problem. The numerical heave acceleration for case 2 and 3, respectively the semi- linear and nonlinear case, do have a distinct offset for maximums and minimums with both amplitudes and phase angles. The amplitudes and the phase angles for the numerical heave acceleration differ from the experimental cases, due to the potential damping and added mass problem.

The Morison's formulation also assumes that the water plane area is constant during decay and regular wave tests. This assumption is violated for all nonlinear cases since the water plane changes drastically when the torus goes in and out of the water. The effect of violating the linear assumption is hard to address for these decay and regular wave cases since the overall hydrodynamic formulation is poor.

The Morison's representation of the hydrodynamic forces calculates the structural motions incorrectly, and a new hydrodynamic formulation must be implemented to see whether another method is better than the latter (Morison's). The comparison study of the new hydrodynamic formulation is the content for the next chapter.

Chapter 6

Comparison of Numerical LPT Model and Experimental Model

The aim of this chapter is to evaluate and judge how good the numerical LPT model represents measurements from the experimental model. The numerical LPT model is created according to Chapter 4, where the numerical LPT model is replicated to the experimental model as good as possible. The reader must understand the limitations of the numerical LPT model, concerning scaling method and nonlinear motions, as presented in Section 4.8.

The comparison study in this chapter contains a comparison of decay tests, regular wave tests, and RAOs for the experimental and numerical LPT model. The natural periods are compared for decay tests, heave accelerations comparison for regular wave test and heave displacement for RAOs. The decay tests will compare acceleration and displacement for heave and pitch motions. The comparison of the experimental and numerical results will be based on theory for the numerical LPT model and visual observations for the experimental model.

The setup of this chapter contains results and discussion for each comparison type before a discussion summary is established in the end. The discussion will discuss linear and nonlinear motions separately.

6.1 Decay Tests

The decay test introduction is presented in Section 5.1, for the Morison's formulation of hydrodynamic loads. The same statements are valid for the comparison of the decay tests with the LPT formulation of hydrodynamic loads.

The decay test will be performed for heave, pitch and heave w/ heave plates in the next sections. The experimental test for decay is performed by the author, in contrary to what was done for the Morison's formulation in Section 5.1.1.

6.1.1 Heave

Heave decay test will be performed for linear and nonlinear motions. Linear motions are assumed when the water plane area is constant, and nonlinear motions are assumed when this is violated.

6.1.1.1 Linear

The heave acceleration and heave displacement for a decay analysis with an offset of 0.74 m are shown in Figure 6.1.

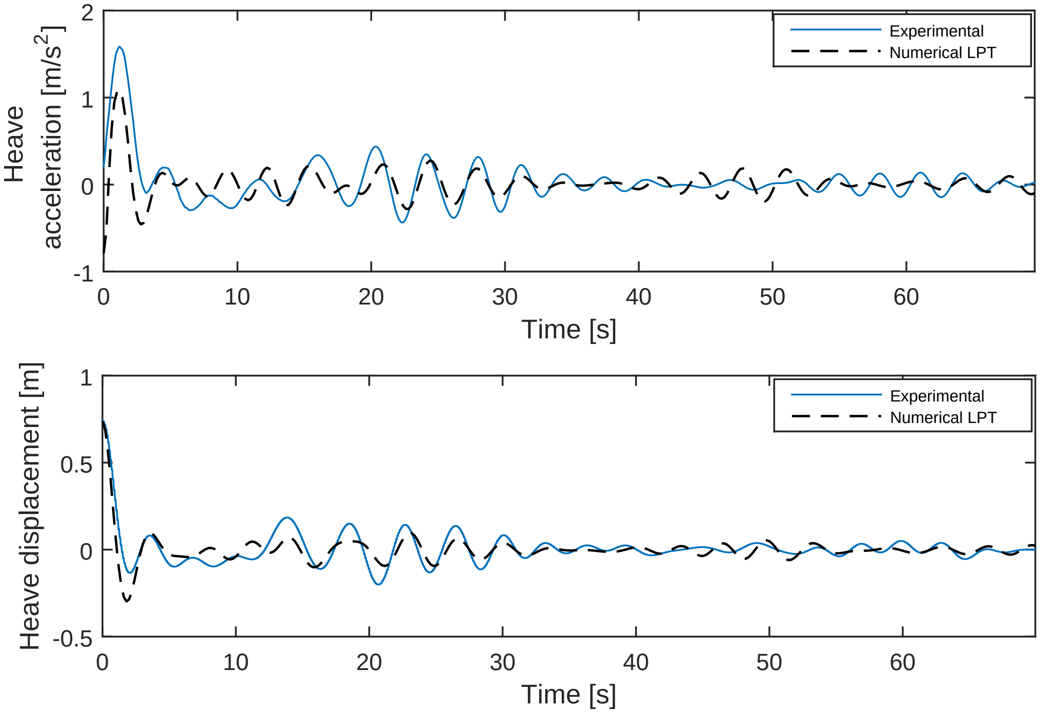

Figure 6.1: Linear decay heave motions

The experimental and numerical results show good correspondence. The significant reduction of the position after half a cycle, due to a large hydrodynamic damping, is captured to some degree by the numerical LPT model even though the minimum after half a cycle is greater than for the experiment. It is observed that the peak after one oscillation is at the same time instant for numerical and experimental data. This time instant is at 3.4 s, which corresponds well with the natural periods listed in Table 5.1.

A following flat heave displacement and acceleration behavior after the rapid damping during the first oscillation is observed for the numerical LPT model. This effect is obtained by both the numerical and experimental computation, even though the oscillations does not peak at the same time instant for experimental and numerical values.

It is observed that the heave acceleration and heave displacement are excited after 10 s, in Figure 6.1. The same occurrence happens for the time interval between 45s and 50s.

6.1.1.2 Nonlinear

The nonlinear decay analysis is performed by submerging the whole torus during offset. This results in a very nonlinear case during the experimental test where the water plane changes and higher order fluid effects occur. The heave acceleration and heave displacement for a decay analysis with an offset of 4.132 m are shown in Figure 6.2.

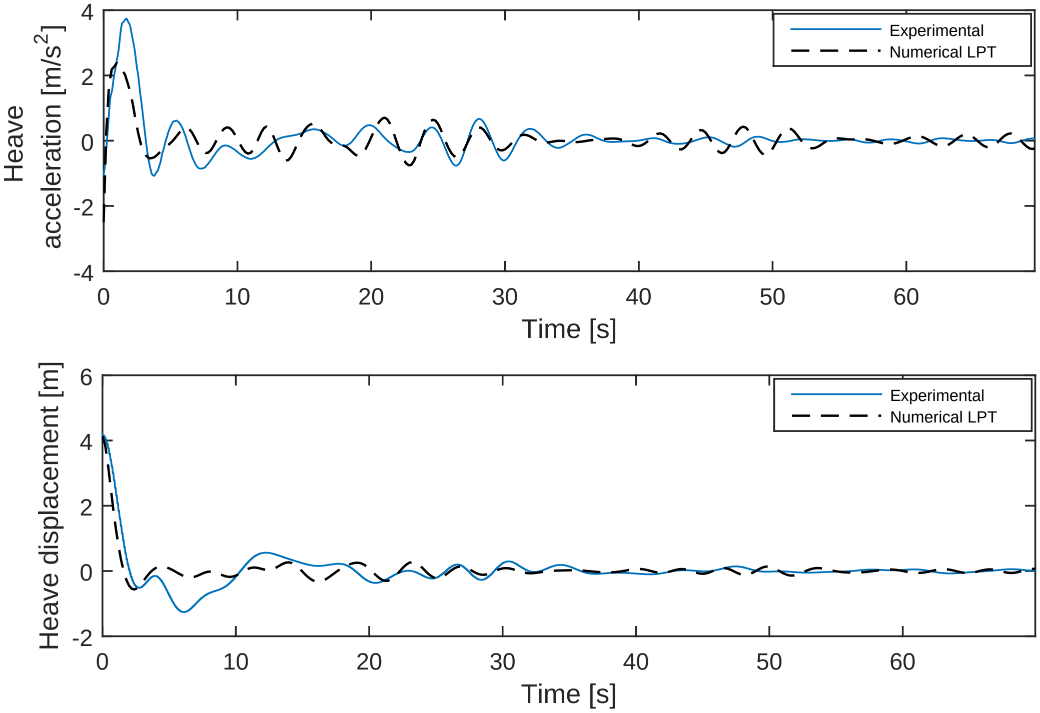

Figure 6.2: Nonlinear decay heave motions

It is observed from Figure 6.2 that the nonlinear case does not correspond as good as the linear case in Section 6.1.1.1. The numerical LPT model decays faster, in terms of seconds, than the experimental model during the first half oscillation. The second part of the first oscillation oscillates the numerical LPT model slower than the experimental model for heave motions. Nevertheless, this results in a nonlinear natural period for heave motions of 4 and 4.4s for respectively experimental and numerical LPT model.

Further, it is observed that the heave displacement picks up at the time interval between 20 and 30s. The amplitude for both heave acceleration and heave displacement are aligned with the experimental motions, at this time interval. The heave acceleration and heave displacement are repeated at 40- 55 s. It is observed from the numerical motions at this time interval that the magnitude is larger than the experimental amplitude. The heave natural period is established to be 3.6 s, at this time interval, for both numerical and experimental heave motions, which is closer to the linear natural period.

6.1.2 Pitch

Pitch decay test will be performed for linear and nonlinear motions. Nonlinear motions are not reliable. Thus, it will be presented.

6.1.2.1 Linear

The linear pitch decay case has a fixed rotation of 0.3 degrees before it is released. The linear pitch decay test is shown in Figure 6.3.

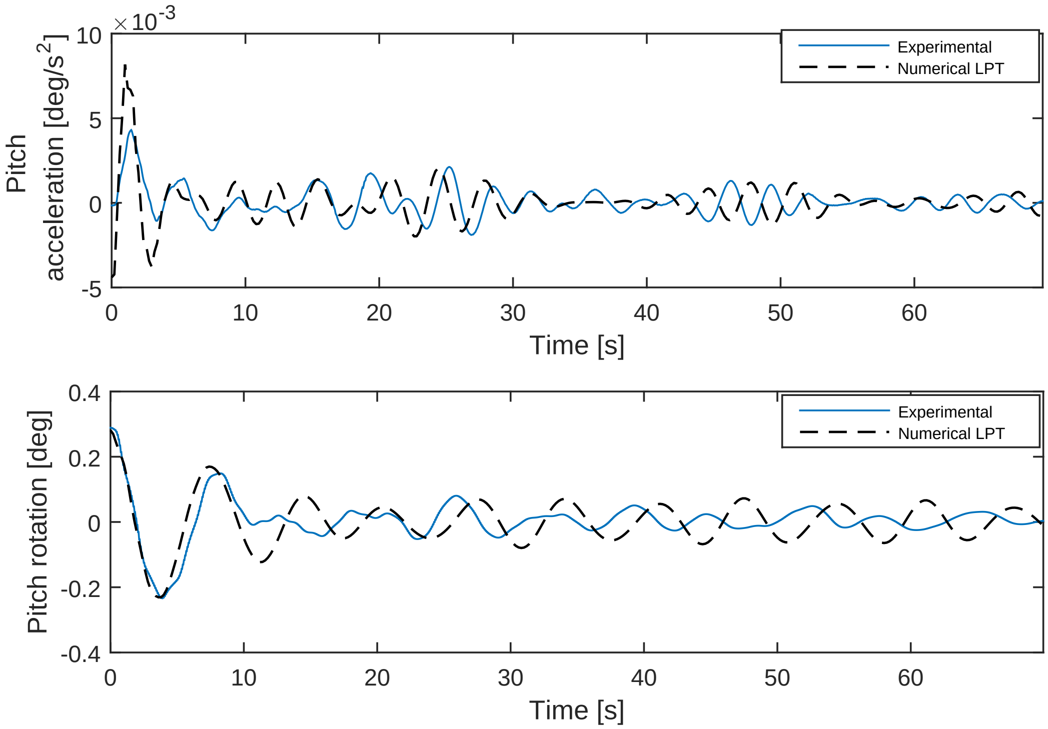

Figure 6.3: Linear decay pitch motions

The pitch position for experimental and numerical decay test have an offset to some extent for all measurements. For the first oscillation is the numerical pitch motion shifted 0.8 s to the left, while the amplitudes correspond well. The linear pitch natural periods are determined to be 8.2 s and 7.4s respectively for the experimental and numerical LPT model.

The numerical pitch rotation is shifted to the right from 20 to 70 s. The numerical pitch rotation is to some degree higher than the experimental pitch position between the same interval. Thus is the difference not large enough for including constant hydrodynamic damping coefficients.

6.1.2.2 Nonlinear

The nonlinear pitch decay test has a fixed rotation of 0.814 degrees before it is released. Pitch acceleration and pitch rotation are shown in Figure 6.4.

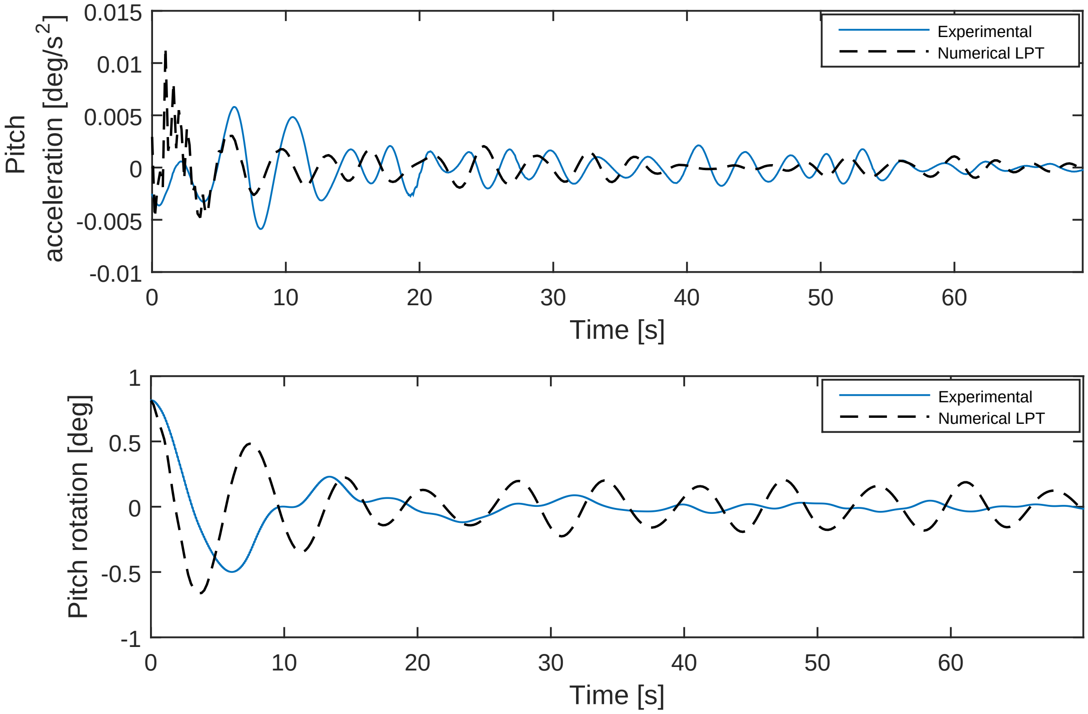

Figure 6.4: Nonlinear decay pitch motions

The numerical and experimental data deviates in a far larger magnitude than it did for the pitch linear case, even though the pitch angle is still small. It is observed from Figure 6.4 that the natural periods in pitch are 9.6s and 7.4s for respectively the experimental and the numerical responses. The numerical natural period is observed to be the same as for the linear case. The experimental natural period is observed to increase for larger motions.

It is also observed that the numerical amplitudes for the whole time series are larger than the amplitudes for the experimental model.

6.1.3 Heave with Heave Plates

Heave decay tests w/ heave plates will be performed for linear and nonlinear motions.

6.1.3.1 Linear

The heave linear case w/ heave plates has an offset of 0.87 m before it is released. The heave acceleration and displacement are shown in Figure 6.5.

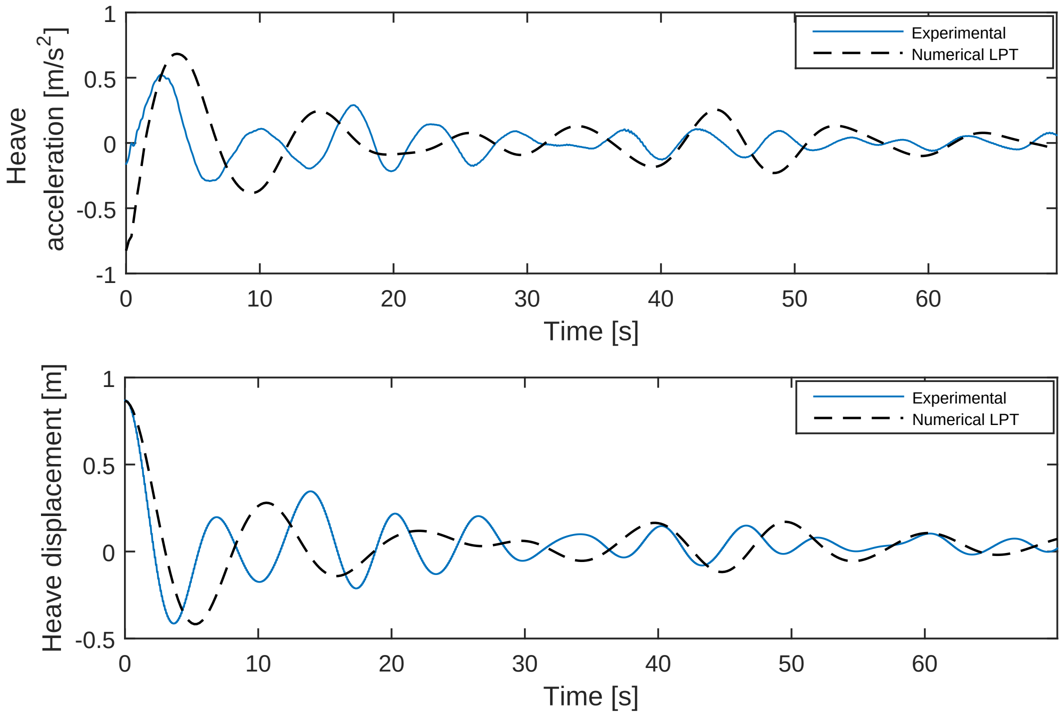

Figure 6.5: Linear decay heave motions with heave plates

Figure 6.5 illustrates that the numerical values deviates from the experimental values. It is observed that the heave acceleration and heave displacement are shifted to the right for the numerical results, compared to the experimental decay results. It is observed that the heave natural periods w/ heave plates are 6.9 s and 10.6s, respectively for the experimental and numerical motion. It is, in addition, observed that the numerical decay line does not oscillate in the same phase as the experimental model.

6.1.3.2 Nonlinear

The heave nonlinear case w/ heave plates has an initial offset of 2.54 m. The heave acceleration and displacement are shown in Figure 6.6.

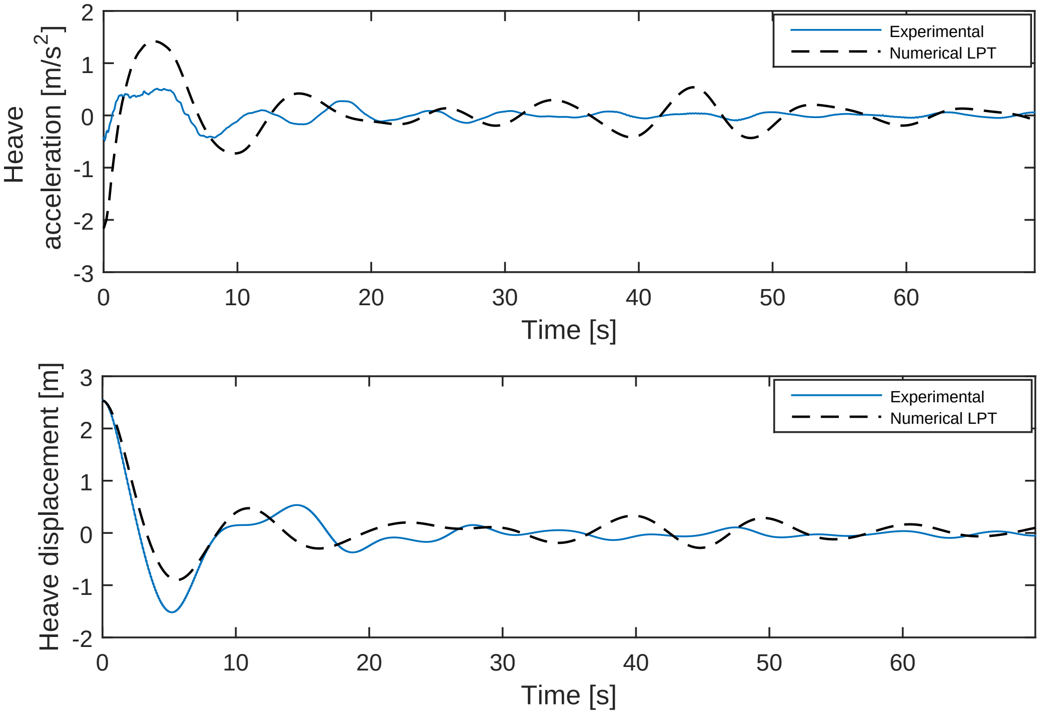

Figure 6.6: Nonlinear decay heave motions with heave plates

The experimental and numerical heave acceleration and heave displacement correspond better than it did for linear motions w/ heave plates. It is observed that during the half first cycle that the minimum occurs at the same time instant for numerical and experimental heave values. It is observed that the second part of the first oscillation peak is shifted to the left. The heave natural periods are therefore respectively 9.7 s and 10.6s for experimental and numerical response. It is seen that the damping during the first cycle is too great for the numerical decay, compared to the experiment. The experimental heave acceleration observes a vibrational behavior during the first oscillation.

It is also observed that, even though the damping is large during the first cycle, the oscillation amplitudes are larger for the numerical case for time 30s to 70 s, for both heave acceleration and position.

6.1.4 Updated Natural Periods

The experimental natural periods does not change compared to Table 5.1. Thus, the numerical natural periods are changed with the LPT formulation. The updated natural periods for experimental and numerical results are shown in Table 6.1.

Table 6.1: Updated natural periods

Nat. period	**Linear exp.**	**Linear num.**	**Nonlinear exp.**	**Nonlinear num.**
T_{33} [s]	3.4	3.4	4	4.4
T_{44} [s]	8.2	7.4	9.6	7.4
T_{33} w/ heave plates [s]	6.9	10.6	9.7	10.6

This table shows that the natural period in heave for numerical linear motions is the same as the experimental. However, the nonlinear heave natural period has increased for both experimental and numerical results. The experimental heave natural period may be correct, but it is strange that the heave nonlinear natural period differs from the linear natural period for numerical results.

It is also observed, from the same table, that the numerical pitch natural periods are smaller for both linear and nonlinear motions compared to the experimental results.

6.1.5 Discussion

This discussion contains relevant main findings and discussion of the natural periods and the response behavior from the decay tests.

6.1.5.1 Natural Periods

The natural periods for the numerical LPT model are established to be closer to the experimental model than it was for the Morison's formulation. The natural period for linear heave motions, from Table 6.1, is the same as for the experimental model, which is a clear indication that the LPT formulation of diffraction/radiation problem is a good formulation of the experimental results.

The problem arises when nonlinear motions in heave are exposed during decay tests, where the water plane area changes as a function of the displacement. The natural period increases for both the experimental and numerical LPT model, which is odd especially for the numerical LPT model. In reality, the natural periods should be the same, since the numerical LPT model for linear and nonlinear motions are based on linear theory. To the author's great surprise do the nonlinear natural period for the numerical LPT model correspond with the nonlinear natural period for the experimental model. This is either a pure coincidence or that 3DFloat could include parameters that the author does not know of.

The natural periods in pitch is harder to establish, and the problematic is important to address. It is assumed that the oscillation is valid for linear motions in pitch direction for experimental results, while the nonlinear motions are incorrect. This observation leads to the fact that the linear natural periods are analyzable, while the natural periods in pitch for nonlinear motions are not analyzable. In other words may the natural period for nonlinear motions be *more* correct for the numerical LPT model than for the experimental model, since the linear numerical pitch natural period corresponds okay with the linear experimental pitch natural period. It is from Table 6.1 observed that there exist a distinct offset between the experimental and numerical natural period in pitch. This difference may be vital for the numerical responses if, for instance, the spectral peak period is higher than the numerical pitch natural period. This would naturally lead to that the numerical LPT model under predicts the motions.

The natural periods in heave w/ heave plates increases for linear and nonlinear motions. Thus is the nonlinear natural period more aligned with the experimental test than the linear natural period. The reason for this may be that the numerical LPT model does not calculate the correct added mass or other effects in 3DFloat which is unknown for the author.

It is, in general, observed that the natural periods is close to the 1^{st} order wave period interval. The pitch (linear and nonlinear) and the heave w/ heave plates (linear and nonlinear) natural periods are all within the 1^{st} order wave period interval, meaning that large motions will occur for the structure.

6.1.5.2 Response Behavior of Decay Test

The linear heave motions represent the experimental motions well, meaning that LPT formulates the experimental motions well. The nonlinear heave motions have a larger offset than the linear case. The experimental nonlinear heave natural period is observed to increase during tank tests, due to the sudden change of water plane area and the higher order viscous effects from when the torus exits and enters the sea water. This exit-enter phenomenon leads to a vibrational behavior, expressed as an increase of added mass, which increases the natural period. It is also observed for the experimental model, that the first rapid damping generates waves. These waves go outwards as well as inwards within the torus. The inward waves interact with the *other side* of the torus, and that is why the heave displacement and acceleration picks up later in the time series for linear and nonlinear heave motions. The numerical LPT model represents this occurrence well.

The response behavior for linear pitch motions is observed to have a distinct offset, compared to experimental motions. There exist a phase shift, even though the peaks for both models have the same amplitude. Nonlinear pitch motions are observed to have a large difference, due to the bad measurements from experimental tests.

The response behavior in heave w/ heave plates shows good correspondence for nonlinear heave motions. This correspondence may be a random coincidence or because of inadequate representation of heave plates. It can also be connected to insufficient knowledge regarding the nonlinear theory of heave plates or bad post-processing of the experimental results.

The determination of hydrodynamic coefficients, in terms of linear and quadratic damping, has only been applied in the heave direction without heave plates for getting a better correspondence with experimental results. Thus, it is seen from Figure 6.1 and Figure 6.2, that the numerical motion still has an offset. The linear and quadratic damping is not sufficient, seen by the large damping during the first oscillation in Figure 6.1 and the excited motions at 45 s in Figure 6.2. This means that there must exist higher order additional damping effects, which are either frequency dependent or connected to other motions than velocity.

The response behavior of pitch motions and heave motions w/ heave plates does account for the constant linear heave damping coefficients, but not damping effects for its oscillation. The reason for not obtaining linear and quadratic damping coefficients for pitch and heave w/ heave plates is due to the measurement system for experimental pitch motions, and the many uncertainties of the scaling of the model sized heave plates. Usage of values which corresponded with the decay test in Secs. 6.1.2 - 6.1.3 would only be a random guess, and could under predict loads in future analysis.

6.2 Regular Wave Test

The regular wave test comparison compares the nacelle heave acceleration, column base heave position and the wave elevation for numerical and experimental motions.

6.2.1 Case 1 - Linear

Case 1 is a very linear sea state, where the wave height is small compared to the wave length. This case is excited by incident regular waves with a wave height of 1.05 m and wave period of 14.5 s. Heave acceleration, heave displacement and the sea elevation are shown in Figure 6.7.

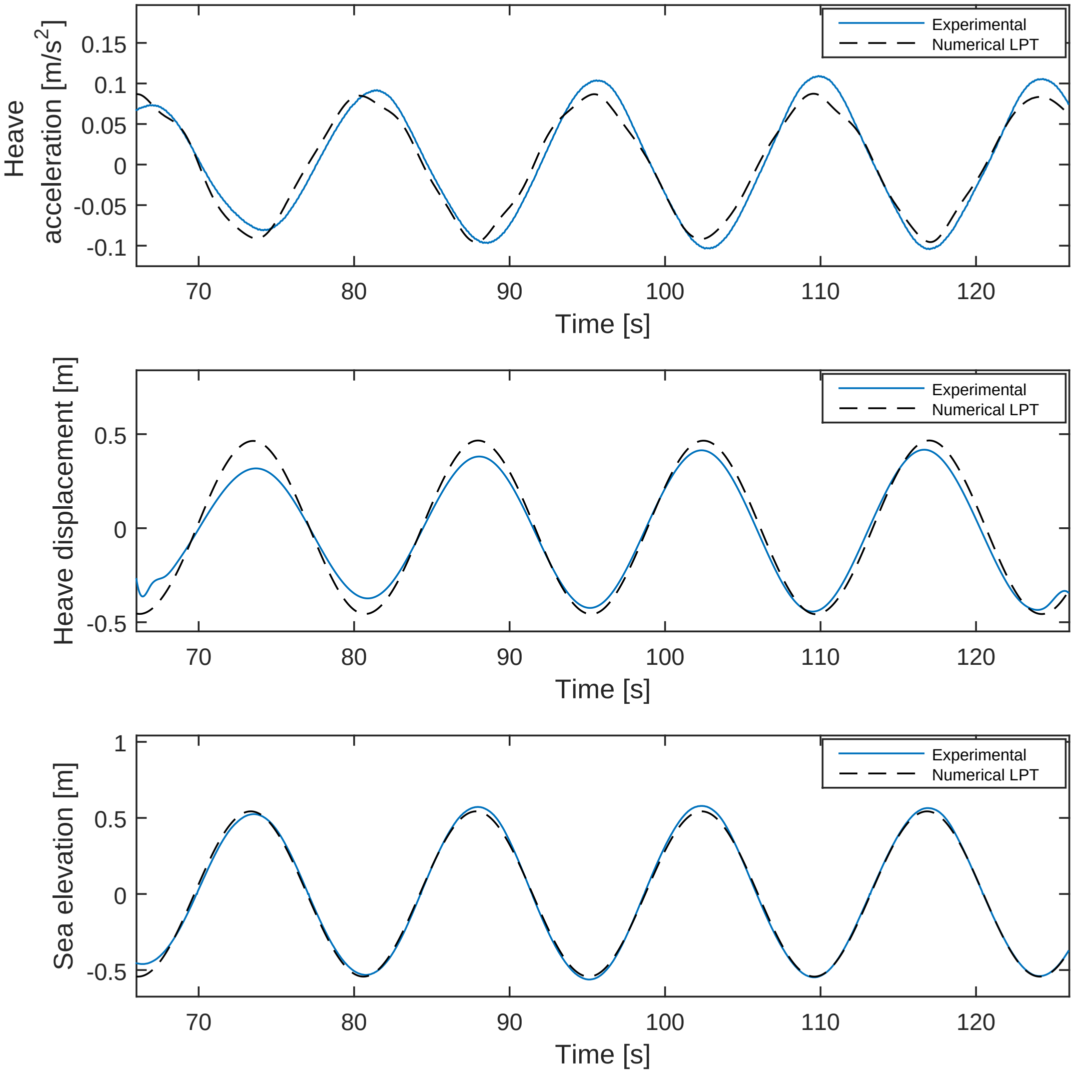

Figure 6.7: Comparison of case 1

It is observed that the numerical heave acceleration, heave displacement and sea surface corresponds well with the experiments, for the last three oscillation. The first oscillation is to some degree inconsistent, possibly due to the ramping of the waves during experimental test.

6.2.2 Case 2 - Semi Linear

A wave height of 1.8 m and wave period of 10 s excites the wave in case 2. Heave acceleration, heave position and the sea surface are shown in Figure 6.8, for the numerical and experimental test.

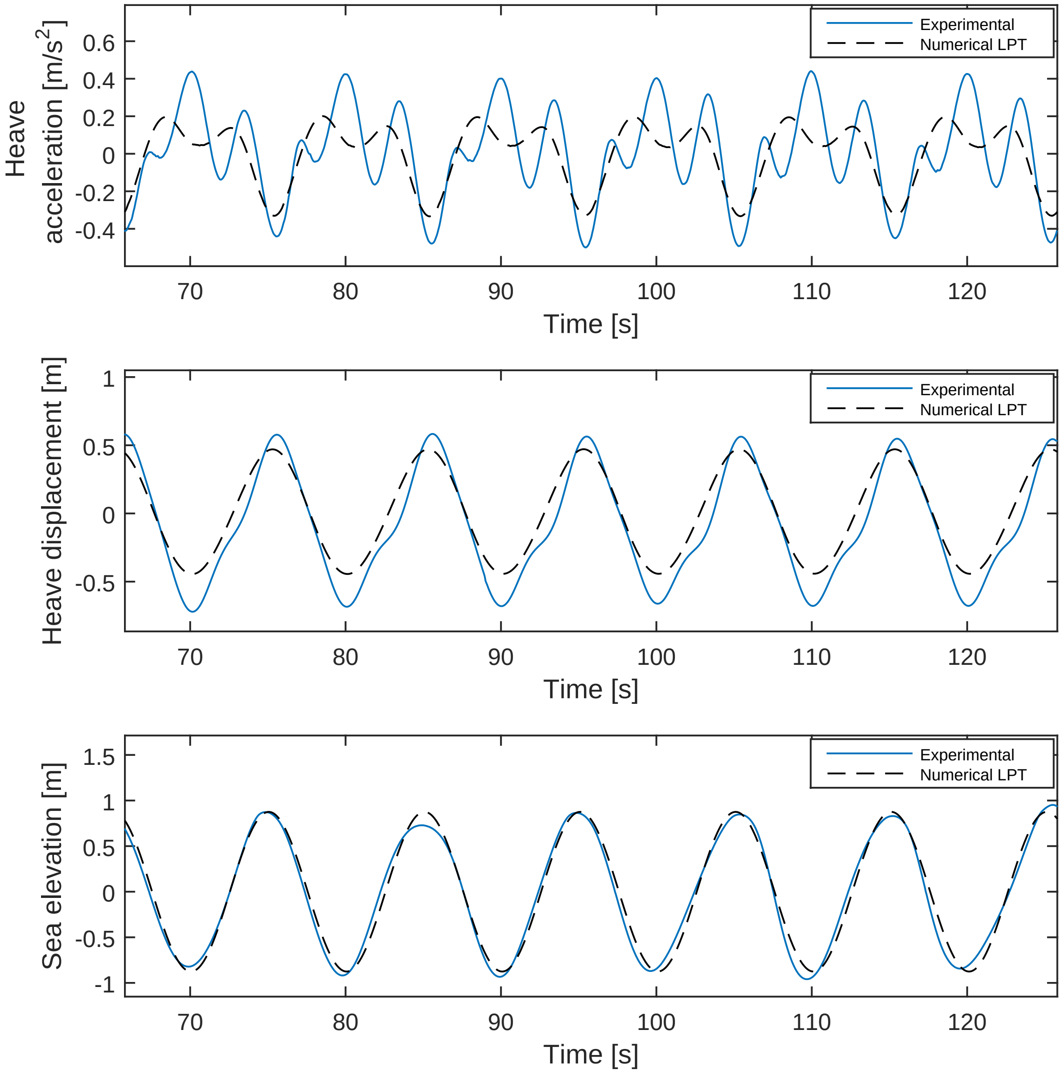

Figure 6.8: Comparison of case 2

A closer look between 95.5s and 106 s has been illustrated in Figure 6.9.

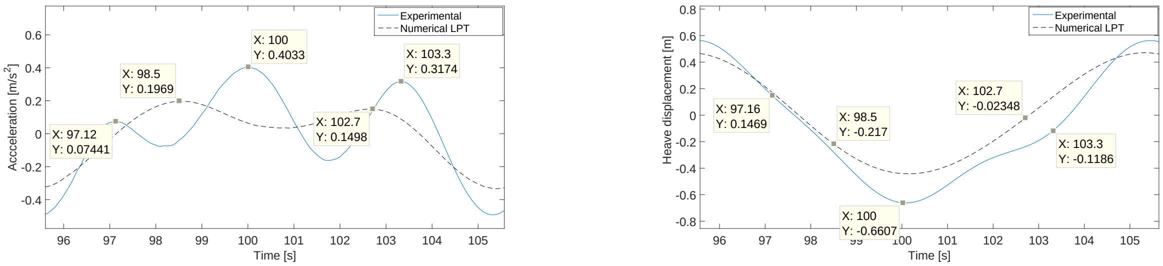

(a) Acceleration

(b) Heave displacement

Figure 6.9: Detailed comparison case 2

The numerical heave acceleration is observed to have a distinct offset for maximums and minimums from the experimental heave acceleration, even though the behavior is good. The maximums of heave accelerations have three peaks for the experimental (97.12s,100s and 103s), from Figure 6.9a. These are also plotted in the heave elevation in Figure 6.9b. The experimental heave acceleration peaks are at concave bottoms for the heave elevation. These are show-able for the reader at the second and third peak (100s,103.3s), while the reader must look closely to see the concave behavior for the first peak of heave displacement (97.12s).

It is observed that the peak oscillations at the maximum for heave acceleration (on the interval 95.6-106s) oscillate two times for the numerical LPT model. That is a clear difference from the experimental model that oscillates three times.

It is also observed that the experimental motions are larger than the numerical heave displacement. The experimental heave displacement does also oscillate about a negative value, seen by the heave minimums being greater than the heave maximums.

6.2.3 Case 3 - Nonlinear

The structure is exposed to a nonlinear incident regular wave in case 3. The incident regular wave has a wave period of 9 s and a wave height of 6.5 s. Heave acceleration, heave displacement, and sea elevation are shown in Figure 6.10, for experimental and numerical results.

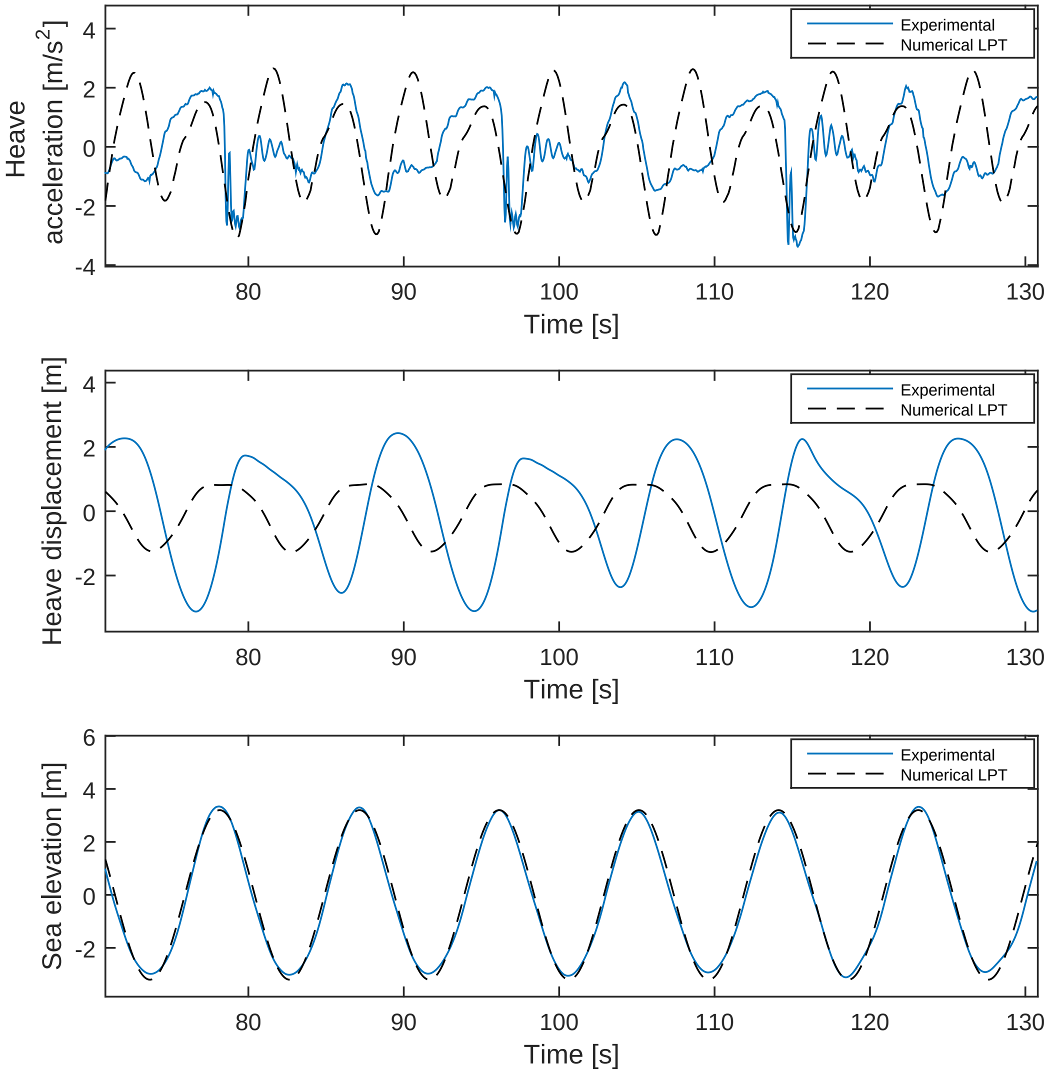

Figure 6.10: Comparison of case 3

A closer look between 97s and 116 s has been illustrated in Figure 6.11.

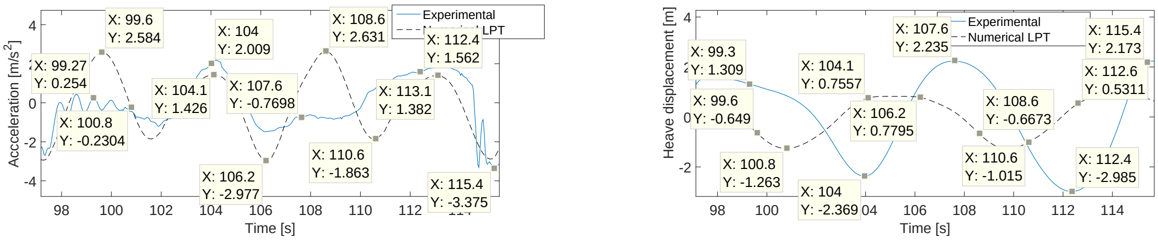

(a) Acceleration

(b) Heave displacement

Figure 6.11: Detailed comparison of case 3

The numerical heave acceleration is observed to have two fully oscillations when the numerical heave acceleration only has one. This is seen between 97s to 106s, where the experimental avoids the fully oscillation at 99 s, and excites vibrations instead. The period between two adjacent peaks for the numerical LPT model is 4.5 s, equal to half the pitch oscillation period.

The experimental heave displacement of the structural response oscillates with double of the incident regular wave period, 18.1 s, gathered directly from the heave acceleration. Another observation is that the experimental heave displacement does not oscillate with the same period during the double regular wave period. It is observed that the *first* heave oscillation oscillates with a period of 9.8 s (107.6s-97.8s), while the *next* oscillation oscillates with a period of 8 s (115.6-107.6). It is also observed that the experimental heave displacement does not oscillate with the same phase as the regular waves. This is seen clearly at time 107.6 s where the experimental heave position is at its maximum, while the sea elevation is at a negative value. It is, therefore, observed that the phase difference is approximately 90 degrees.

The numerical heave displacement is observed to have a maximum at the same position as the sea elevation (105.2 s), i.e. no phase difference between the numerical heave displacement and sea elevation. Thus, it is observed that the heave displacement at the maximum is *longer and flatter* than for the heave minimum. Further, it is noted that during the numerical heave maximum at the *starting point* of the heave max is for a numerical heave acceleration at a peak (104s) and the *ending point* of the heave maximum (106 s) is at a heave acceleration minimum. This observation means that half a heave acceleration cycle occurs while the heave position is held at a maximum. It is also observed that the experimental heave displacement is higher than the predicted heave displacement from numerical calculations.

6.2.4 Case 4 - Nonlinear with Heave Plates

The structure is monitored w/ three heave plates in case 4. The structure interacts with incident regular waves with a wave period of 10 s and a wave height of 6 m. A comparison between experimental and numerical heave acceleration, heave displacement and sea elevation are shown in Figure 6.12.

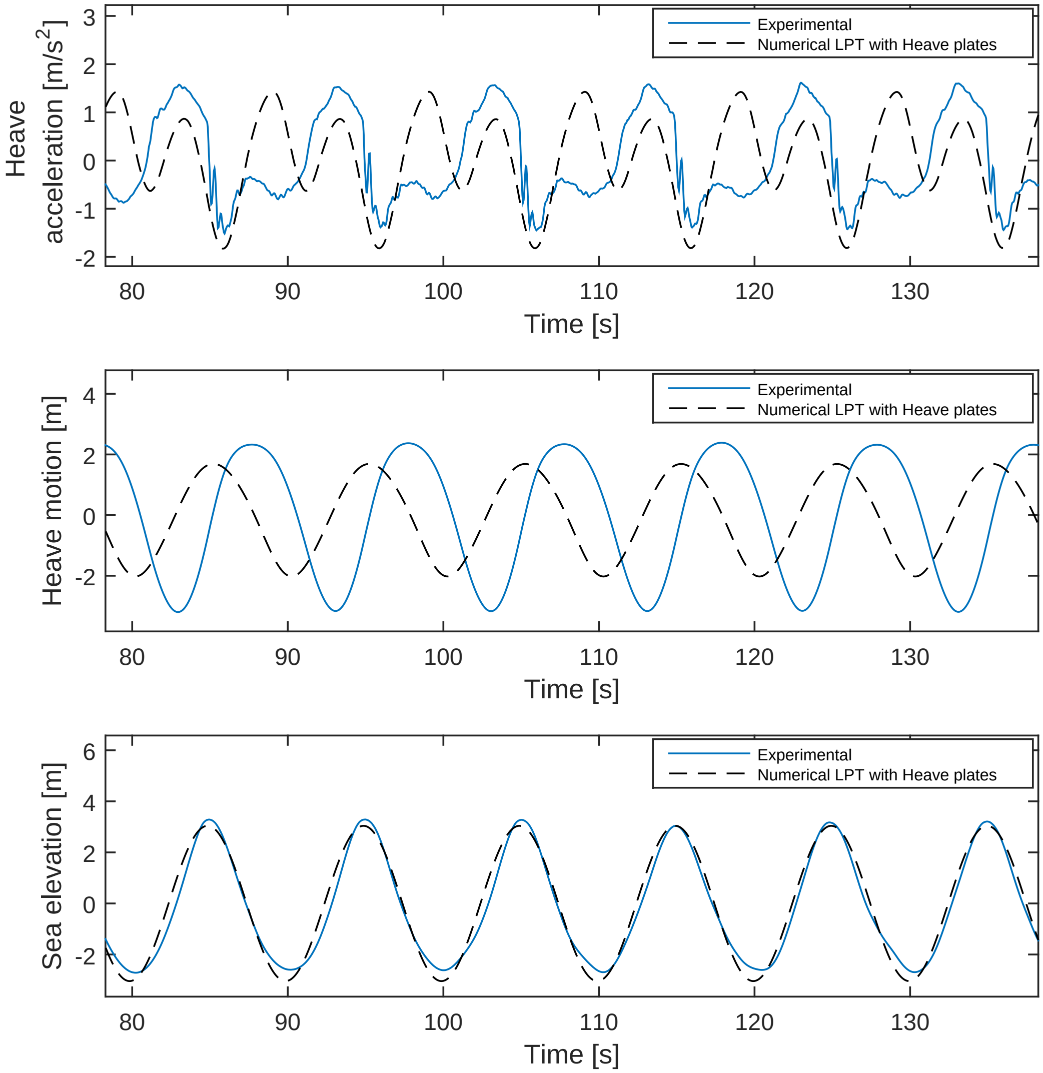

Figure 6.12: Comparison of case 4, with heave plates

A closer look between 94s and 107 s has been illustrated in Figure 6.13.

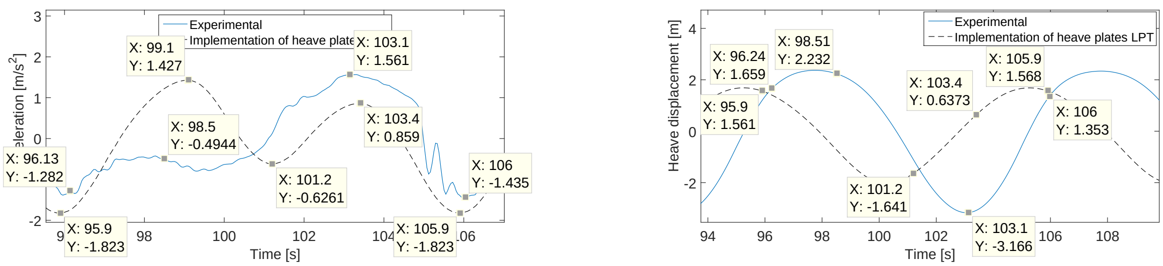

(a) Acceleration

(b) Heave displacement

Figure 6.13: Detailed comparison of case 4, with heave plates

This case observes much of the same observations as described in Section 6.2.3, but some observations are different.

The experimental heave acceleration oscillates with the wave period (10 s), where the behavior of the acceleration repeats with the same behavior (96s-106s,106s-116s and so on). The experimental heave acceleration is not exposed to the vibrational behavior as it was for case 3 without heave plates (98.5 s), but a significant damping occurs. Thus, it is observed for experimental heave acceleration that the oscillation from 96.13s - 103.1s only has one succeeding oscillation due to the large hydrodynamic damping at 98.5 s. This is the time instant where the large vibration occurrence happens in Section 6.2.3.

The numerical heave acceleration oscillates with the same behavior as it did for case 3 without heave plates. It is observed that the numerical heave acceleration has two succeeding oscillation, while the experimental heave acceleration is exposed to significant damping effects (and has therefore only one oscillation).

The numerical and experimental heave displacement does not oscillate in the same phase. The experimental heave displacement is approximately 90 degrees out of phase, as it was in the case in Section 6.2.3. It is observed that the experimental heave displacement oscillates with a more consistent behavior, compared to the experimental heave displacement for the case without heave plates. It is also noted that the experimental heave displacement is higher than the predicted heave displacement from numerical calculations.

6.2.5 Discussion

The acceleration behavior is directly connected to the response behavior of decay tests. This is seen for the linear wave case in Section 6.2.1, where the numerical LPT model represents the experimental motions well. It is safe to say that LPT formulation represents the experimental motions well.

The heave acceleration for the semi-linear case, Section 6.2.2, differs to a larger degree than the linear case. The numerical heave acceleration maximums and minimums, from Figure 6.8, are observed to be lower than the experimental motions, possibly due to higher order damping effects. An increase of the linear and quadratic damping would increase the numerical heave acceleration, but also reduce the heave displacement. This is not optimal, seen from the same figure. The maximums for the heave acceleration have further respectively two and three peaks for the numerical LPT and experimental model. It is clear that the linear formulation does not capture all effects, due to this missing peak oscillation. The peak oscillations at the maximum for heave acceleration (on the interval 95.6-106s, from Figure 6.9a) is most likely due to the pitch oscillation period, occurring during regular wave oscillations. The reader should know that one full pitch oscillation contributes to two heave acceleration oscillations. This observation means that the numerical maximum peaks consist of one peak for the heave displacement and one for the pitch rotation. The same reasoning can be said for the experimental heave acceleration. The reason for the experimental to have three peaks may be due to other effects, for instance motion in one of the other DOFs.

The experimental heave acceleration for the very nonlinear case, Section 6.2.3, is observed to oscillate with twice the incident wave period, while the numerical heave acceleration oscillates with the incident wave period. The experimental heave acceleration observes vibrational loads for twice the incident wave period at time instant 82s, 99s and 117s from Figure 6.10. This vibrational observation is nonlinear and occurs due to the large hydrodynamic loads that occur right before the torus pierces the sea surface. The numerical heave acceleration oscillation does not capture this vibrational effect (seen from the numerical line in Figure 6.10), due to its dependency of linear theory. That is why the numerical heave acceleration oscillates with the incident regular wave period. The numerical heave acceleration observes further two maximum peaks for each incident wave period, due to the pitch motion. The pitch motion contributes to two heave acceleration during one oscillation, described in the previous paragraph. The experimental heave displacement from Figure 6.10 is observed to be larger than the numerical heave displacement, which is due to the heave displacement effect from the submergence of the torus and a non-constant water plane area. The experimental heave displacement is also observed to be shifted 90 degrees to the right in Figure 6.10. This is an odd observation and may be because of a poor measurement system.

The heave acceleration for the nonlinear case w/ heave plates, Section 6.2.4, follows much of the same reasoning as the nonlinear case without heave plates (previous paragraph). The difference from the previous paragraph is that the waves are smaller and that the structure oscillates with a more consistent behavior due to the heave plates. The large vibrational loads are gone, and the structure oscillates with the incident wave period. The experimental heave displacement oscillates still with a phase angle of 90 degrees, compared to numerical heave displacement, which strengthens the statement about a poor measurement system. Thus, the numerical heave displacement amplitude is closer to the experimental heave displacement, meaning that a more consistent behavior (less nonlinear effects) contributes to a better numerical heave representation.

6.3 RAO

A Response Amplitude Operator (RAO) comparison study has been performed to validate the numerical LPT model for heave displacements. An RAO study is a method for determining natural periods and cancellation periods. During such an analysis is the wave height fixed, while the incident regular wave period varies. RAO is often denoted as a transfer function, which gives the response as a percentage of the incident wave height.

To perform an RAO comparison must the experimental test be reliable and correct. This is only partly true since pitch is not analyzable and waves with short periods are not consistent, regarding heave displacement and sea elevation. Nevertheless, an RAO study for heave displacement will be compared, to establish a better understanding of which wave period that is reliable, and if fundamental assumptions are correct. The RAO values are determined by taking the mean (half of the upper and lower peaks) of all peaks of the heave position and divide it by the average of all peaks of the sea elevation.

The measured wave heights during experimental tests are limited, and a complete comparison can not be performed. The comparison has therefore used all available measurements from the experimental database, to capture most of the RAO line. Three RAO comparisons in heave will be presented in the next three section, where the incident regular wave height will be 1, 2 and 3m.

The experimental heave displacement, compared to the sea elevation, for the five regular wave cases from Appendix F.3 are also plotted in the RAO comparison. This is for illustration how linear and nonlinear sea states differs for linear RAO lines. The environmental parameters for the five regular wave cases are shown in Table 6.2.

Table 6.2: Regular wave cases for RAO comparison

Case	**Hs [m]**	**Tp [s]**	**Description**
1	1.05	14.5	Linear
2	2	10	Semi-linear
3	6.5	9	Nonlinear
4	3	10.4	Semi-Linear
5	2.17	9	Semi-Linear

6.3.1 Wave Height 1 m

The numerical unit load for a fixed wave height of 1 m, with varying wave periods, is computed through 3DFloat and compared with cases from the experimental database. These points are plotted together and are illustrated in Figure 6.14.

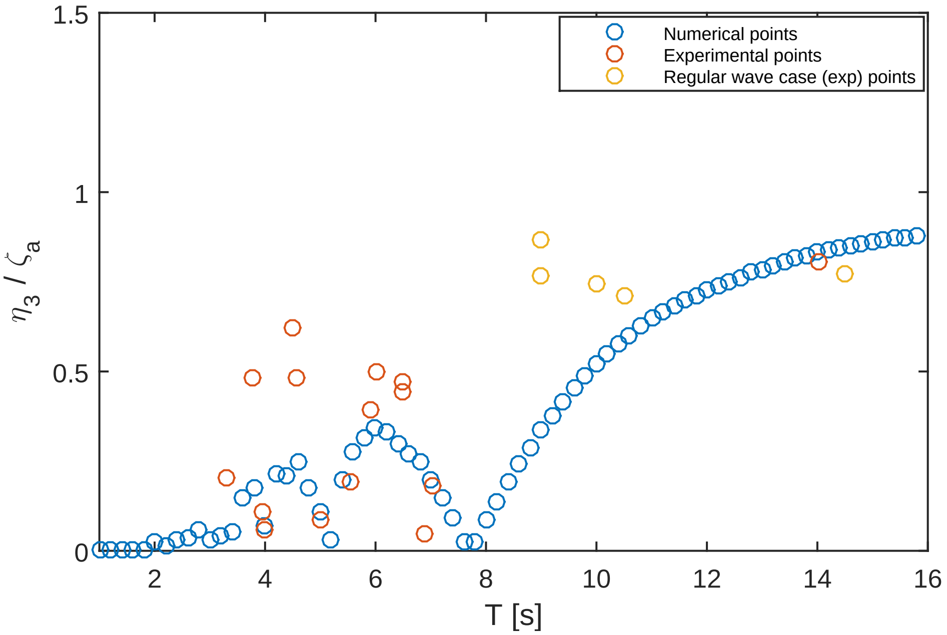

Figure 6.14: RAO for wave height 1 m

Figure 6.14 consists of numerical, experimental and regular wave case (exp) points. These represent the computed numerical points, experimental points from a database and the experimental points from Appendix F.3 respectively. The regular wave case (exp) points differs to a great extent compared to both the numerical and experimental (from the database) points. The point that has a wave period of 14.5 s and wave height of 1.05m corresponds well with the numerical point.

The computed numerical points are more consistent than the experimental points. The numerical points follow a smooth line, and it is easy to see that the cancellation periods are at time instant 4s, 5.2s, and 7.7s. The peaks for the experimental RAO amplitudes are observed at 3.7s and 4.4s, corresponding well with the numerical linear and nonlinear natural period from Table 6.1.

6.3.2 Wave Height 2 m

An RAO comparison between experimental and numerical results for a wave height of 2m is shown in Figure 6.15.

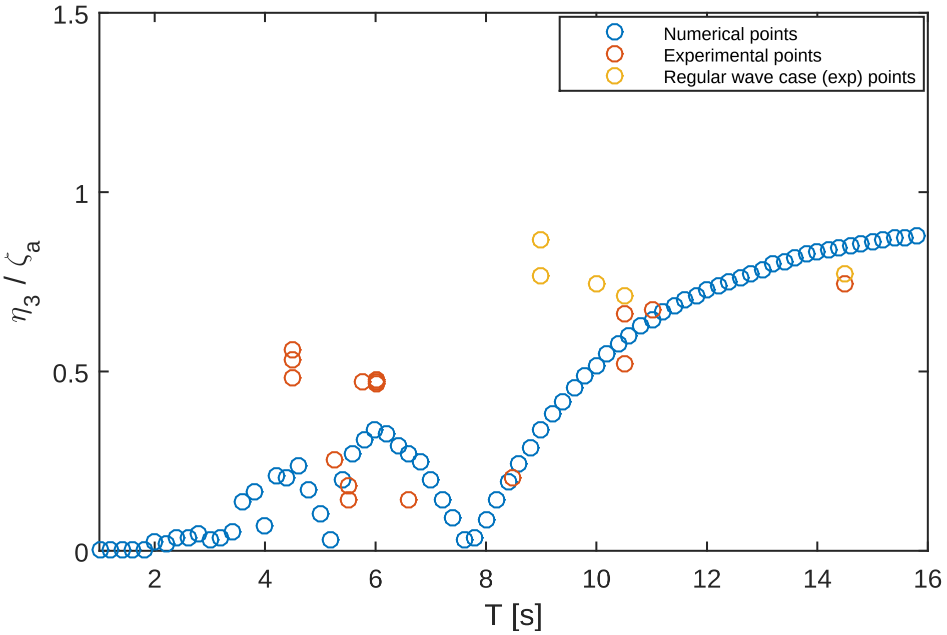

Figure 6.15: RAO for wave height 2 m

It is observed from Figure 6.15 that the numerical unit response points behave in the same manner as it did for 1 m. The underlying problem with analyzing the relationship between incident regular wave height and the heave displacement is the same for this section, as described in Section 6.3.1.

The number of experimental points is less, compared to the 1m RAO case, due to a limited number of experimental tests. Thus, it is observed that there exist more points in the time interval between 8 s and 12 s, which makes a total RAO comparison more complete. The RAO points from the semi-linear case two and four from Table 6.2 are additionally within the same range as the numerical points.

6.3.3 Wave Height 3 m

An RAO comparison between experimental and numerical results for a wave height of 3m is shown in Figure 6.16.

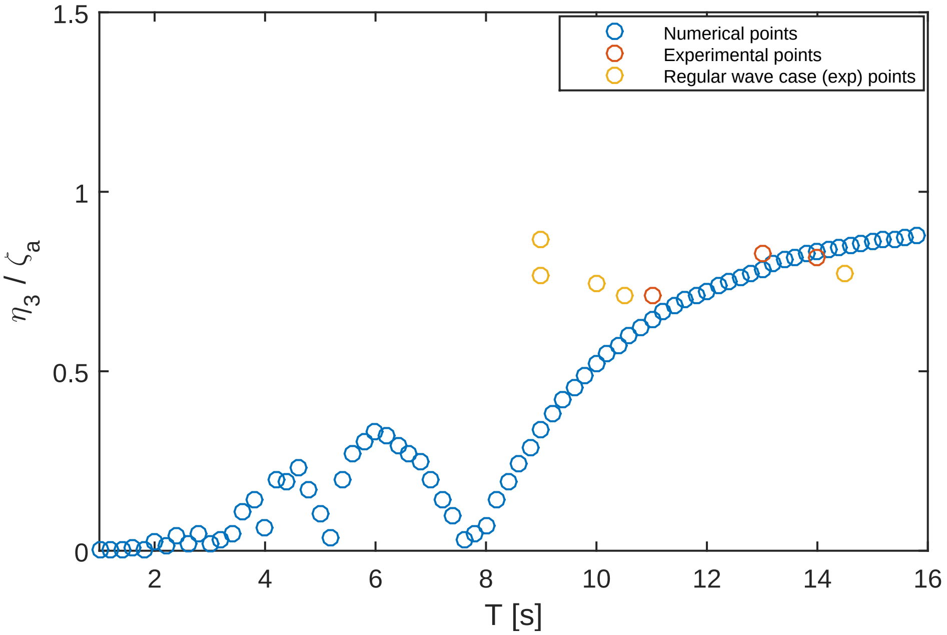

Figure 6.16: RAO for wave height 3 m

The numerical points from Figure 6.16 behaves with the same trend, as it did for the two previous RAO comparisons. This case has only three linear experimental points for comparison, and it is observed by looking at the figure that these points are closely aligned with the numerical points. These three points cover the missing points from previous sections, which completes an RAO comparison more.

6.3.4 Discussion

The discussion of RAO consists of a discussion regarding three regular wave cases from RAO 1m, followed by a general discussion in the end.

6.3.4.1 Three Experimental Regular Wave Cases

The RAO comparisons have a distinct offset when experimental and numerical motions are compared. Subjects that must be addressed are why the amplitudes are different and why are some of the points inconsistent. The sea elevation and heave displacement from experimental test must be studied in detail, to do so. Three experimental wave cases from Section 6.3.1 with the associated heave displacement are shown in Figure 6.17. The selected experimental points are 3.28 s, 4.49s and 6.87s.

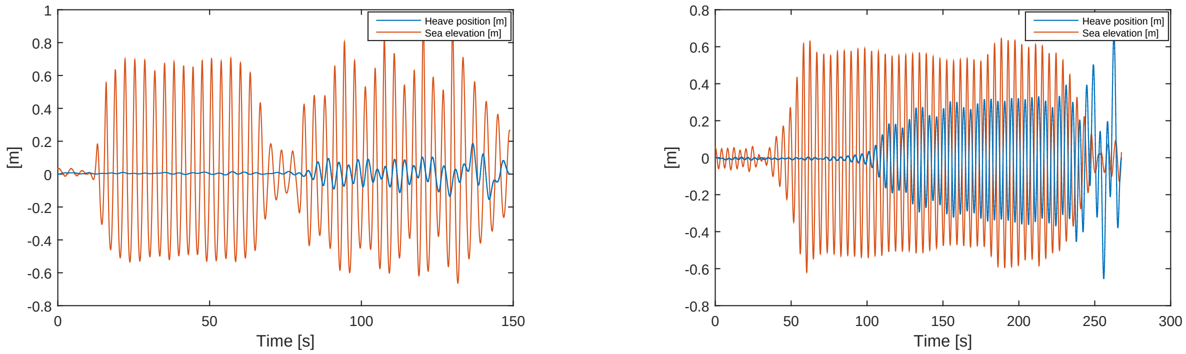

(a) H = 1.03m , T = 3.28s

(b) H = 1.09m , T = 4.49

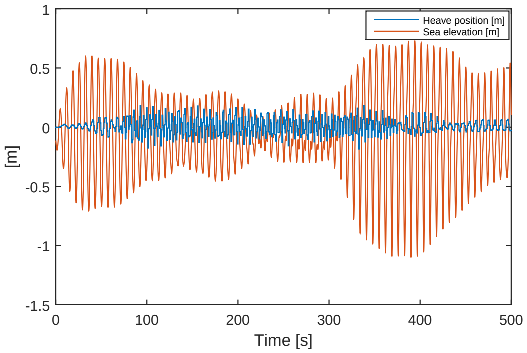

(c) H = 1m , T = 6.87s

Figure 6.17: Three different experimental wave cases for heave displacement and sea elevation, picked out from the RAO

Case (a) from Figure 6.17a illustrates an incident wave with a short period interacting with the structure. The same figure shows that the incident regular wave behaves irregularly, where the first part oscillates regular and the latter part irregular. It is, also, observed that the incident wave is measured at a time before it interacts with the structure.

Case (b) from Figure 6.17b represents better an interaction of incident regular waves. It is, therefore, more analyzable, than the previous case. Thus, it is observed that the time difference between the sea elevation and heave position occurs, as it did for case (a). The heave displacement is observed to increase for each oscillation cycle. That indicates the structure is oscillating in its heave natural period. If a longer analyze window would be selected could the RAO response been larger. This is seen by the high motions at the end of the figure.

Case (c) from Figure 6.17c illustrates an incident regular wave with a wave period of 6.87 s. It is observed that the waves are irregular compared to case (b), where the wave height varies from 0.7 m to 1.5 m. It is, therefore, difficult to create an accurate RAO point. It is observed that the waves are longer, fewer waves die out and the comparison time window is longer. It is, also, observed that the time distance between the sea elevation and heave elevation is small, due to a higher wave period.

6.3.4.2 RAO

The RAO comparisons for the three wave heights are difficult to analyze, seen by the previous section. This is valid especially for shorter waves, where the waves die out and diffract from the structure. Medium long waves excite the structure and the associated radiated waves influences also the flow field and the analyzing window for regular waves. Another effect for the RAO comparison is the misalignment between the sea elevation and the heave displacement, affecting the window of analyzation. This is due to the wave probe being monitored a distance in front of the structure. However, the RAO will be investigated for three wave heights to verify fundamental assumptions.

The RAO comparison consists of numerical and experimental points within linear theory, and regular wave case points within semi- and nonlinear theory. The numerical points follow a smooth behavior for all wave heights, due to its dependency on linear theory. The numerical RAO points are at peaks of 3.7s, 4.5s, and 6s, and cancellation periods at 4s, 5.5s, and 7.8s. The two first peaks correspond well with the linear and heave nonlinear natural period, found from Table 6.1. The period 6s does also have an amplitude, but this is not seen as the natural period. The experimental points verify the natural periods to some degree. The experimental peaks are observed at 3.7s and 4.5s from Figure 6.14, meaning that the numerical LPT model represents natural periods good for linear motions. The experimental points from the regular wave comparison differ to a larger degree for the nonlinear waves, seen in Figure 6.14. There exist a larger offset for nonlinear waves which states that the numerical LPT model has problems for nonlinear motions.

The RAO for a wave height of 2 m (Section 6.3.2) observes peaks for numerical and experimental points at 4.5 s. It is in other words safe to say that one of the natural periods is for this period. The numerical points behave in the same manner as presented in the previous paragraph. Thus, it is now observed that there exist experimental points between 8 s and 12 s, completing the total RAO. The experimental points correspond good with the numerical points, meaning that the LPT represents long wave period well for linear motions. The experimental points from regular wave test comparison are observed to have a distinct offset due to the nonlinear behavior.

The experimental points for RAO of 3m (Section 6.3.3) have only three points, due to limited time in the tank. These waves are close to the numerical RAO line, which is a clear indication that the numerical LPT model for long waves is correct.

6.4 Discussion Summary

The numerical LPT model represents the experimental model in a better way than the numerical Morison's model. The numerical LPT model includes the frequency dependent added mass and damping for linear motions, that captures a lot of the effects which the numerical Morison's model misses.

The numerical LPT model represents the experimental model for linear motions, due to a good correspondence for the natural period. The linear heave natural period is the same for the experimental and numerical LPT model, meaning that LPT is correctly implemented. The formulation regarding pitch motion is rather uncertain and unknown to the author. It is hard to establish natural periods and hydrodynamic coefficients for pitch motions, due to inadequate measurement methods during experimental tests. The pitch motion from the experimental test is based on many uncertainties, and a combination of hydrodynamic coefficients would be totally random. This is also valid for the case w/ heave plates. The influence of the pitch motion is unknown in this comparison chapter but is assumed to be little on natural periods and general behavior. Thus, it will affect the next two chapters, since these uses bending moments for its calculation which are directly influenced by the pitch motions.

The heave displacement has a distinct offset for semi- and nonlinear motions, according to this chapter. This is most likely due to the excitation loads that are dependent on linear theory for this numerical LPT model. The theoretical influence of the torus going in and out of the water plane and an non-constant water plane area is difficult to address, but it is seen from visualization and comparison that the impact is great. The heave motions are observed to oscillate irregularly for regular waves, which the numerical LPT model does not capture. Higher order damping effects occur for the experimental model that linear and quadratic damping does not capture sufficiently.

Chapter 7

Fatigue Limit State Design Check

Long-term analysis is now possible to perform, due to a calibrated and developed numerical LPT model that corresponds with experimental results in heave. The Fatigue Limit State(FLS) design check is the first long-term analysis that will be performed.

This chapter defines the FLS reference frame, establishes the 20-year cumulative fatigue damage for the structure w/ and without heave plates and investigates the fatigue damage further. The structure is excited for different environmental conditions within one sea state in a further analysis, to check whether the structure is wave- or wind-dominated. The wave, wind, and wave heading angle are the environmental conditions that vary.

7.1 Definition of Reference Frame

The fatigue calculations in this Master's thesis are calculated for the tower base. A well-described definition of the reference frame is needed to remove any doubts regarding the calculation. A thorough verification by using a simplification method for establishing moments at tower base can be seen in Appendix G.

The orientations of moments and the cross section of the tower base can be seen in Figure 2.14, gathered directly from Section 2.8.1. The local coordinate system for the tower base is established from an Unsteady BEM modeling, where the local tower base coordinate system is defined in Table 7.1.

Table 7.1: Definition of local in global coordinate system

Global/Local	**X - Axis**	**Y-Axis**	**Z-Axis**
X - Axis	0	0	1
Y - Axis	0	1	0
Z - Axis	-1	0	0

The emphasized and bolded axis determines respectively the local and global coordinate system, from Table 7.1. It is observed that the coordinate system is changed compared to the Cartesian coordinate system for incident regular waves and global motions, in 3DFloat. A further investigation for verifying the moments are seen in Figure 7.1.

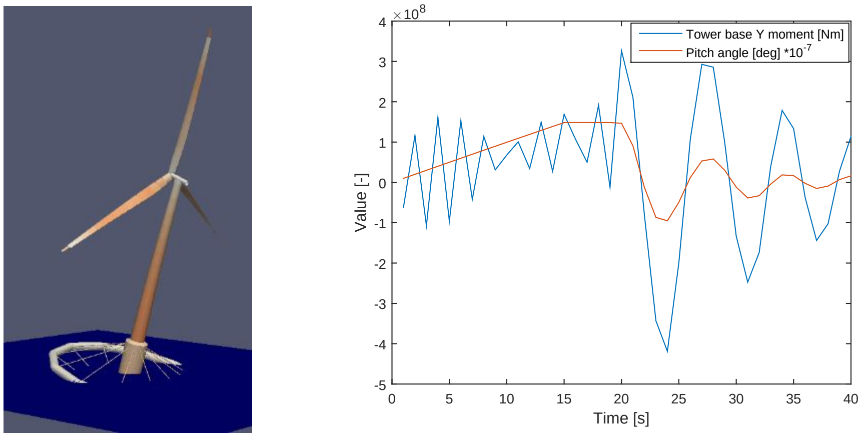

(a) Pitch Decay (b) Tower base Y moment / Pitch angle

Figure 7.1: Verification of tower base moments

The floating wind turbine has a pitch angle of 15 degrees before it decays in Figure 7.1. It is observed that the bending moment oscillates with the same phase as the tower base moment, i.e positive bending moment about the y-axis gives tension and compression in respectively Fore and Aft. This is valid for a wave and wind heading angle of 0 degrees.

7.2 20-Year Cumulative Fatigue Damage

The 20-year cumulative fatigue damage is described in Section 4.7.2 and Section 2.8.1. The FLS study requires that the cumulative damage shall be computed for the operational lifetime. The operational lifetime is not specified for this Master's thesis. According to DNV-RP-J101 will the FLS study be performed according to the 20-year cumulative fatigue damage.

A hypothetical site [19] is selected for fatigue analysis and comparison. It is assumed that 95 % of the environmental conditions can be expressed by 15 sea states, where the last 5 % of the environmental conditions does not contribute to fatigue damage. A cumulative fatigue damage for t_y years can be calculated by using Equation 7.1,

$$D_{t_y} = t_y \cdot 365 \cdot 24 \cdot \sum_{k=1}^{15} D_k \cdot P(k) \tag{7.1}$$

where D_k is the cumulative damage within sea state k, and P(k) is the probability for the associated sea state.

7.2.1 Without Heave Plates

The environmental conditions for the 15 sea states, simulation damage, the probability of the sea state, annual and 20-year fatigue damage are presented in Table 7.2, for the structure without heave plates.

Table 7.2: Fatigue damage at tower base, for structure without heave plates

Case	**Hs**	**Tp**	**U**	$\mathbf{D1_{1hour}}$	$\mathbf{D2_{1hour}}$	$\mathbf{D_{1hour}}$	**Prob**	$\mathbf{D_{1y}}$	$\mathbf{D_{20y}}$
1	1.25	4	4	2.4e-06	2.83e-06	2.62e-06	0.168	0.00385	0.077
2	1.25	6	6	5.24e-05	5.24e-05	5.24e-05	0.227	0.104	2.08
3	1.25	8	4	0.000174	0.000173	0.000174	0.132	0.201	4.01
4	2.75	6	6	0.000412	0.000424	0.000418	0.178	0.651	13
5	2.75	8	8	0.00155	0.00157	0.00156	0.098	1.34	26.8
6	2.75	10	8	0.00138	0.00146	0.00142	0.025	0.31	6.21
7	2.75	12	10	0.000873	0.000841	0.000857	0.021	0.158	3.15
8	3.75	6	12	0.000879	0.000875	0.000877	0.005	0.0384	0.768
9	3.75	8	10	0.00489	0.00454	0.00471	0.057	2.35	47.1
10	3.75	10	12	0.00381	0.00361	0.00371	0.015	0.488	9.75
11	3.75	12	14	0.00246	0.00248	0.00247	0.002	0.0433	0.866
12	5.25	8	18	0.0165	0.0179	0.0172	0.009	1.36	27.1
13	5.25	10	18	0.0108	0.0115	0.0111	0.01	0.975	19.5
14	5.25	12	18	0.00688	0.00734	0.00711	0.002	0.125	2.49
15	6.75	12	20	0.0135	0.0132	0.0134	0.004	0.468	9.37

There has been done two 1 hour simulations, $D1_{1hour}$ and $D2_{1hour}$, for each sea state, in order to establish a mean damage, D_{1hour}. The damage and the associated Prob (Probability) are the necessary parameters to establish the 1 year and 20-year cumulative damage for one sea state. This is seen through Equation 7.1, by only summing up over one sea state. The 15 different damages and probabilities are input to the same equation, for establishing the 1 year and 20-year cumulative damage. These cumulative damages are shown in the following list:

$$1_{\text{year}_{\text{fatigue}}} = 8.6$$

$$20_{\text{years}_{\text{fatigue}}} = 172.4$$

It is observed that the damage at tower base violates the fatigue requirement from DNV-RP-C203, for respectively 1 and 20 years.

7.2.2 With Heave Plates

The same procedure is used to establish cumulative damages for 1 hour, 1 year and 20 years within each of the 15 sea states, as presented in the previous section. These damages are shown in Table 7.3, for the structure w/ heave plates.

Table 7.3: Fatigue damage at toer base, for structure with heave plates

Case	**Hs**	**Tp**	**U**	$\mathbf{D1_{1hour}}$	$\mathbf{D2_{1hour}}$	$\mathbf{D_{1hour}}$	**Prob**	$\mathbf{D_{1y}}$	$\mathbf{D_{20y}}$
1	1.25	4	4	3.382e-07	3.083e-07	3.233e-07	0.168	0.0004757	0.009514
2	1.25	6	6	2.704e-05	2.619e-05	2.661e-05	0.227	0.05292	1.058
3	1.25	8	4	0.0001567	0.0001668	0.0001618	0.132	0.1871	3.741
4	2.75	6	6	0.0001804	0.0001865	0.0001835	0.178	0.2861	5.721
5	2.75	8	8	0.00127	0.001356	0.001313	0.098	1.127	22.55
6	2.75	10	8	0.001328	0.001257	0.001292	0.025	0.283	5.661
7	2.75	12	10	0.0008772	0.0008672	0.0008722	0.021	0.1604	3.209
8	3.75	6	12	0.0003853	0.0004085	0.0003969	0.005	0.01738	0.3477
9	3.75	8	10	0.003157	0.003388	0.003273	0.057	1.634	32.68
10	3.75	10	12	0.003037	0.002936	0.002986	0.015	0.3924	7.848
11	3.75	12	14	0.002342	0.002387	0.002365	0.002	0.04143	0.8286
12	5.25	8	18	0.01036	0.01035	0.01036	0.009	0.8165	16.33
13	5.25	10	18	0.007999	0.008043	0.008021	0.01	0.7026	14.05
14	5.25	12	18	0.005802	0.005607	0.005704	0.002	0.09994	1.999
15	6.75	12	20	0.009576	0.009878	0.009727	0.004	0.3408	6.817

The cumulative damage from a 1 hour simulation for the structure w/ heave plate, follows the same method as for the case without heave plates. The 15 different mean damages and probabilities are input to Equation 7.1, for establishing the 1 year and 20-year cumulative damage. These cumulative damages are shown in the following list:

$$1_{\mathrm{year}_{\mathrm{fatigue}}} = 6.14$$

$$20_{\mathrm{years}_{\mathrm{fatigue}}} = 122.9$$

It is observed that the damage at tower base violates the fatigue requirement for respectively 1 and 20 years.

7.3 Most Probable Sea State Study

The most probable sea state, from Table 7.2, has been chosen for a detailed analysis, in order to comment the fatigue damage additionally. This sea state has been selected since this sea state has the largest possibility of occurrence. This means that it is not necessary the sea state that contributes to the largest cumulative fatigue damage.

A detailed analysis includes a variation of the environmental condition, in order to see which environmental parameter that contributes the most to the cumulative fatigue damage. This thorough analysis consist of six cases for respectively without and w/ heave plates, seen in Secs 7.3.1 - 7.3.2. The environmental inputs for one of the structural model (w/ or without heave plates) are shown in Table 7.4.

Table 7.4: Sea state parameter for case 2

Case	**Hs [m]**	**Tp [s]**	**U_{90}[m/s]**	**Wave Heading [deg]**
1/4	1.25	6	6	0/90 deg
2/5	0.0001	10	6	0/90 deg
3/6	1.25	6	0	0/90 deg

This table shows that it will be done two analysis for each structural model:

1. Without waves and with wind (Case without waves)
2. With waves and wind (Case Initial)
3. With waves and without wind (Case without wind)

with respectively a wave heading of 0 and 90 degrees. It will it be computed 12 tests, to make everything clear. The wind oscillates direction is hold constant during all analysis in the x direction (0 degrees).

7.3.1 Without Heave Plates

This section will study three cases, as mentioned in the previous section, for respectively a wave heading angle of 0 and 90 degrees without heave plates.

7.3.1.1 Wave Heading 0 Degrees

The stress time series for the three cases: without waves, initial and without wind are shown in Figure 7.2.

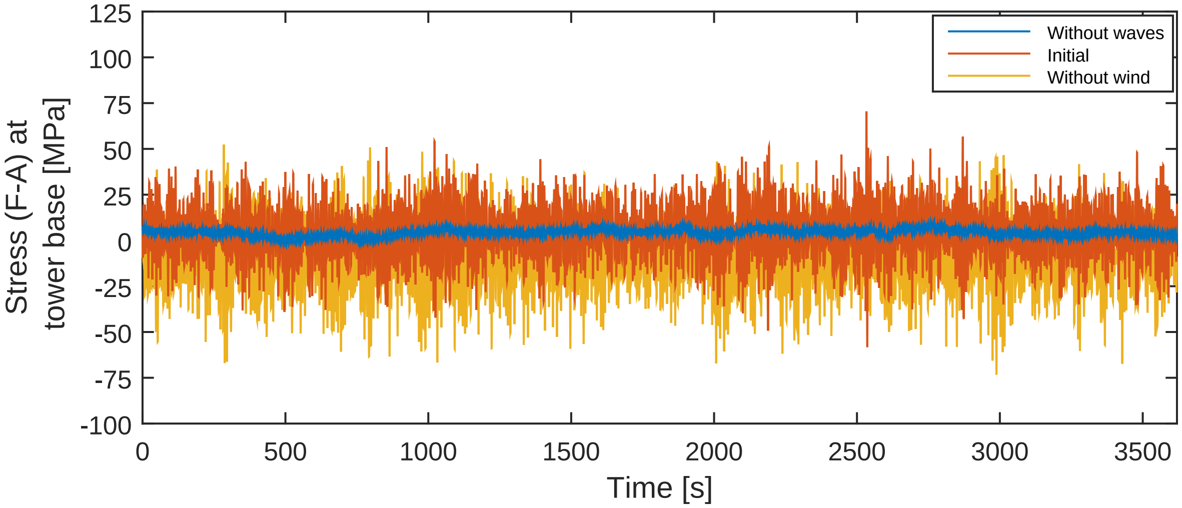

Figure 7.2: 1-hour simulation of stress (F-A) at tower base for wave heading 0 degrees

It is observed that the three different cases give a large variation of stress magnitude. The tower base stress without waves has a mean stress value of 5 Mpa. The initial tower base stress oscillates around the case without waves. The tower base stress without wind oscillates around zero and has a larger amplitude than the previous two cases. It is observed that mean maximum amplitude oscillation for all three cases are between 75 and -75 Mpa.

A further investigation of which frequencies that contributes most to F-A stresses are shown in a spectral analysis in Figure 7.3.

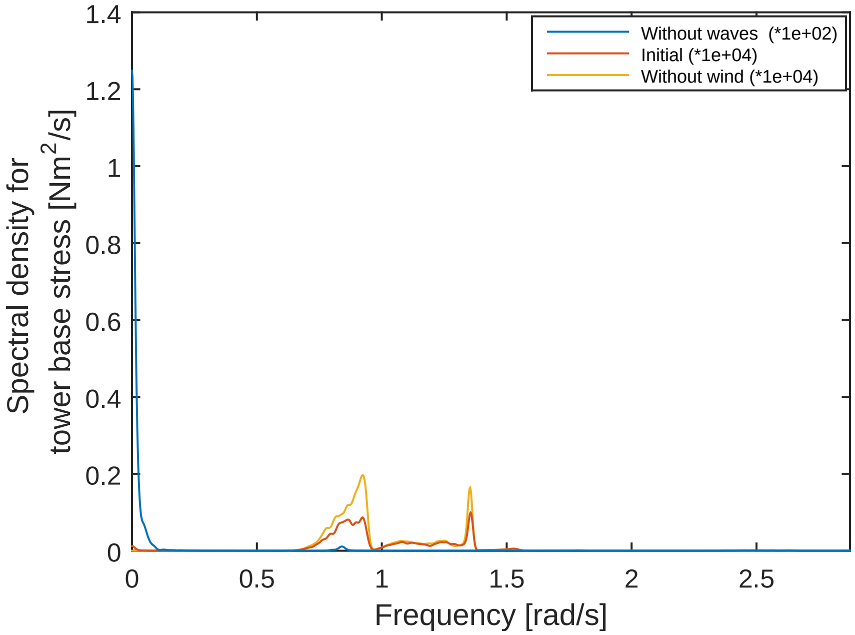

Figure 7.3: Spectral analysis of stress at F-A for wave heading of 0 degrees

It is observed from Figure 7.3 that the initial case has the same graphical behavior as the case without wind. Thus, the magnitude in the spectral analysis are lower for the initial case, following the reasoning for larger stress amplitudes for the case without wind, from the time series in Figure 7.2. It must also be noted that the tower base stress spectral density without waves is 10^{-2} smaller than for the two other cases.

It is of interest to analyze which frequencies the spectral density is excited for. There are observed peaks for all three cases, where some are dominant compared to others. The associated frequencies for each peak are shown in Table 7.5.

Table 7.5: Evaluation of frequencies influencing spectral density

Without waves	
Explanation	*Frequency*
Wind oscillation frequency	0 - 0.08 rad/s (125 s ->)
1 P	0.84 rad/s (7.48 s)
3 P	2.5 rad/s (2.5133s)
Initial [2] & Without wind [3]	
Explanation	*Frequency*
Wind oscillation frequency [2]	0 - 0.08 rad/s (125 s ->)
Pitch Natural frequency [2 & 3]	0.85 rad/s (7.4 s)
Heave Natural frequency [2 & 3]	1.35 rad/s (4.5s)

The values established in Table 7.5 are established with close investigation, where for instance the 3P frequency is barely visible, seen from Figure 7.3. It should be noted that Table 7.5 only lists the frequencies that are identifiable, even though the spectrum has amplitudes for other frequencies than listed. It is seen from Figure 7.3 and Table 7.5 that the waves dominates, since the magnitude is 10^2 larger than for wind. The wave cases has the majority of its excitation for periods between 6.7s to 8.4 s and for 4.5 s, seen from Figure 7.3.

The cumulative fatigue damage for S-S and F-A for these three cases are presented in table 7.6.

Table 7.6: Fatigue damage during 1 hour simulation with wave heading of 0 degrees

Fatigue 1 hour	**S-S**	**F-A**
Without waves	6.9e-10	2e-10
Initial	3e-9	5.23e-5
Without wind	4.82e-12	1e-4

It is observed from the table that the cumulative fatigue damage is largest for the case without wind. The initial case has half the fatigue damage, while the case without waves has a much lower fatigue damage.

7.3.1.2 Wave Heading 90 Degrees

In an S-S fatigue analysis is a wave heading of 90 degrees utilized. The stress time series for the three cases: without waves, initial and without wind are shown in Figure 7.4.

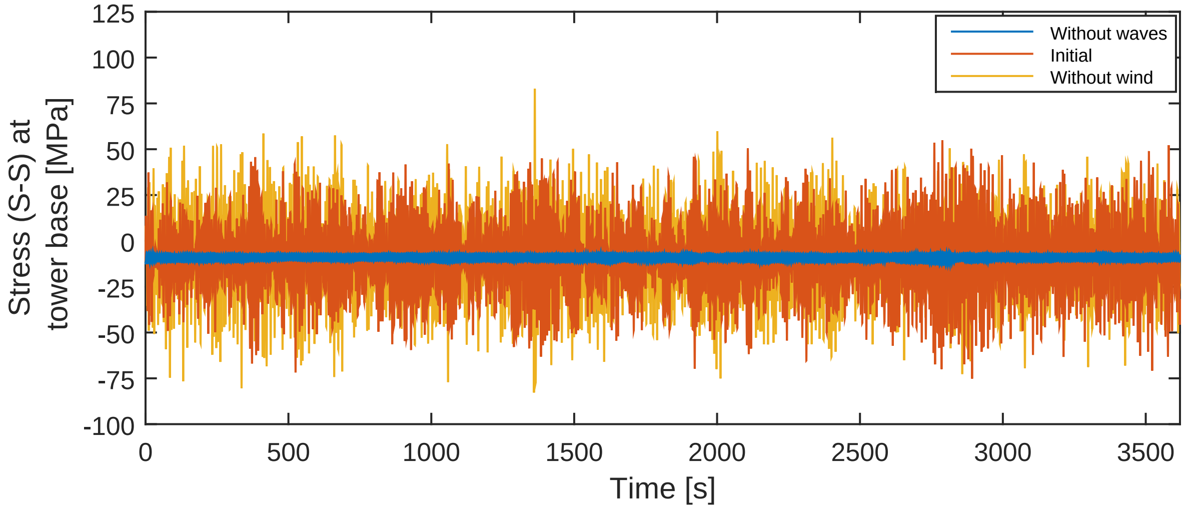

Figure 7.4: 1-hour simulation of stress (S-S) at tower base for wave heading 0 degrees

It is observed from Figure 7.4 that the mean negative stress at tower base for the case without waves has a mean stress of -5 Mpa. The initial case oscillates around this mean value, while the case without wind oscillates around a mean value of 0 Mpa. It is observed that the difference between the two wave cases (with and without wind) does not differ significantly, in contrary to the previous section. It is noted that the maximum amplitude interval of all three cases is between 80 Mpa and -80 Mpa.

A further investigation of which frequencies that contributes most to the S-S stresses are shown in a spectral analysis in Figure 7.5.

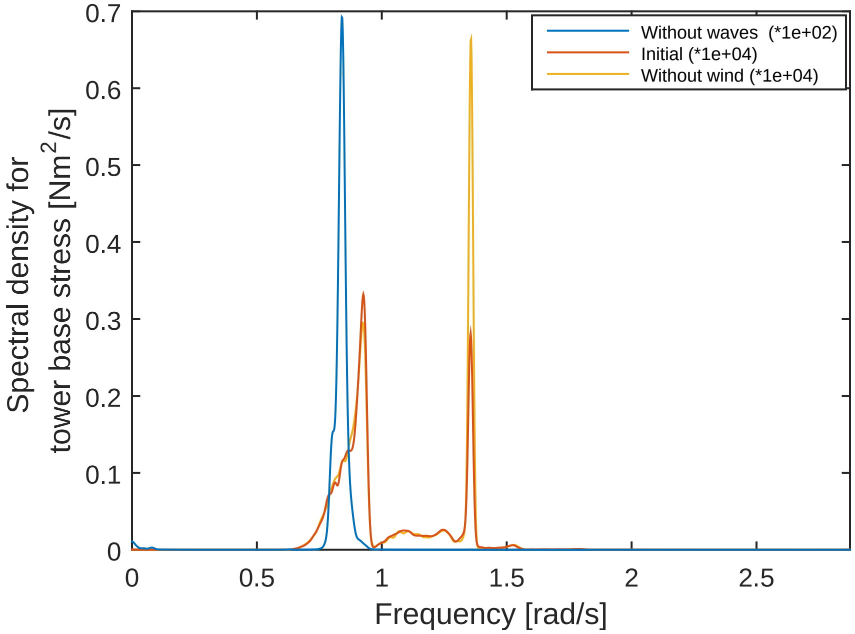

Figure 7.5: Spectral analysis of stress at S-S for wave heading of 90 degrees

The spectral density for the stress of a wave heading of 90 degrees, is located at the same frequencies as it was for wave heading of 0 degrees. This is seen if one were to compare Figure 7.3 and 7.5. An observation seen from this figure is that the spectral density peak for the case without waves has a large amplitude at 0.8 rad/s.

The cumulative fatigue damage for S-S and F-A for these three cases are shown in Table 7.7.

Table 7.7: Fatigue damage during 1 hour simulation with wave heading of 0 degrees

Fatigue 1 hour	**S-S**	**F-A**
Without waves	7e-10	2e-10
Initial	1.37e-4	5.51e-10
Without wind	1.85e-4	1.7e-12

It is observed from this table that the largest cumulative fatigue damage occurs for S-S motions for the case without wind. This cumulative damage is 1.85e-4 during a one-hour simulation.

7.3.2 With Heave Plates

This section will study the same three cases, listed in Table 7.4, for respectively a wave heading angle of 0 and 90 degrees w/ heave plates.

7.3.2.1 Wave Heading 0 Degrees

The stress time series for the three cases: without waves, initial and without wind are shown in Figure 7.6.

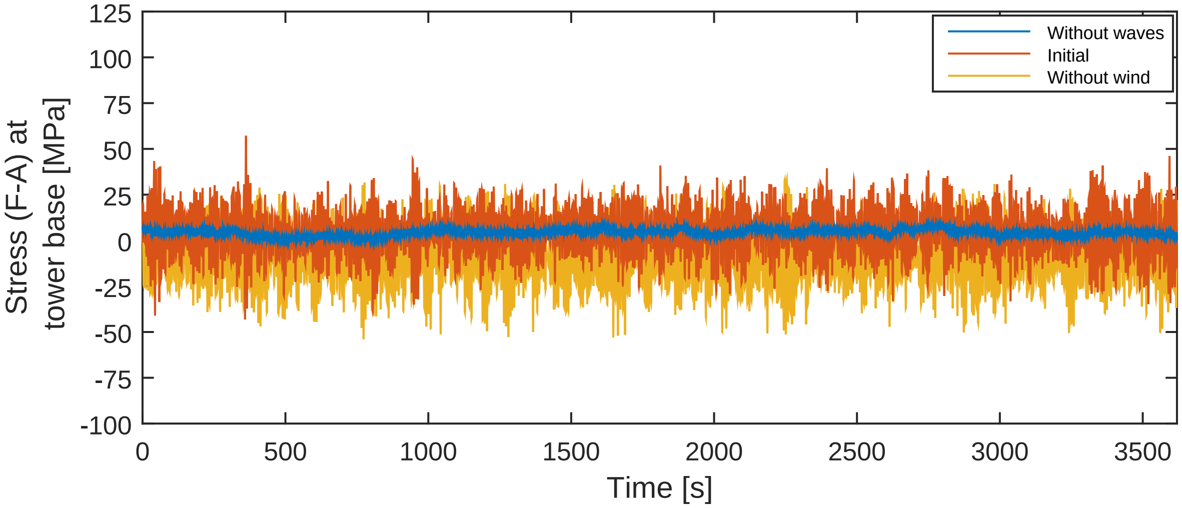

Figure 7.6: 1-hour simulation of stress (F-A) at tower base for wave heading 0 degrees, with heave plates

It is observed From Figure 7.6 that the mean negative stress value for the case without waves is approximately 5 Mpa. The initial case oscillates around this mean value, while the case without case oscillates around zero. It is observed that the maximum oscillations for all three cases are between 50 Mpa and -50 Mpa.

A further investigation of which frequencies that contributes most to the F-A stresses is shown in a spectral analysis in Figure 7.7.

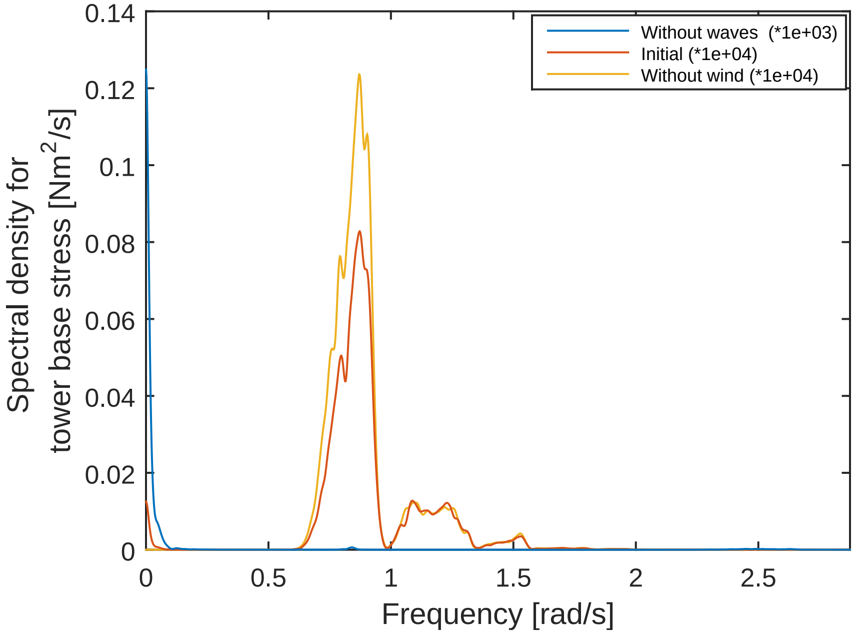

Figure 7.7: Spectral analysis of stress at F-A for wave heading of 0 degrees, with heave plates

It is observed that the greatest magnitude of the stresses is within the interval between 0.7 to 0.9 rad/s. It is observed that the spectral density is approximately twice as high for the case without wind as the initial case for tower base stress.

The associated frequencies for each peak in Figure 7.7 are shown in Table 7.8.

Table 7.8: Evaluation of frequencies influencing spectral density, with heave plates

Without Waves	
Explanation	*Frequency*
Wind oscillation frequency 1 P 3 P	0 - 0.08 rad/s (125 s ->) 0.84 rad/s (7.48 s) 2.5 rad/s (2.5133s)
Initial [2] & Without Wind [3]	
Explanation	*Frequency*
Wind oscillation frequency[2] Natural pitch frequency[2 & 3]	0 - 0.08 rad/s (125 s ->) 0.88 rad/s (7.5 s)

Table 7.8 shows the identifiable frequencies from Figure 7.7. The same figure has several peaks for the initial and without wind case between 1 rad/s and 1.5 rad/s, but it is difficult to say whether these excited frequencies are at the associated structural natural periods.

The cumulative fatigue damage for these three cases are shown in Table 7.9.

Table 7.9: Fatigue damage during 1 hour simulation with wave heading of 0 degrees, with heave plates

Fatigue 1 hour	**S-S**	**F-A**
Without waves	2e-10	6.25e-10
Initial	5.2e-10	2.7e-05
Without wind	9.2e-12	4.3e-05

It is observed that the largest damage occurs for the case without wind and is calculated to be 4.3e-5 for the F-A representation.

7.3.2.2 Wave Heading 90 Degrees

The stress time series for the three cases: without waves, initial and without wind are shown in Figure 7.8.

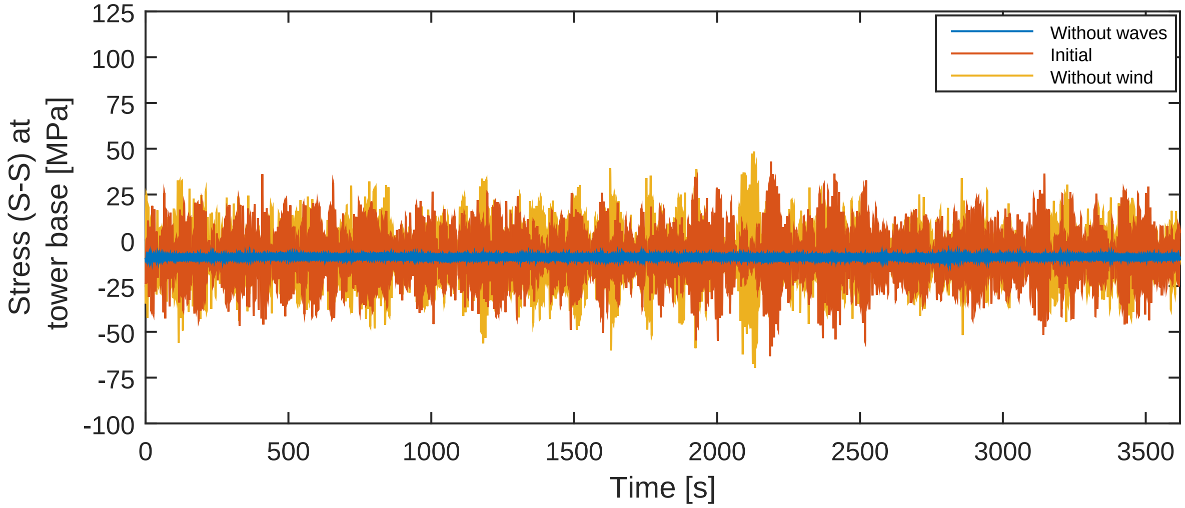

Figure 7.8: 1-hour simulation of stress (S-S) at tower base for wave heading 90 degrees, with heave plates

It is observed that the case without waves does not contribute much to the S-S stress, with a mean value of -5 Mpa. The stresses for the two wave cases are approximately the same. The average amplitude interval of all three cases is between 50 Mpa and -50 Mpa.

A further investigation of which frequencies that contributes most to the F-A stresses are shown in a spectral analysis in Figure 7.9.

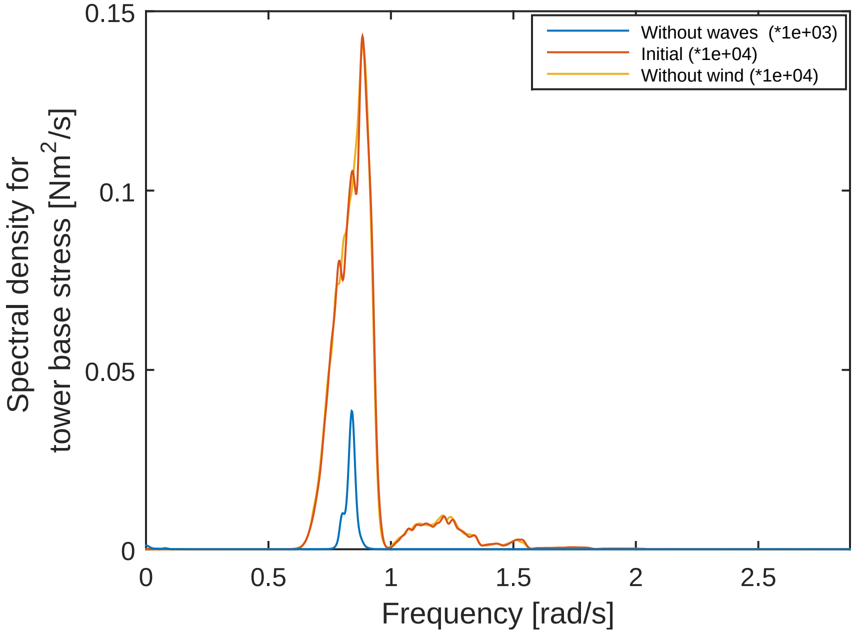

Figure 7.9: Spectral analysis of stress at S-S for wave heading of 90 degrees, with heave plates

It is observed that there is a large peak at 0.84 rad/s for the case without waves, arising from vibrational loads to the S-S stresses at the tower base. All cases are excited for the same frequencies as presented in Table 7.8.

The cumulative fatigue damage for these three cases are shown in Table 7.10.

Table 7.10: Fatigue damage during 1 hour simulation with wave heading of 90 degrees, with heave plates

Fatigue 1 hour	**S-S**	**F-A**
Without waves	2e-10	6.3e-10
Initial	4.53e-05	1.83e-07
Without wind	4.59e-05	2.05e-07

It is observed from Table 7.10 that the two latter cases contribute to the largest cumulative S-S fatigue damages. The damages for the initial case and the case without wind are respectively 4.53e-5 and 4.59e-5.

7.4 Comparison

This section will show an orderly overview of the 20-year cumulative fatigue damage and the detailed fatigue damage. The detailed fatigue damage consists of the spectrum comparison and 1-hour fatigue damage for the relevant orientation. The relevant orientations are FA and SS for respectively a wave heading of 0 and 90 degrees.

7.4.1 Annual and 20-Year Fatigue Damage

The annual and 20- year cumulative fatigue damage, based on a 1 hour simulation, are shown in Table 7.11.

Table 7.11: Comparison of annual and 20 year cumulative fatigue damage

	Without heave plates	**With heave plates**
Damage 1 year	8.6	6.14
Damage 20 year	172.4	122.9

It is observed that the cumulative fatigue damages violates with the requirement criteria, described in Section 7.2. The annual and 20-year cumulative fatigue damage reduces with approximately 28.5 % w/ heave plates attached.

7.4.2 Spectrum

The frequencies of excitation in the most probable sea state and the associated peak magnitude from the spectral analysis are compared for without and w/ heave plates in Table 7.12, with a wave heading of 0 degrees.

Table 7.12: Comparison of spectral peaks and associated periods with wave heading of 0 degrees

	Without heave plates		**With heave plates**	
Without waves	*Per.[s]*	*Amp.* $[Nm^2/s]$	*Per.[s]*	*Amp.* $[Nm^2/s]$
Wind frequency	125 ->	1.25e2	125s ->	1.25e2
1 P	7.48	1.1	7.48	1.1
3P	2.5	0.08	2.5	0.08
Initial				
Wind frequency	125 ->	1.25e2	125s ->	1.25 e2
Pitch Natural Period	7	8.6e2	7.2	7.3e2
Heave Natural period	4.5s	1e3	4.5s	3.4
Without wind				
Pitch Natural Period	7	1.9e+3	7.2	1.2e3
Heave Natural period	4.5	1.6e3	4.5	3.4

It is observed from the table that the periods (Per.) and the associated spectral peak amplitudes (Amp.) for the case without waves are approximately the same w/ and without heave plates.

It is further observed that the difference between with and without heave plates is significant for the two latter cases (*initial* and *without wind*).The spectral peak amplitude that corresponds to the pitch natural period in the two wave cases have reduced respectively 17.3 % and 27.2 % w/ heave plates attached. The most significant reduction for the initial and without wind cases is the amplitude that corresponds to the natural heave period. The amplitudes have decreased with respectively 97.5 % and 98 % for excitation period of 4.5 w/ heave plates attached, for the two latter cases. 68%, 99.5%, 68%, 99% The frequencies of excitation for the most probable sea state and the associated peak magnitude from spectral analysis are compared w/ and without heave plates in Table 7.13, with a wave heading of 90 degrees.

Table 7.13: Comparison of spectral peaks and associated periods with wave heading of 90 degrees

	Without heave plates		**With heave plates**	
Without waves	*Per.[s]*	*Amp.* $[Nm^2/s]$	*Per.[s]*	*Amp.* $[Nm^2/s]$
1 P	7.48	6.9e1	7.48	3.85e1
3P	2.5	3.5e-3	2.5	3e-3
Initial				
Pitch Natural Period	7	3.3e+3	7.2	1.4e3
Heave Natural Period	4.5	6.6e3	4.5	2.6e1
Without wind				
Pitch Natural Period	7	3.3e+3	7.2	1.4e3
Heave Natural Period	4.5	2.8e3	4.5	2.6e1

The three cases with a wave heading of 90 degrees have the same excitation periods, as the cases for a wave heading of 0 degrees. The magnitude of the amplitudes between a wave heading of 0 and 90 degrees have thus a difference. The wind frequency excitation does not affect the S-S stress with a wave heading of 90 degrees, such that this excitation is set to approximately zero.

The wind excitation 1P amplitude is 63 and 35 times larger for the S-S with a wave heading of 90 degrees compared to the stress in F-A direction, for respectively without and w/ heave plates. It is further observed that the excitation at pitch natural period reduces with 68% w/ heave plates for both wave cases, while the heave natural period reduces with 99.5% and 99% w/ heave plates for the initial and without wind cases.

7.4.3 1-Hour Cumulative Fatigue Damage

The 1 hour cumulative fatigue damage with wave heading of 0 and 90 degrees are shown in Table 7.14, w/ and without heave plates.

Table 7.14: Comparison of 1 hour cumulative fatigue damages (F-A) for weave heading of 0 degrees

	Without heave plates	**With heave plates**
0 deg, FA		
Without waves	2e-10	6.25e-10
Initial	5.23e-5	2.7e-5
Without wind	1e-4	4.3e-5
90 deg, SS		
Without waves	7e-10	2e-10
Initial	1.37e-4	4.53e-5
Without wind	1.85e-4	4.59e-5

The largest fatigue damage, for the structure without heave plates, is observed to be 1.85e-4 and 1e-4 for respectively SS and FA direction. These fatigue damages are seen for respectively the case without wind. This means that the cumulative fatigue damage increases with approximately 46 % for a wave heading of 90 degrees for the case without wind.

The largest fatigue damage, for the structure w/ heave plates, is observed to be 4.59e-5 and 4.3e-5 for respectively SS and FA direction. This leads to an increase of only 7 % fatigue damage when the waves are headed with 90 degrees.

It is further observed that the initial case compared to the case without wind is 25 % and 50 % smaller for respectively a wave heading of 0 and 90 degrees.

7.5 Discussion

The 20-year cumulative fatigue damage violates with the DNV requirement of having a 20-year fatigue damage below 1, w/ and without heave plates. The structural cross section has a diameter of 45 mm, and even by doubling the diameter will the cumulative fatigue damage violate the DNV requirement (by neglecting the fact that the structural mass and natural periods changes). However, the heave plates reduce the 20-year cumulative fatigue damage with approximately

28.5%, which is an important effect if one were to design a new structure. The reduction is thus a factor of the surge and pitch acceleration, and with a structure that oscillates less motion, will the cumulative fatigue difference be less. This is clearly seen by for instance wave case 10 in Table 7.2, where the damage difference is only 20% w/ heave plates attached.

The 20-year fatigue damage has not been calculated with a wave heading of 90 degrees, but according to Table 7.14 for the most probable case, increases the damage with approximately 46 % (FA damage to SS damage). This leads to the fact that the 20-year fatigue damage is even higher for a constant wave heading of 90 degrees. The reason for this increase is the pitch damping the rotor contributes to the motions, explained in 2.7.3, which contributes to a 25% smaller damage when the wind and waves are aligned. The probability of having a constant 90 degrees heading during 20-year is very low, but it should be noted that the structure is very vulnerable for different wave heading angles. The structure with heave plates, however, is not so vulnerable to wave heading changes. With a wave heading of 90 degrees increases the SS damage (from FA damage) with only 7%. This will have a great impact on the fatigue damage when the waves get higher, and the sea becomes rougher.

It is seen from all stress time series figures that the stress magnitude oscillates around 0 - 10 Mpa. This is a clear indication that the wind does not contribute significantly to the stress, and that the structure is wave-dominated. The spectral density and the associated excitation frequency, for all wave heading angles w/ and without heave plates, has the majority of its energy for 7.2 s. This period is close to the numerical pitch natural period (Table 6.1), meaning that the stress ranges comes from the oscillation in pitch (or roll).

Another great magnitude of the spectral density is close to 4.5s for the structure without heave plates. This excitation frequency corresponds to the numerical heave natural period, meaning that the stress also comes from heave motions. Another observation is the decrease of spectral magnitude for the heave natural period (4.5s) w/ and without heave plates. The is due to the change of heave natural period when heave plates are attached. It is observed in Table 6.1 that the natural period in heave goes from 4.5s to 10.6s when heave plates are attached. This means that the stress spectrum for this period in this sea condition is low. However, the structure within a sea state with a wave period of 10 s may be vulnerable, regarding fatigue damage, because of the increase of heave natural period.

Another significant effect is the increase of spectral magnitude for 1P frequency for a wave heading of 90 degrees. The 1P period is determined to be approximately the same as the pitch natural period, which means that coupling between these two frequencies may occur.

The cumulative fatigue damage is based on a numerical LPT model without linear and quadratic pitch (and roll) damping for the numerical LPT model. On behalf of experimental data was the pitch damping set to zero, even though linear and quadratic damping should have been included in the rotational direction. This means that the damages in this chapter are conservative.

Chapter 8

Ultimate Limit State Design Check

This chapter will investigate the Ultimate Limit State (ULS) design checks for the improved numerical LPT model, calibrated through comparison study. The checks carried out in this Master's thesis are regarding yield, shell buckling, and column buckling. The loads are established by long-term simulations in 3DFloat, and the checks are therefore dependent on the goodness of the numerical LPT model in 3DFloat.

The numerical LPT model is attached w/ or without heave plates. The ULS design check will, therefore, be carried for both numerical LPT models.

8.1 Definition of Reference Frame

The ULS calculations will be calculated for the tower base. All motions and moments around the tower base are defined with the reference frame shown in Figure 2.14.

The yield conditions follow the same procedure in obtaining the stresses at different angles around the cross section as FLS, while the shell buckling condition is different. The buckling condition for a shell element assumes that the axial force and bending moment are the same for the upper part and lower part, seen from Figure 8.1.

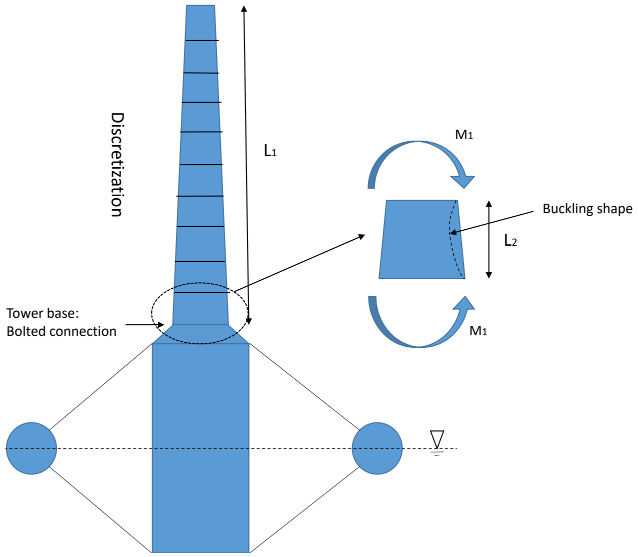

Figure 8.1: Reference frame for ULS calculations

In reality, the tower should be discretized into n number of shell elements, such that the forces on each side are approximately the same. This was not done when performing the time-domain simulation since forces and moments are only established for tower base and tower top. In other words, a buckling length must be chosen, to perform shell buckling checks. Ring stiffeners are introduced for the tower, to separate the column into shells. The buckling length on the shell, L_2 is chosen to be 10 % of the tower length, L_1. This implies values of respectively 7.36 m and 73.6 m, for respectively the buckling length and tower height.

8.2 Checks

The ULS design check is decribed in Section 2.8.2 and 4.7.2. The chosen site for establishing the worst sea state environmental conditions are gathered from a site called Norway 5 [27], which is located in the North Sea outside Trondheim. Information about this sea state is listed in Table 8.1.

Table 8.1: 50- year worst sea state parameters for Norway 5 (Taken from [27])

Water depth	**U_{10}, 50 year**	**H_s, 50 year**	**T_p, mean**
202 m	33.49 m/s	10.96 m	11.06 m

The worst sea states where wind and waves are dominating are shown in Table 8.2.

Table 8.2: Relevant environmental cases for ULS checks (Taken from [27])

Condition	**H_s**	**T_p**	**U [m/s]**
Wave Dominated	15.6	14.5	31.2
Wind Dominated	13.1	13.4	33.6

The environmental conditions from Table 8.2 is the relevant information needed to perform an ULS design check, when it comes to environmental conditions. The reason for establishing two different cases for worst sea states, is due to the unknown knowledge of which environmental parameter that contributes to the largest response. In this Master's thesis will 6 simulations for each dominating case be performed (w/ and without heave plates), with a simulation time of 1 hour. This means that 24 analysis will be performed in total.

8.2.1 Without Heave Plates

The yield and buckling checks for all cases without heave plates are shown in Table 8.3, for cross section orientation θ.

Table 8.3: Checks for eight angles between fore and aft, without heave plates

	Wave Dominated		*Wind Dominated*	
Orientation	**Yield**	**Buckling**	**Yield**	**Buckling**
$\pi/2$	Not ok	Not ok	Not ok	Not ok
$3\pi/8$	Not ok	Not ok	Not ok	Not ok
$\pi/4$	Not ok	Not ok	Not ok	Not ok
$\pi/8$	Not ok	Not ok	Not ok	Not ok
0	Ok	Not ok	Not ok	Not ok
$-\pi/8$	Not ok	Not ok	Not ok	Not ok
$-\pi/4$	Not ok	Not ok	Not ok	Not ok
$-3\pi/8$	Not ok	Not ok	Not ok	Not ok
$-\pi/2$	Not ok	Not ok	Not ok	Not ok

This table shows that yield for $\theta = 0$, i.e where no bending moment occurs, is sufficiently designed for the wave dominated case. The rest of cases and the associated orientations are not designed according to the yield and buckling requirement.

The column buckling improvement shall be assessed if (Section 2.8.2.2):

$$\frac{kL_C}{i_c} \geq 2.5\frac{E}{f_y} \tag{8.1}$$

which is not the case for neither cases. The tower/column should not be improved regarding column buckling requirement.

8.2.2 With Heave Plates

The yield and buckling checks for all cases w/ heave plates are shown in Table 8.3, for cross section orientation θ.

Table 8.4: Checks for eight angles between fore and aft, with heave plates

	Wave Dominated		*Wind Dominated*	
Orientation	**Yield**	**Buckling**	**Yield**	**Buckling**
$\pi/2$	Not ok	Not ok	Not ok	Not ok
$3\pi/8$	Not ok	Not ok	Not ok	Not ok
$\pi/4$	Not ok	Not ok	Not ok	Not ok
$\pi/8$	Not ok	Not ok	Not ok	Not ok
0	Ok	Not ok	Ok	Not ok
$-\pi/8$	Not ok	Not ok	Not ok	Not ok
$-\pi/4$	Not ok	Not ok	Not ok	Not ok
$-3\pi/8$	Not ok	Not ok	Not ok	Not ok
$-\pi/2$	Not ok	Not ok	Not ok	Not ok

This table shows that the yield requirement is now achieved for orientation 0 degrees for wave dominated and wind dominated sea states. The rest of the orientations for respectively yield and buckling requirements are violated.

The column buckling requirement is the same for without heave plates, and must not be improved.

8.3 Discussion

The ULS study, regarding buckling and yield, requires, in general, a structure defined with cross-sectional properties. The cross section should be defined with longitudinal, orthogonal or ring stiffeners or a combination of these three. Only the ring stiffeners are selected for the structural cross section, to perform shell buckling calculations.

The yield loads are established by the mean maximum from the 6 tests for respectively wind and waves, defined in Table 8.2. The loads are multiplied with combinations of loading factors defined in Table 2.3, as a requirement of the recommended practice from DNV. The result is that the yield condition requirement is satisfied for an orientation of only 0 degrees (Side of the cross section) from Figure 2.14, for the structure without heave plates oscillating in the wave dominated sea state. However when the heave plates are attached is the yield condition satisfied for the orientation angle 0 for the wind dominated structure as well. This is due to the reduction of acceleration, e.g. increase of added mass, with heave plates attached. This is a clear indication that the structure is wind-dominant for ULS calculations in terms of yield checks.

The shell buckling condition is computed by assuming that the tower is ring stiffened with a spacing of 7.36 m. This assumption means that the moment at the upper end shall be equal to the moment at the lower end (measured by the author). Further are the design stress loads established by the same combination of load factors of the mean maximum for the 6 test (respectively wind and waves), as mentioned in the previous paragraph. The shell buckling stability requirement are violated for all orientation angles, seen from Table 8.3 and 8.4 respectively. The shell buckling is now computed according to a cross-sectional thickness of 45 mm, and by the program buckling_and_yield.m can it be observed that all orientations are satisfied, if the thickness was 150 mm. Such a thickness will introduce operational problems regarding welding. Luckily can the effective shell thickness be increased by into introducing orthogonal and longitudinal stiffeners, which may satisfy even more orientations for the structure w/ and without heave plates.

The column buckling is relevant for long cylindrical shells. The column buckling should be assessed according to Equation 8.1, but this is not the case for this structure. For large wind turbines that require a longer tower may the column buckling be relevant.

This ULS study does, in fact, not enlighten the reader to a great extent. Information about the structural cross sections are very limited, and the author has had to assume the ring stiffened distance. Longitudinal and orthogonal stiffeners could also have been assumed, but since stiffeners increase the total structural mass and natural periods may be affected (increased), may the associated loads change and not be valid for this structure.

Chapter 9

Conclusions and Recommendation for Future Work

The aim of this Master's thesis was to solve the hydrodynamic problems the FO OFWT foundation faced, and to create a full-scale numerical model applicable for long-term analysis. The numerical LPT model described in this thesis gives an improved representation of the experimental motions, compared to the Morison's formulated numerical model. A long-term analysis can be performed if the user knows the model's limitations.

In Chapter 3, it is shown that experimental measurements are adequate for heave motions and inadequate for nonlinear pitch motions. This influence the judgment of the numerical comparison with experimental results in Chapter 5 and 6.

In Chapter 6, it is shown that the hydrodynamic problems are solved acceptably for linear heave motions. The natural periods, acceleration and displacement are closely aligned with experimental results. The nonlinear heave motions are also sufficient for the numerical model, but a larger deviation occurs than for linear motions. This difference is related to the inadequate setup of the measurement system and nonlinearity. The linear pitch motions are observed to correspond mediocre with experimental results, while the nonlinear motions have a distinct offset compared with the experimental results. The heave motions with heave plates, does also correspond mediocre with experimental results. LPT is concluded to represent the experimental results for heave motions and linear pitch motions, while the nonlinear pitch motions and heave motions with heave plates are unreliable.

Constant damping coefficients are utilized for the heave motions and represents the damping well. The inadequate measurements from the experimental test make a comparison challenging for pitch motions, and any meaningful constant damping coefficients can not be obtained. The constant damping coefficients for heave motions with heave plates is, also, difficult to establish, due to inadequate measurements.

An FLS and ULS design check, where the calculations are mainly from pitch oscillation are violated. The goodness of these checks are dependent on the pitch validity, and it is from the previous paragraphs seen that this is mediocre. Thus, a lot of the heave motions are coupled to the pitch motions during regular and irregular waves, which means that the representation is better. However, the FLS and ULS results represents a conservative solution, but this does not change the fact that the foundation is wave-dominated. The natural period is still within the 1^{st} order wave frequency interval, and to satisfy the requirements, regarding FLS and ULS, a re-design must be performed.

9.1 Recommendations for Future Work

The recommendations for future work consist of problems regarding the design of the floater foundation, improvement of the experimental results, experimental model, software, and numerical modeling. In addition to these problems, a specific site must be selected for future work, in order to take advantage of the environmental condition.

9.1.1 Design of the Floater Foundation

Research in this Master's thesis shows that the structure is wave dominated due to the structural natural periods. The natural periods in heave w/ heave plates and pitch w/ and without heave plates are within the 1^{st} order wave frequency interval, and future work should consider changing these natural periods to be outside the 1^{st} order wave frequency interval. This change can be done either by a re-design of the floater foundation, or adjustments to the existing foundation. One proposed adjustment to the current floater foundation is shown in Figure 9.2.

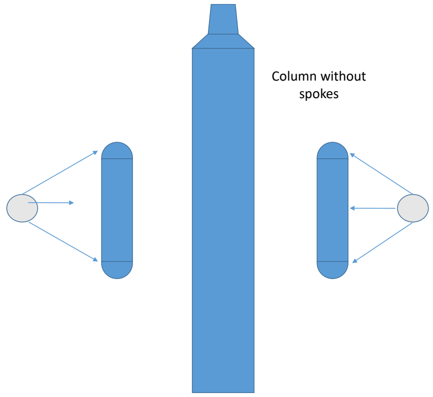

Figure 9.1: Adjustment for future work of the current floater foundation

The foundation in this figure illustrates a reduction of the torus diameter (from the center column), and an increase of the torus height. This foundation will have a smaller water plane area and radii of gyration, which would decrease the hydrostatic stiffness coefficients, and increase the natural periods. The torus height must increase, to withstand the maximum loads and make it more suitable for linear theory.

Nevertheless, a complete design renovation should be carried out in future work, due to the overall violation of design requirements.

9.1.2 Improvement of the Experimental Results and the Experimental Model

The heave motions are the only reliable measurement in our tank test. The pitch direction is also of importance for judgment of the numerical model, due to the dependency of pitch motions in FLS and ULS design study. An improvement of the model test, regarding accelerometers, can be seen in Figure 9.2.

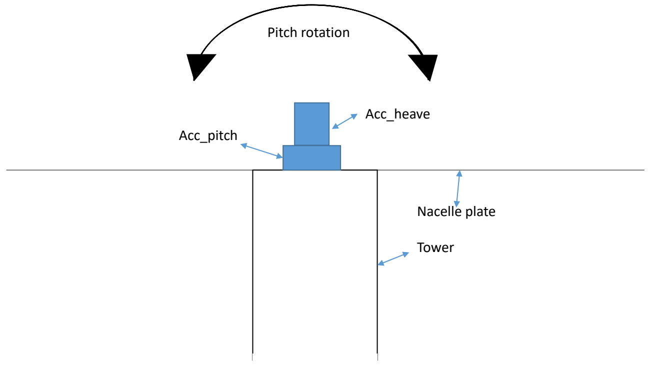

Figure 9.2: Adjustment of experimental accelerometers setup

This figure shows that the pitch acceleration would be more accurate for a rotating structure.

Further improvements, regarding the experimental results, are shown in the following list:

- The heave displacement should in future work be shifted, such that it is aligned with the sea elevation. The incident regular waves for short wave periods dies out before it reaches the structure, such that the number of sea elevation oscillations is not the same as the heave elevation oscillations. It will be important to consider the surge motion of the structure, for the alignment of the waves and structural motions. This could have been done by measuring the forces in the horizontal spring.
- The generated waves during experimental test should have been for a complete RAO analysis, i.e. from a period of 5s to 20s with an acceptable increment period.
- The wave probe should be calibrated in a future investigation. This is for having a correct correspondence between environmental conditions and rigid body motions.
- Another possible future investigation is to include the effect that waves are diffracted from the structure, which influences the new measurements. One way of solving this is to look at the interaction between the structure and the first couple of waves, where the waves have not been diffracted.

- It is also of interest to analyze the waves that interact with the model. Whether they are linear or nonlinear is of importance when post-processing the results.

Improvements, regarding the experimental model, are shown in the following list:

- The experimental model for a new floater foundation should be scaled correctly. This means that the experimental model should use the same material and have correctly scaled weight, COG, and dimensions close to the sea surface.
- The experimental heave plates are rectangular, while circular for the numerical model. The geometry and a verification of a correct scaled heave plate should be carried out in future work.
- It could be interesting to apply a horizontal spring force at the nacelle, to see the pitch damping similar to a constant wind.
- In interest of FOW, it may be relevant to 3D print a smaller model with the correct scaling factor, to expose it for extreme sea, and perform associated analyses.

9.1.3 Software and Numerical Modeling

The software for the LPT formulation assumes linear theory, which is a simplification of the real hydrodynamical problem. In future analysis should the nonlinear theory be implemented, such that higher order damping effect are included. Another approach is to design the structure such that the real hydrodynamical problem can be represented through linear theory.

The LPT can thus be implemented in a better way than the method used in this Master's thesis. The total rigid body can be split into two separate rigid body systems. The reason for separating the body is to account for the fact that the spokes are not infinitely stiff, and that the torus can move independently from the spar (taken into consideration that the spokes are not there). The most interesting way to split the FO structure is pictured in Figure 9.3.

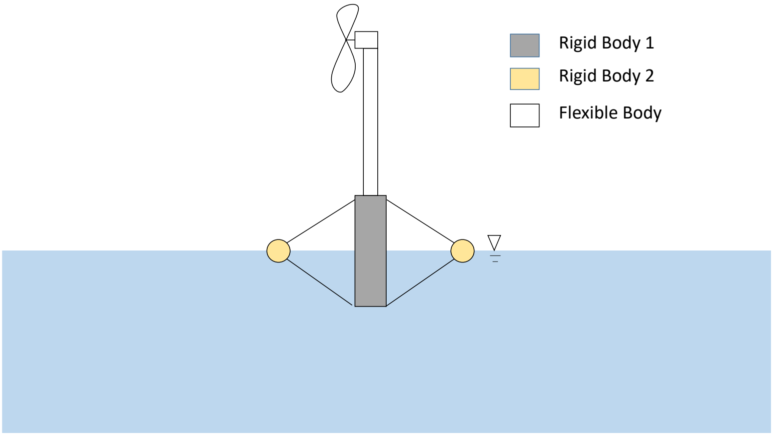

Figure 9.3: Two body system of FO concept

With this setup, it is possible to analyze the internal forces of the spokes and establish a more realistic response of the numerical model.

Another method for representing the hydrodynamic loads is through distributed linear potential loads (distributed LPT). This method applies the integrated forces for each element at the respective node, such that internal loads can be computed for all elements. In other words is the distributed LPT comparable with Morison's formulation, only that frequency dependent hydrodynamic coefficients are included.

Another focus should be to create a numerical model that is consistent with the scaling factor or a numerical model-scale model and the experimental model. In this way would the comparison study only be influenced by the measurement setup within the tank facility.

Other improvements, regarding numerical modeling, are shown in the following list:

- To perform ULS design checks should ring, orthogonal and longitudinal stiffeners be defined across the tower length.
- FLS study should carry out fatigue damage for the heave plates and spokes, in addition to the tower base
- The determination of hydrodynamic coefficient, in terms of linear and quadratic damping, should be applied for pitch and roll direction in future work. The hydrodynamic coefficients should also be established for heave plates in future work.

Appendix A

Acronyms

EU European Union

OECD Organisation for Economic Co-operation and Development

WT Wind Turbine

OWT Offshore Wind Turbine

OFWT Offshore Floating Wind Turbine

O&G Oil & Gas

FO Fred Olsen

IFE Institutt for Energiteknikk

LPT Linear Potential Theory

BEM Blade Element Momentum theory

GDW Generalized Dynamic Wake

EOM Equation of Motion

ULS Ultimate Limit State

FLS Fatigue Limit State

ALS Accidental Limit State

SLS Servicability Limit State

DNV Det Norske Veritas

RAO Response Amplitude Operator

SS Side-to-Side fatigue damage

FA Fore-to-Aft fatigue damage

Appendix B

Design Check for Buckling of Shells

The design requirements for different buckling modes and the associated method for determining the stability of buckling is achieved studied in this chapter.

B.1 Buckling Modes

The buckling modes are shown in Figure B.1.

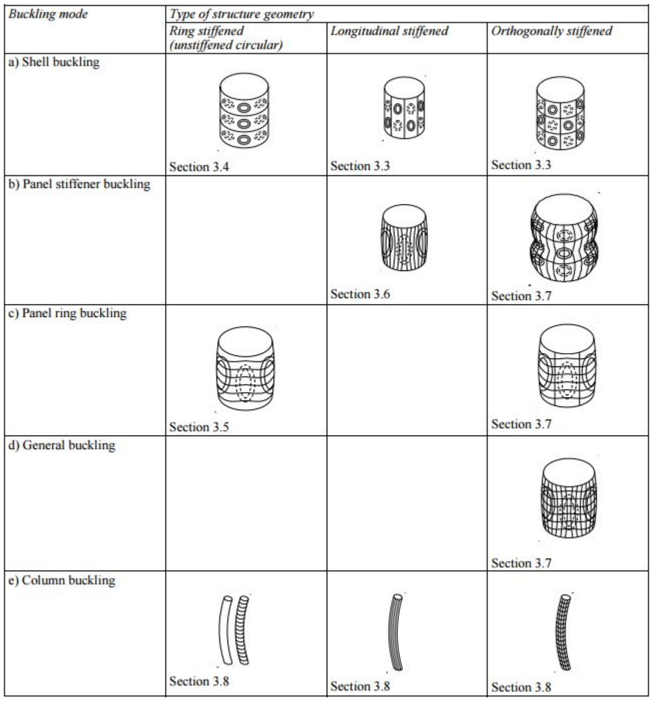

Buckling mode	*Type of structure geometry*		
	Ring stiffened (unstiffened circular)	*Longitudinal stiffened*	*Orthogonally stiffened*
a) Shell buckling	Section 3.4	Section 3.3	Section 3.3
b) Panel stiffener buckling		Section 3.6	Section 3.7
c) Panel ring buckling	Section 3.5		Section 3.7
d) General buckling			Section 3.7
e) Column buckling	Section 3.8	Section 3.8	Section 3.8

Figure B.1: Buckling modes (Taken from [4])

Each buckling mode depends on the structural cross-sectional design of axial, longitudinal and ring stiffeners and each buckling mode. Each buckling mode has its requirement.

B.2 Method for Buckling Design Check

This section will present the method for establishing the buckling requirement, which is the same for all buckling modes. All buckling modes must satisfy the buckling stability requirement represented in Equation B.1[4].

$$\sigma_{j,Sd} \leq f_{ksd} \tag{B.1a}$$

$$f_{ksd} = \frac{F_{ks}}{\gamma_m} \tag{B.1b}$$

The material safety factor depends on the parameter $\bar{\lambda}_s$ which is described in Equation B.2:

$$\gamma_m = 1.15 \qquad \text{for } \bar{\lambda}_s < 0.5$$

$$\gamma_m = 0.85 + 0.6\,\bar{\lambda}_s \qquad \text{for } 0.5 \leq \bar{\lambda}_s \leq 1.0$$

$$\gamma_m = 1.45 \qquad \text{for } \bar{\lambda}_s > 1.0$$

The characterist buckling strength and what it depends on is shown in the following equation:

$$f_{ks} = \frac{f_y}{\sqrt{1+\bar{\lambda}_s^4}} \tag{B.2a}$$

$$\bar{\lambda}_s^2 = \frac{f_y}{\sigma_{j,sd}}\left[\frac{\sigma_{a0,sd}}{f_{Ea}} + \frac{\sigma_{m0,sd}}{f_{Em}} + \frac{\sigma_{h0,sd}}{f_{Eh}} + \frac{\tau_{sd}}{f_{E\tau}}\right] \tag{B.2b}$$

$$\sigma_{j,sd} = \sqrt{(\sigma_{a,sd}+\sigma_{m,sd})^2 - (\sigma_{a,sd}+\sigma_{m,sd})^2\sigma_{hSd} + \sigma_{hSd}{}^2 + 3\tau_{sd}{}^2} \tag{B.2c}$$

where

$\sigma_{a,sd}$ = The axial design stress due to axial forces (tension positive)

$\sigma_{m,sd}$ = The bending design stress due to bending moment (tension positive)

σ_{hSd} = The circumferential design stress due to external pressure (tension positive)

τ_{sd} = The shear and torsion design stress due to shear and torsion forces

f_{Ea} = buckling strength for axial force

f_{Em} = buckling strength for bending moment

f_{Eh} = bucklling strength for circumferential pressure

$f_{E\tau}$ = buckling strength for torsion and shear forces

$\sigma_{a0,sd}$, $\sigma_{m0,sd}$, $\sigma_{h0,sd}$ and τ_{sd} is only the contribution from compression, such that every value less than zero is positive and every value above zero is positive. The buckling strength depends on which buckling mode that shall be investigated. The method going from here depends on of the aim of the buckling study, and which buckling modes that are relevant. These modes are seen in Figure B.1 and the associated methods can be seen in DNV-RP-C202 [4].

Appendix C

Previous Work

This chapter will summarize information and results on behalf of the work done in the Project thesis.

C.1 Experimental and Numerical Dimensions

Table C.1 summarizes the experimental and numerical model dimensions.

Table C.1: Dimensions of experimental and numerical model

Structural dimensions	**Experimental model**	**Full-scale**
Column height	421.5 mm	30 m
Column diameter	90 mm	10 m
Torus large diameter	940 mm	70 m
Torus diameter	50 mm	3.7 m
Structural mass	4.024 kg	2.11E+06 kg
Nacelle mass	0.913 kg	400E+03 kg

C.1.1 Froude Scaling

There exist various scaling methods, and each of them has its pros and cons[42]. In this master thesis has the Froude scaling method only been used for comparisons between numerical and experimental results, seen in Chapter 5 and 6. The Froude Scaling method is also known as geometrical scaling, since the scaling factor is the ratio between a selected full scale dimension and the respective model scale dimension:

$$\lambda = \frac{L_{\text{Full scale}}}{L_{\text{Model Scale}}} \tag{C.1}$$

A more thoroughly investigation of Froude scaling and scaling methods can be found in respectively [32] and [42]. On behalf of previous work is the scaling factor established to be 74, seen from Appendix C.2.

C.2 Establishment of Scaling Factor

Table C.2 validates the scaling factor on behalf of structural dimensions of the experimental and full scale numerical model.

Table C.2: Relationships between model and scale

Establishing scaling factor from known parameters	**Full-scale [m]**	**Model-scale**	**Scale [-]**
Column height	30	421.5 mm	71.18
Column diameter	10	90 mm	111
Torus large diameter	70	940 mm	74.46
Torus cross section diameter	3.7	50 mm	**74**
Structural mass	2.11E+06 kg	4.024 kg	43.1
Nacelle mass	400E+03 kg	0.913 kg	75.94
Model-scale estimated using scaling factor			
Center of gravity	26.15	**353** mm	74
Roll-radius of gyr.	40.72	**550** mm	74

Even though the scaling factor varies from 43.1 to 111 is the scaling factor established to be 74.

C.3 Hydrostatic Stability During Operation and Storm

A check of hydrostatic stability during operation and storm was performed in the project thesis [32] and is shown in Figure C.1. A more detailed investigation can be seen in the same project thesis.

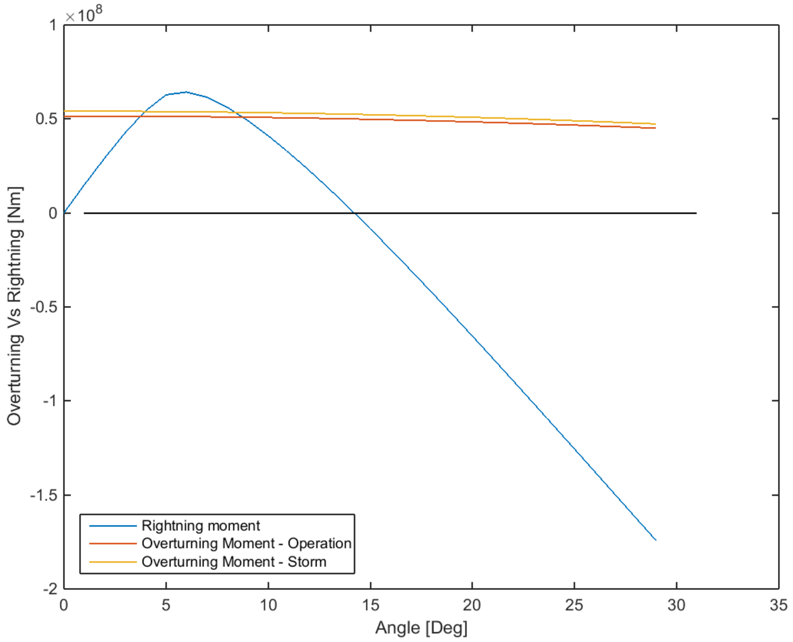

Figure C.1: Overturning moment vs restoring moment for operation and storm

It is concluded that the structure has sufficient stability, according to Figure C.1. A thorough explanation can be seen in [32].

C.4 Tank Facilities and Experimental Setup

The experimental model in the tank, attached with accelerometers and mooring lineas are shown in Figure C.2.

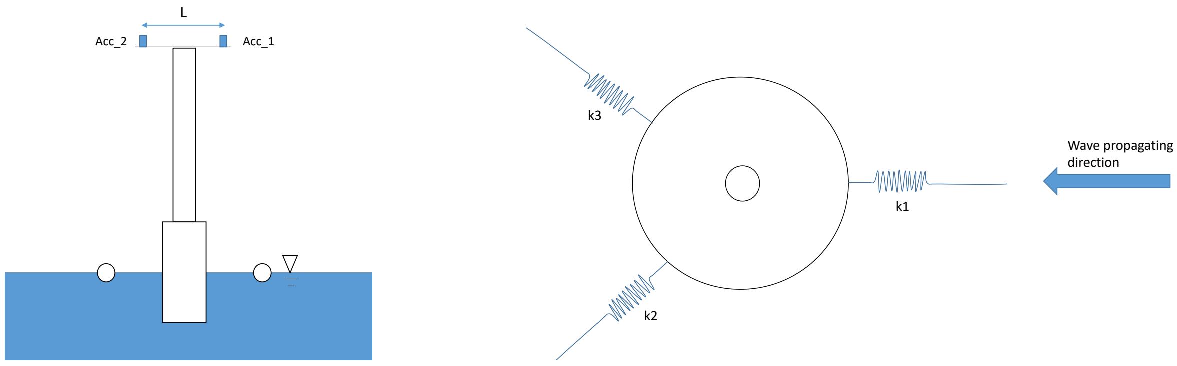
L
Acc_2
Acc_1
k3
k1
k2
Wave propagating direction

(a) Accelerometers (b) Spring system

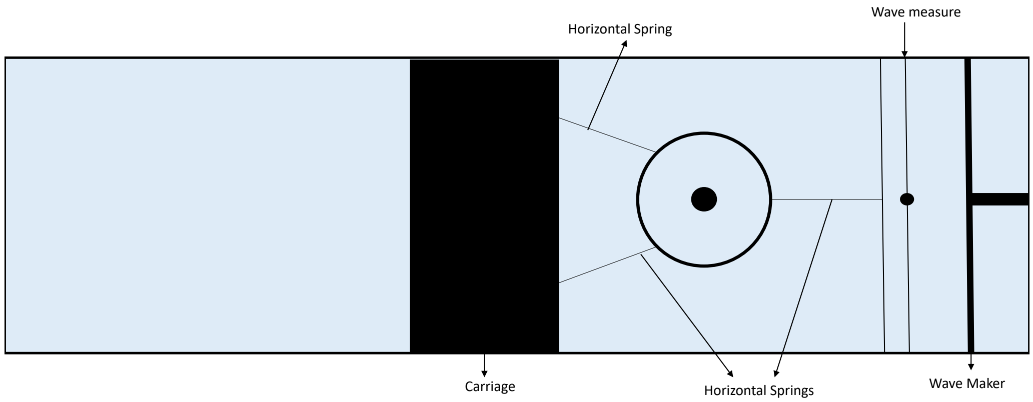
Horizontal Spring
Wave measure
Carriage
Horizontal Springs
Wave Maker

(c) Tank dimensions

Figure C.2: Experimental model setup (Taken from [32])

The tank dimensions are shown in Table C.3.

Table C.3: Tank facility dimensions

Length	**Width**	**Depth**	**Wave maker**
25 m	2.8 m	0 .65 m	Piston wave maker

The accelerometer description is shown in Table C.4.

Table C.4: Accelerometers description

Accelerometer 1	**Accelerometer 2**	**L**
Direction: Normal to the plate	Direction: Normal to the plate	0.155 m

The mooring lines are modelled as horizontal spring stiffness in this Master's thesis. The stiffness for model scale and full scale is shown in Table C.5.

Table C.5: Full-scale and model-scale mooring stiffness

	Model-scale	**Full-scale**
$k1_x$	3.91 N/m	17201.8 N/m
$k2_x$	3.63 N/m	11749.0 N/m
$k2_y$	2.1 N/m	20350 N/m

These values are established on behalf of having a natural periods of 60 seconds in the horizontale planes.

Appendix D

Software Background

The software background consists of GeniE, HydroD, 3DFloat and Matlab. The software flowchart for this thesis is seen in Section 4.1.

D.1 GeniE and HydroD (WAMIT)

The relevant DNV Sesam software used in this Master's thesis are GeniE and HydroD. The total Sesam package has the possibility to solve the whole problematic described in Chapter 2. However will just two programs of the whole software be used, GeniE and HydroD, since 3DFloat is utilized. This section will describe the background within each software.

DNV GeniE is a panel model generator program. A panel model is in practice only the design of the structure, where the structure is divided into n number of panels. The panels can be related to meshes for general FEM programs. The FO OFWT design is designed within this program and shown in Figure D.1, with respect to the numerical model dimensions shown in Table 3.1.

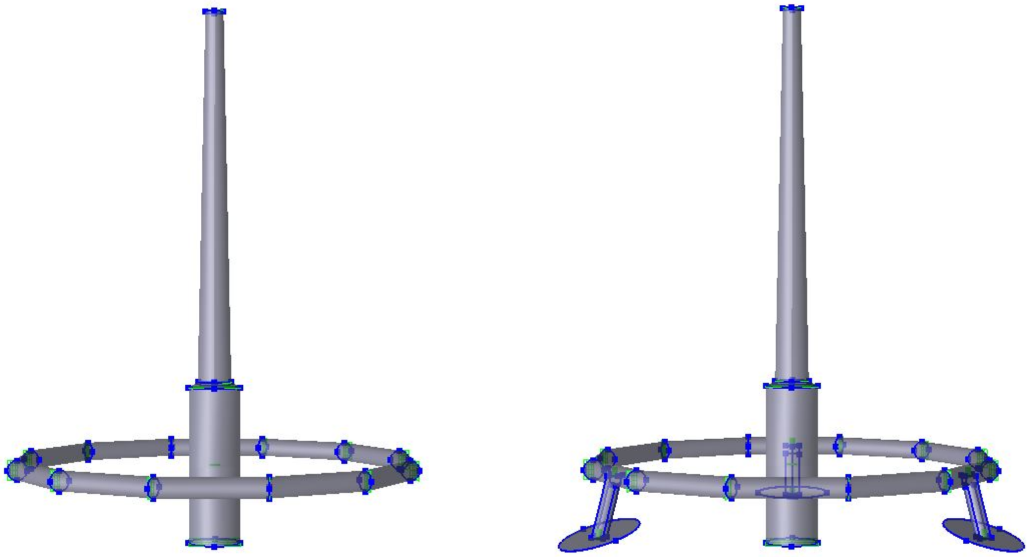

(a) Model (b) Model with heave plates

Figure D.1: GeniE models with and without heave plates

Figure D.1 does not show the panels for the structure w/ and without heave plates, but only a model consisted of shell elements. Each shell element has an associated thickness and material type. It is further observed that neither the spokes or mooring lines are designed in GeniE. This is because all elements move rigidly together. The structural parts that contribute to the freely floating hydrodynamical loading are of main interest, and that is why neither spokes or mooring lines are attached[1]. The static loads are applied in GeniE by defining a Load Condition 1 (LC1) which defines the hydrostatic pressure when the structure is freely floating. This OFWT concept has hydrostatic pressure on half the column and torus volume. It is possible to perform further hydrostatic and hydrodynamic loads analysis with these parameters defined. This is done in HydroD where the panel model is an input file.

The panel model from GeniE is exported into HydroD through the *.FEM file. This file contains all panels, the associated material properties, and LC1. HydroD is a program that performs stability and hydrodynamic analysis of various floating structures. The floating structure that will be evaluated in this thesis is the OFWT concept, and this structure is shown in Figure D.2.

---

[1] It should be noted that mooring lines will contribute to the hydrodynamic loads, but the mooring lines are included in the time-domain response generator. Mooring lines are removed in GeniE and HydroD, to not double count the mooring contribution.

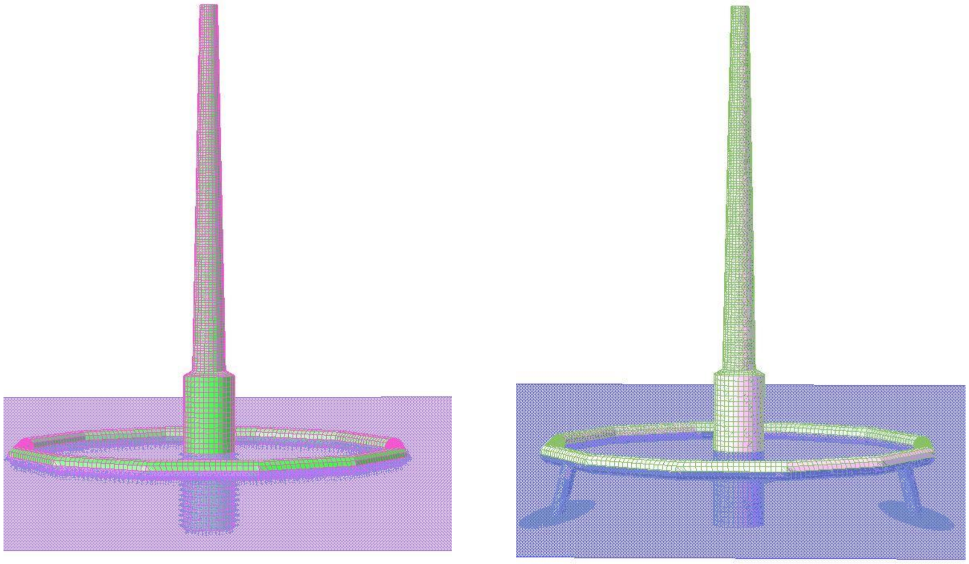

(a) Model

(b) Model with heave plates

Figure D.2: HydroD models with and without heave plates

Figure 4.2 shows the model w/ and without heave plates freely floating at the mean sea water line. If the reader were to look more closely can the structural panels and the hydrostatic pressure arrows be seen. HydroD calculates the total hydrostatic and hydrodynamic load from integration over all panels. This means that a larger number of panels increases the accuracy, but increases the computational time as well.

HydroD can perform stability analysis by establishing the structural restoring when the structure is forced to rotated. The restoring curve for each angle results in a GZ curve, describing the structural stability. This curve was established in the project thesis and is shown in Appendix C.3.

The hydrodynamic analysis consists of frequency dependent coefficients, describing the radiation and diffraction problem, described in Section 2.2.3.1. The hydrodynamic coefficients for the LPT formulation are frequency, water depth and wave heading angle dependent. The water depth is initially set in HydroD. The hydrodynamical analysis in HydroD runs various cases with constant wave height and varying wave periods to establish the hydrodynamic properties for all frequencies and wave heading angles. The core program that performs the hydrodynamical analysis is the software WAMIT [3]. The results from the hydrodynamic analysis are two relevant output files, *.1 and *.3 file, describing the radiation and diffraction force respectively for each wave case with different frequency and heading angle.

The added mass at infinite frequency can not be obtained using HydroD, but an approximated value can be established by running an analysis for a very high frequency. This will be the method for this Master's thesis.

The hydrostatic, hydrodynamic and added mass at infinite frequency coefficients are input values to 3DFloat if an LPT formulation is selected. The time-domain response solver will be presented in the next section.

D.2 3DFloat

3DFloat is an aero-servo-hydro-elastic time-domain response solver for an offshore wind turbine [40]. This sums up Chapter 2 in a way, where 3DFloat solves the response problem on behalf of external and internal loads. 3DFloat uses a core program developed by IFE [1], and to run this program must an input file be defined. The input file varies on what type of analysis one shall perform. This thesis will involve four analysis types: LPT analysis[2], Morison's analysis[3], decay analysis[4] and Eigenvalue analysis[5]. The chosen analysis method changes the input file, but in a general manner will the input file consist of:

- *Environmental parameters*: The environmental parameters consist of ocean waves, ocean wind, and ocean current. 3DFloat has the option to change all of these independently.
- *Structural dimensions and properties*: Each element of the structure has a start node and an end node. These are defined with a given diameter and thickness. These elements can be defined as non-buoyancy, horizontal cylinder, vertical cylinder and so on. The relevant option can be seen in by the *help functions* of the software ([1]).

---

[2] An LPT analysis consists of both rigid and flexible elements

[3] Pure Morison's elements. These are flexible

[4] The elements depends on LPT or Morison's formulation

[5] Pure Morison's elements. These are flexible

- *Drag and mass coefficient*: It is possible to apply selected values for drag and mass coefficients for each element. It is otherwise possible to apply a global drag and mass coefficient which is applied to all elements.
- *Simulation properties*: The simulation properties consist of the simulation time, time step and so on. It is also possible to select the numerical integration method and the input for performing such an integration method. It is also possible to increase the number of Gauss point for each element to get the variational loads along a significantly long element.
- *Linear and quadratic damping*: Linear and quadratic damping can be applied at a node for your own wish. This is to account for linear and nonlinear effects, which is not included in the general hydrodynamic theory.
- *Mooring lines*: The mooring lines must also be defined, whether it is catenary mooring lines or spring stiffnesses.
- *Wind turbine formulation*: The wind turbine can be defined as a point mass, or as the actual rotor. Further description of the generator, pitch control type and so on can also be defined in the input file.

These input parameters for each run are changed using scripts, developed by Jonas Sjolte and modified by the author. The next tables will respectively inform the reader of the default changes in 3DFloat, and which changes that must be done in order to run 3DFloat for a selected analysis.

The default parameters are shown in Table D.1.

Table D.1: Default parameters

Input parameters	**Default**
Environmental parameter	Small wave height, long wave period, no wind
Structural Properties	Initial values applicable for Morison's elements
C_M	Global value is 2.0, unless other values are specified
C_D	Global value is 1.0, unless other values are specified
$A(\omega)$	Frequency dependent added mass and at infinite frequency is 0
$B(\omega)$	Frequency dependent potential damping is 0
Wind turbine	A nrel 5MW rotor is connected to the tower (Based on [25])

This table shows that the default parameter conditions is for an analysis where the structure (pure Morison's elements) is freely floating in the sea surface. The mass and drag coefficients for the specified element will be investigated in Table 4.1. Table D.2 shows whether parameters for a selected analysis must be changed from the default parameters.

Table D.2: Changes from default parameters in 3DFloat

Input	**Analysis, LPT**	**Analysis, Morison's**	**Decay analysis**	**Eigenvalue analysis**
Env. Par.	Yes	Yes	No	No
Struct. Prop.	Yes	Yes	No	No
C_M	Yes	No	No	No
C_D	No	No	No	No
$A(\omega)$	Yes	No	No	No
$B(\omega)$	Yes	No	No	No
WT	Yes/No	Yes/No	Yes	Yes

The LPT analysis formulation is connected to the output files from HydroD, Section D.1. The environmental parameters must be changed so that a meaningful analysis will be performed. The most special change for structural properties is that buoyancy is turned off. This is because the hydrostatic parameters are applied at one certain node, that gives the structural a *virtual* stability. The structural parameters of the elements must, also, be changed so that the LPT formulation is correct. The horizontal elements must be defined as $closed_{horizontal}$ so added mass along the torus is not double counted. A thorough explanation of this can be seen in Appendix D.4. The structural elements must also have mass coefficients equal to 0 since the elements shall not calculate the added mass. The added mass is included from the frequency dependent added mass in the output from HydroD. The frequency dependent damping coefficients, frequency dependent excitation force, and added mass at infinite frequency must also be included in the input file, in addition to the frequency dependent added mass. The wind turbine can both be modeled as the actual rotor or as an equivalent point mass. If comparisons shall be performed is the equivalent point mass chosen, while the NREL 5MW rotor is chosen for FLS and ULS study.

The Morison's analysis is to some degree similar to the LPT analysis. The differences are that the output files from HydroD are not included in 3DFloat, mass coefficients are applied, and buoyancy is turned on.

The decay analysis follows the default parameters for Morison's formulation, while the changes from Table D.2 in an LPT formulation. The wind turbine is replaced with an equivalent point mass during decay comparison, to replicate experimental results in the best manner.

The Eigenvalue analysis follows the default parameters without the NREL rotor. The eigenvalue analysis is used for establishment of Rayleigh damping coefficients (Equation 2.32) or to establish the resonant frequencies for the tower.

Independent of the selected analysis, is the structural model from a 3DFloat analysis w/ and without heave plates (created from the input file) shown in Figure D.3.

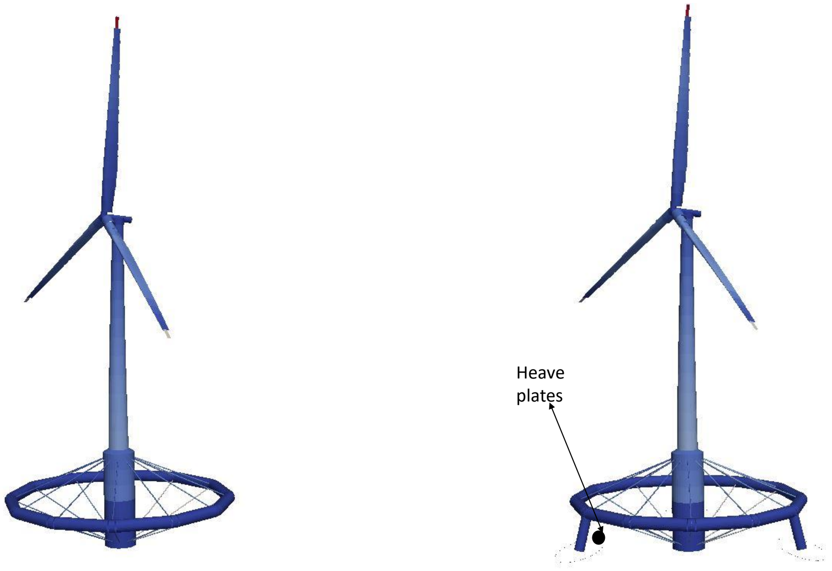

(a) Model (b) Model with heave plates

Figure D.3: 3DFloat model with and without heave plates

The models represented in Figure D.3 are illustrated using an additional program called Paraview 5.0. 3DFloat does not compute visual lids on cylindrical elements, and that is why the heave plate in Figure D.3b is barely visible. The pressure from the lids on each element is chosen in the structural properties in the input file.

D.3 Matlab

The post - processing of experimental and numerical results is done using Matlab. This section will describe scripts that:

1. Import results from experimental and numerical results
2. Compare the numerical and experimental results
3. Verifies design checks for FLS and ULS

D.3.1 Import from Experimental and Numerical Tests

The results from numerical and experimental tests must be organized in a systematized manner, such that the overview of all results are good. The functions extractMassFromLogfile.m and resTols.m are scripts developed by Jonas Sjolte (FO company), and its purpose is to organize the results from a specific run in a user-friendly manner.

The experimental data did not follow the same setup, as the results from the numerical run. The code for the formulation of the numerical results was good, and the solution was to express the experimental results data in the same manner as the numerical results. The code generateStruct.m performs this transformation from the experimental data log file to a result file which is comparable with the numerical results.

The code generateStruct.m has several subfunctions that post - process decay and regular wave tests. The experimental data log file consisted of sea elevations and accelerations for the two accelerometers. This measurement system is shown in Figure 3.3. The subfunctions for post-processing decay and regular wave tests included filtering of frequencies and integration to establish the motion. The filtering of frequencies was performed by using a high pass filter.

D.3.2 Comparison

The numerical and experimental comparison, from the generated results from the scripts resTols.m and generateStruct.m, is seen necessary to verify whether the numerical model is a good representation to the real problem. The script comparison.m imports the relevant numerical and experimental result and performs a comparison study. The script comparison.m has several subfunctions that compare decay and regular wave test, in addition to the determination study of structural and hydrodynamic coefficients. The determination study for hydrodynamic and structural coefficients are presented in respectively Section 4.3.3 and 4.6.

The comparison study will be presented for Morison's and LPT formulation in respectively Chapter 5 and 6.

D.3.3 Design Checks

The long-term responses are established using the 3DFloat software, and these are needed to be post- processed to have meaningful values. The Matlab script buckling_yield_check.m imports the values from numerical results and uses methods in DNV recommended practice to see if the requirements are satisfied.

The FLS and ULS study will be presented for the structure w/ and without heave plates in Chapter 7 and 8.

D.4 Drag Forces for Morisons Representation and LPT Representations

It has been mentioned in previous sections that the external drag force is applied to both theoretical representations. This is one of the reasons why the structural elements are modeled as Morison's elements when 3DFloat computes the loads (based on LPT). The drag and inertia force from the Morison's equation were verified for cylinders piercing the sea surface vertically. The problem arose when horizontal elements were on the sea surface. A software update was required in calculating the drag coefficients, such that added mass was not double counted for elements freely floating horizontally on the sea surface. The results were to differ the excitation force in Morison's equation in two: one for structural motion, and one for fluid motion [33]. The transverse and axial excitation loads on respectively a vertical and horizontal element using Morison's equation, without double counting added mass, are respectively shown in Equation D.1a and D.1b.

$$\frac{F^{\text{Excitation}}}{\text{Length}} = \frac{1}{2}\rho C_D D(u-\dot{\eta})|u-\dot{\eta}| + \rho C_{M_{\text{Flud}}}\frac{\pi}{4}D^2 a_{\text{fluid}} - \rho(C_{M_{\text{Structure}}}-1)\frac{\pi}{4}D^2\ddot{\eta}_{\text{structure}} \tag{D.1a}$$

$$F^{\text{Excitation}} = \frac{1}{2}\rho C_D A_D(u-\dot{\eta})|u-\dot{\eta}| + \rho(C_{M_{\text{Flud}}}-1)V_R a_{\text{fluid}} + F_{FK} - \rho(C_{M_{\text{Structure}}}-1)V_R\ddot{\eta}_{\text{structure}} \tag{D.1b}$$

where u is the fluid particle velocity, $\dot{\eta}$ is the structural velocity, C_D is the drag coefficient, D is the structural diameter, C_{M*} is the mass coefficients, A_D is the cross section area and F_{FK} is the dynamic pressure force.

The mass coefficients in Morison's equation for the LPT and Morisons formulation are shown in Table D.3.

Table D.3: Mass coefficient for LPT and Morison's formulation

	$\mathbf{C_{M_{\text{Flud}}}}$	$\mathbf{C_{M_{\text{Structure}}}}$
LPT horizontal	0	1
LPT vertical	1	1
Morison horizontal	$C_{M_{\text{Flud}}}$	$C_{M_{\text{Structure}}}$
Morison vertical	$C_{M_{\text{Flud}}}$	$C_{M_{\text{Structure}}}$

If $C_{M_{\text{Fluid}}}$ is equal to 1 in Equation D.1b, turns 3DFloat the dynamic pressure term off.

D.5 Added Mass at Infinite Frequency

The added mass at infinite frequencies for respectively without and w/ heave plates are shown in following tables.

$$\mathbf{A}_{\infty} = \begin{bmatrix} 1.659E+06 & 1.159E+05 & 2.683E+05 & -2.566E+05 & -4.700E+06 & 9.328E+04 \\ -7.238E+05 & 1.506E+06 & -5.761E+05 & 5.669E+06 & 4.438E+05 & -1.960E+05 \\ 7.436E+02 & -8.695E+02 & 6.025E+05 & 8.159E+03 & 4.326E+03 & 2.125E+05 \\ -5.861E+06 & 6.264E+06 & -3.933E+05 & 1.164E+09 & -4.620E+06 & -1.450E+05 \\ -7.101E+06 & -3.365E+05 & -2.193E+06 & 1.019E+07 & 1.166E+09 & -7.472E+05 \\ 8.624E+03 & -6.746E+03 & -7.460E+05 & 2.746E+04 & 3.359E+05 & 2.200E+07 \end{bmatrix} \tag{D.2}$$

$$\mathbf{A}_{\infty} = \begin{bmatrix} 2.05E+06 & 6.81E+04 & 7.84E+03 & 2.67E+05 & -2.70E+07 & 1.93E+04 \\ -3.54E+06 & 1.10E+06 & -2.29E+05 & 2.14E+07 & 9.18E+06 & 6.32E+05 \\ -1.07E+05 & -9.47E+03 & 3.65E+06 & 1.70E+06 & 6.99E+06 & -1.17E+07 \\ -2.52E+07 & 2.57E+07 & -1.25E+07 & 2.26E+09 & 1.18E+08 & 2.89E+07 \\ -4.00E+07 & 7.04E+06 & 4.93E+06 & 2.88E+07 & 2.29E+09 & -2.36E+07 \\ 5.40E+04 & 5.04E+04 & -3.21E+05 & -5.53E+06 & -5.10E+06 & 3.23E+08 \end{bmatrix} \tag{D.3}$$

D.6 Determination of Coefficients

This section outlines the determination of hydrodynamic and structural coefficients needed to obtain acceptable results in comparison and long-term study.

D.6.1 Hydrodynamic Coefficients

Drag, linear damping, and quadratic damping coefficients are the relevant coefficients that need to be determined for the LPT formulation. This study establishes the best numerical model on behalf of combinations of drag coefficients listed in Table 4.1 and random damping coefficients.

The transverse drag force, C_{Dn}, on a column (piercing the sea surface vertically), follows the general law for Morison's elements [15], and is set to 0.7. The axial drag coefficient is more uncertain, but on behalf of a paper written by Xiaohong Chen [9] has C_{Da} been chosen to be 3.

The transverse drag coefficients, C_{Dn}, should be in the range of 0.9-1.1, while the axial drag coefficient, C_{Da}, should be in the range of 0.01-0.02. These drag coefficients depend on same parameters from Table 4.1.

The linear and quadratic damping coefficients are established by guessing random variables, to see what gives best correspondence with experimental results. The linear damping coefficients are applied for heave direction since the measurement in this degree of freedom is assumed to be correct.

Numerical runs with varying drag and damping coefficients are performed to establish the best correspondence. The associated drag coefficients will be for the torus, and the associated damping coefficients will be for linear and quadratic damping. The list of the different runs are shown in Table D.4.

Table D.4: Information and input values for the constant hydrodynamic coefficients

Cases	C_{D_a}	C_{D_n}	B_{linear}	$B_{quadratic}$
1- 5	0.01	0.9	1e5	1e5 - 9e5, dt= 2e5
6- 10	0.01	0.9	3e5	1e5 - 9e5, dt= 2e5
11- 15	0.01	0.9	9e5	1e5 - 9e5, dt= 2e5
16- 20	0.01	1	1e5	1e5 - 9e5, dt= 2e5
21- 25	0.01	1	3e5	1e5 - 9e5, dt= 2e5
26- 30	0.01	1	9e5	1e5 - 9e5, dt= 2e5
31- 34	0.01	1.1	1e5	1e5 - 7e5, dt= 2e5
35- 37	0.01	0.9	1e5	3e6- 7e6, dt= 2e5
38	0.01	0.9	9e4	7e6
39-41	0.01	0.9	6e4-2e4, dt= -2e5	7e6
42-45	0.01	0.9	1e4-10, dt=*1/10	7e6

For each case in Table D.4 are the mean difference between the experimental and numerical motions been calculated. The mean difference for acceleration and heave displacement is shown in Figure D.4.

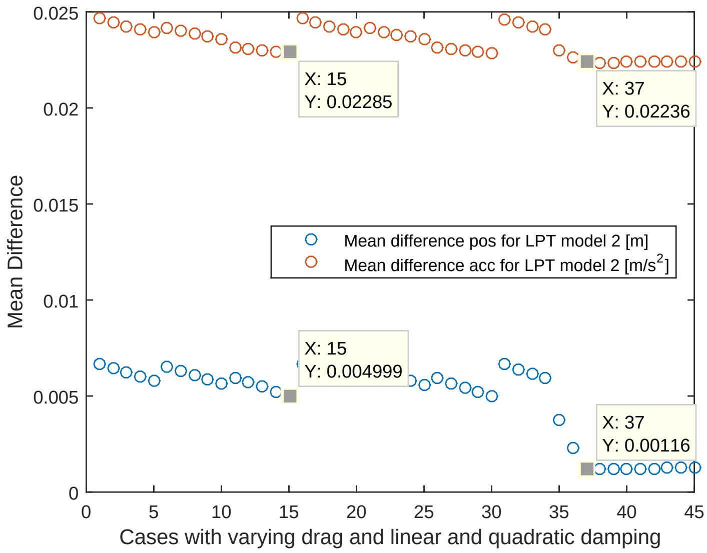

Figure D.4: Mean difference between experimental and numerical motions for constant hydrodynamic coefficients

It is observed that the minimum difference occurs for case 37, from figure D.4. The drag and damping coefficients for this case are however not optimal, due to the method of calculating the mean difference. The mean difference is taken at all points during the simulation, and the majority of the heave response during decay are close to zero. This is why a large damped structure has a low mean difference. A new case, 15, is therefore chosen to establish the coefficients since the numerical behavior fits the experimental behavior much better. The final coefficients are shown in Table D.5, and can be illustrated in Figure 6.1.

Table D.5: Final coefficients for drag and damping

$\mathbf{C_{D_a}}$	$\mathbf{C_{D_n}}$	$\mathbf{B_{linear}}$	$\mathbf{B_{quadratic}}$
0.01	0.9	9e5	9e5

D.6.2 Structural Coefficients

The regular wave test for a structure without structural damping is illustrated in Figure D.5. The regular wave has a wave height of 1.8m and wave period of 10s, and the numerical model is based on the first 3DFloat version with LPT implemented.

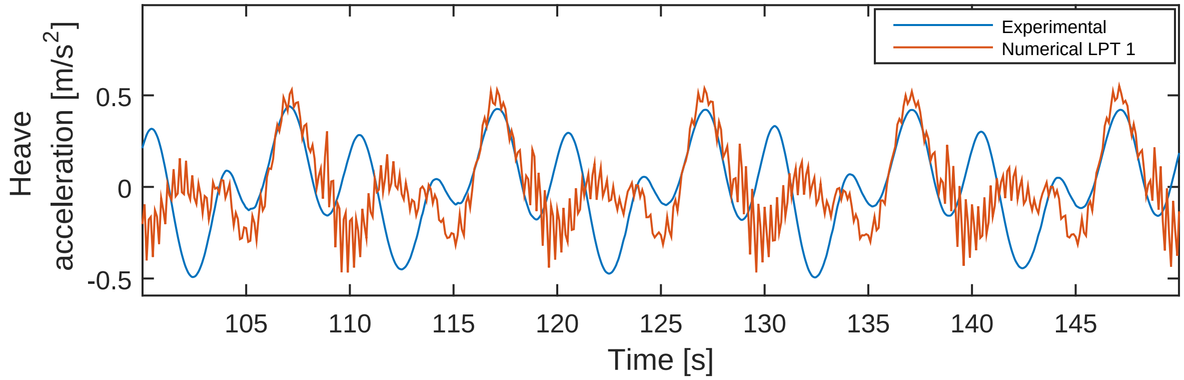

Figure D.5: Regular wave test of the first numerical model

This figure implies the fact that the structure is not rigid, and structural damping must be included. In this thesis will the Rayleigh Damping method be utilized, see Section 2.5.2. There are two ways of calculating these coefficients: Eigenvalue analysis or Determination study.

D.6.2.1 Eigenvalue Analysis

An eigenvalue analysis is performed by 3DFloat for the floater without the implementation of LPT. 3DFloat produces the eigenfrequencies for four different modes (not included the first 6 DOF) and are illustrated in the three first columns in Table D.6). By further assuming a linear correlation between the modes and that the first mode and last mode has a damping ratio of respectively 1 % and 2% is it possible to obtain the damping coefficients. This is shown in column 4 in the same figure.

Table D.6: Natural frequencies versus damping ratio

Mode	Eigen frequency [Hz]	Frequency [rad/s]	Damping ratio
7	4.81E-01	3.022212133	1.00E-02
8	7.70E-01	4.838681005	1.52E-02
9	7.70E-01	4.838681005	1.52E-02
10	1.04E+00	6.54707909	2.00E-02

The rayleigh damping coefficients are from this table calculated to be([10]):

$$\alpha = 0.0059$$

$$\beta = 0.006$$

D.6.2.2 Determination and Comparison Study

The tuning study compares the experimental tests with guessed Rayleigh damping coefficients. The sensitivity study will be done by comparing the experimental and numerical study for the case of:

$H = 1.8$ m

$T = 10$ s

where the structure is exposed to regular waves. In Table D.7 are different input and information listed. The result or mean error between the numerical and experimental regular wave tests are shown in Figs. D.6.

Table D.7: Information and input values for the tuning study

Cases	β	α
1- 8	0 - 0.008	0
9- 16	0 - 0.008	0.002
17-40	0.009 - 0.032	0
40-46	0.042 - 0.092	0
47-65	0.014 - 0.017	0.02 - 0.1
67	0.006	0.0059

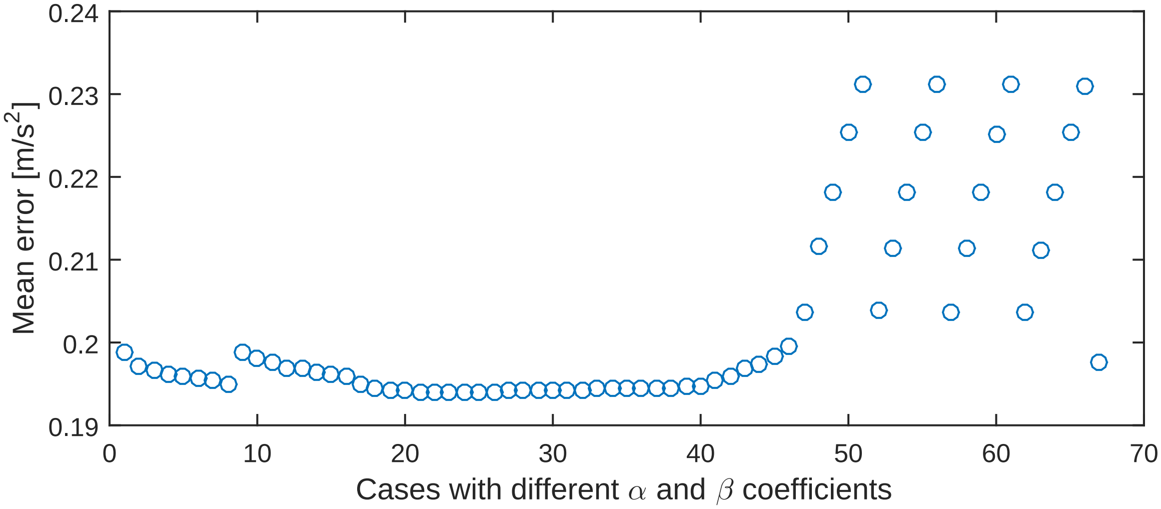

Figure D.6: Mean error between numerical and experimental acceleration for the different cases

The lowest mean value is for case 24, which has $\alpha = 0$ and $\beta = 0.016$. In the same figure is case 67, the coefficients from the eigenvalue analysis, shown. It is seen that it is a good estimate for future knowledge, but for now, will the coefficients from case 24 be used. The impact on the response by using these coefficients is shown in Figure D.7.

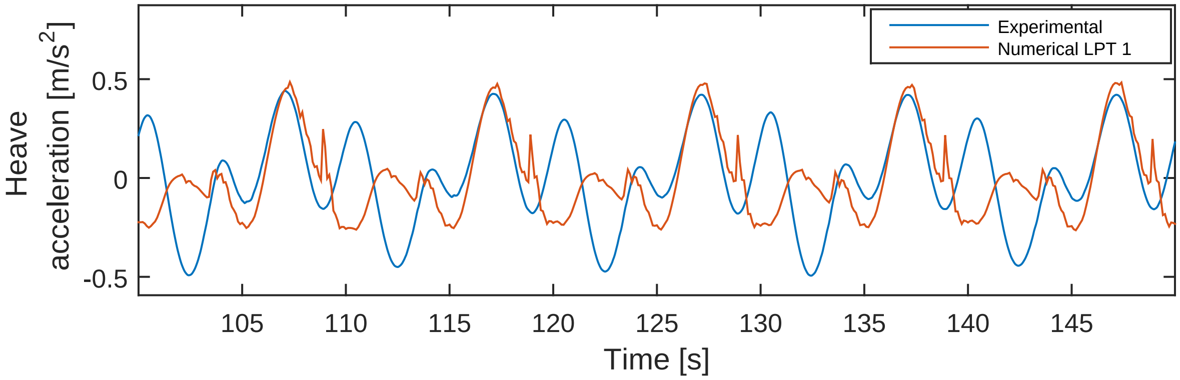

Figure D.7: Numerical results with usage of α equal to 0.016, compared with experimental results

Appendix E

Comparison Between Numerical Morison Model and Experimental Model

The comparison between the numerical Morison's model and the experimental model consist of one decay tests and five regular wave tests.

E.1 Decay

The nonlinear decay test is performed by FO, and is pictured in Figure E.1

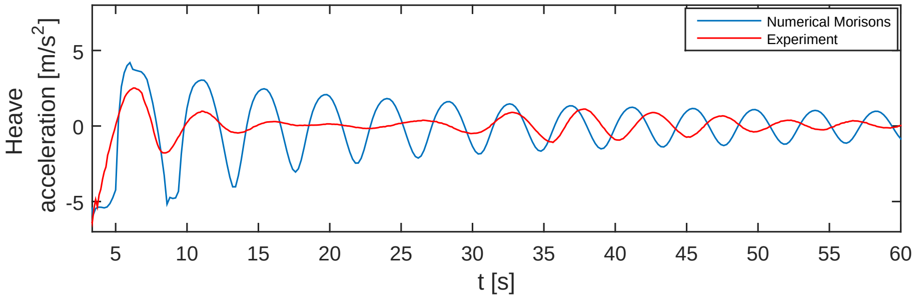

Figure E.1: Nonlinear heave decay a nalysis done by Fred. Olsen

E.2 Regular wave

The regular wave comparison consist of five cases.

Case 1: H of 1.05 m and T of 14.5 s

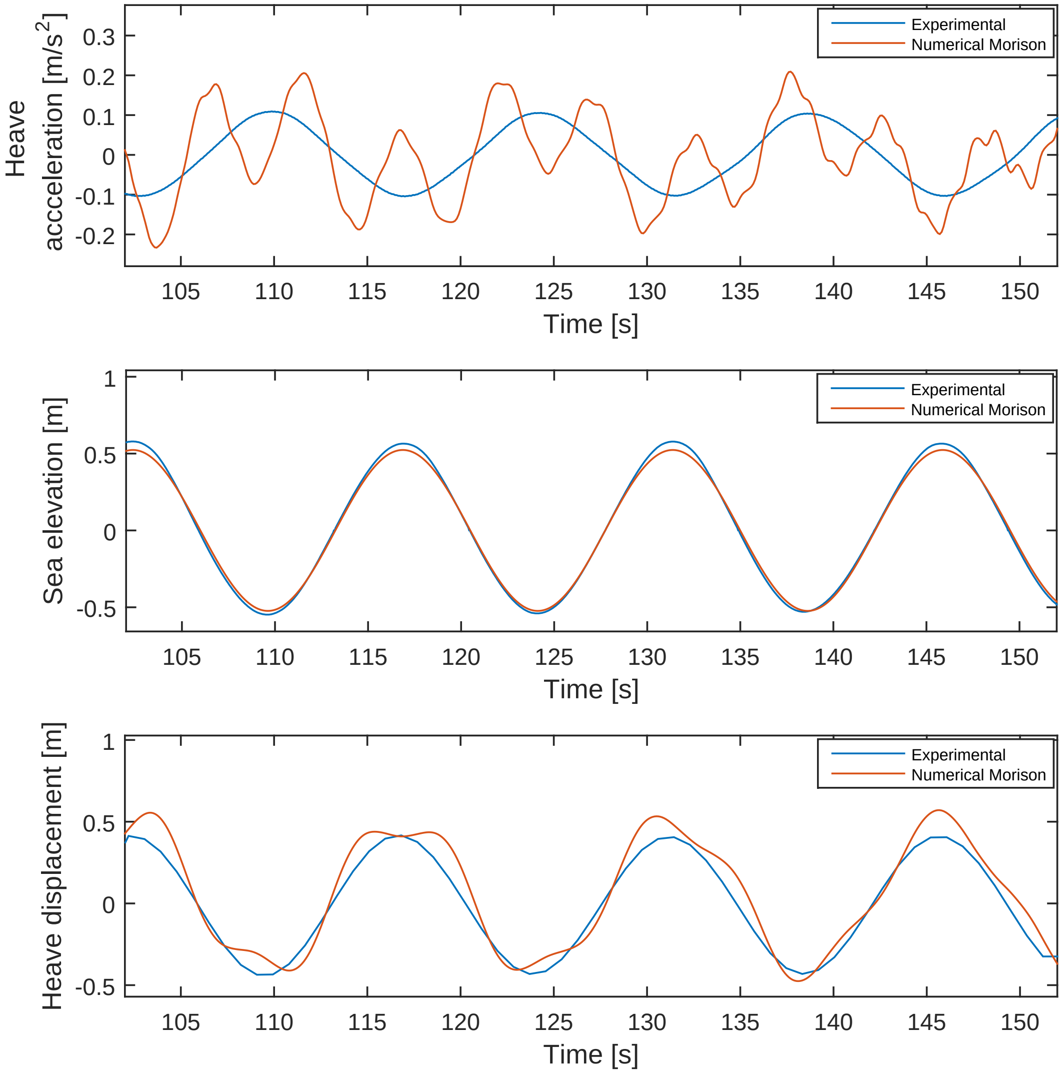

Figure E.2: Comparison of case 1

Case 2: H of 1.8 m and T of 10 s

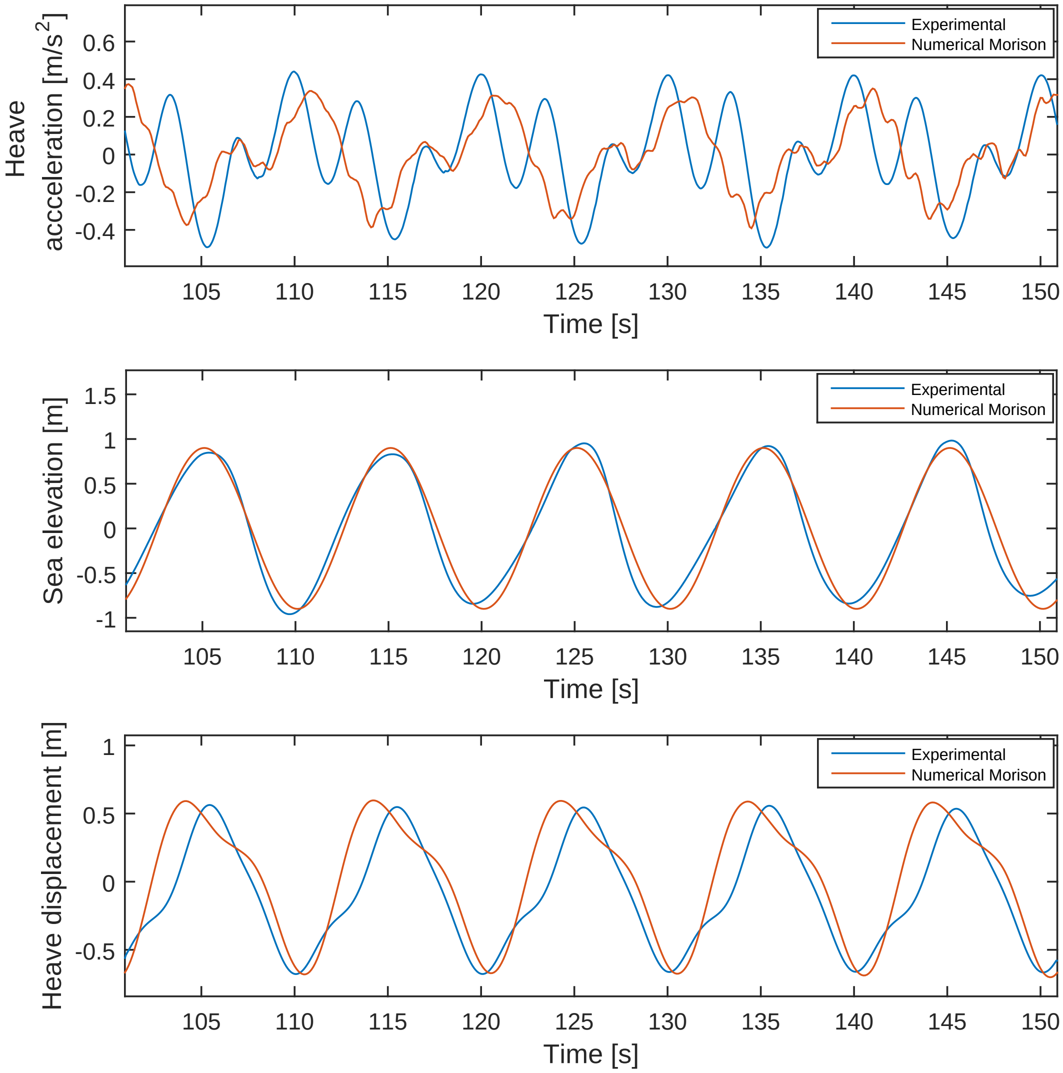

Figure E.3: Comparison of case 2

Case 3: H = 3m and T = 10.5 s

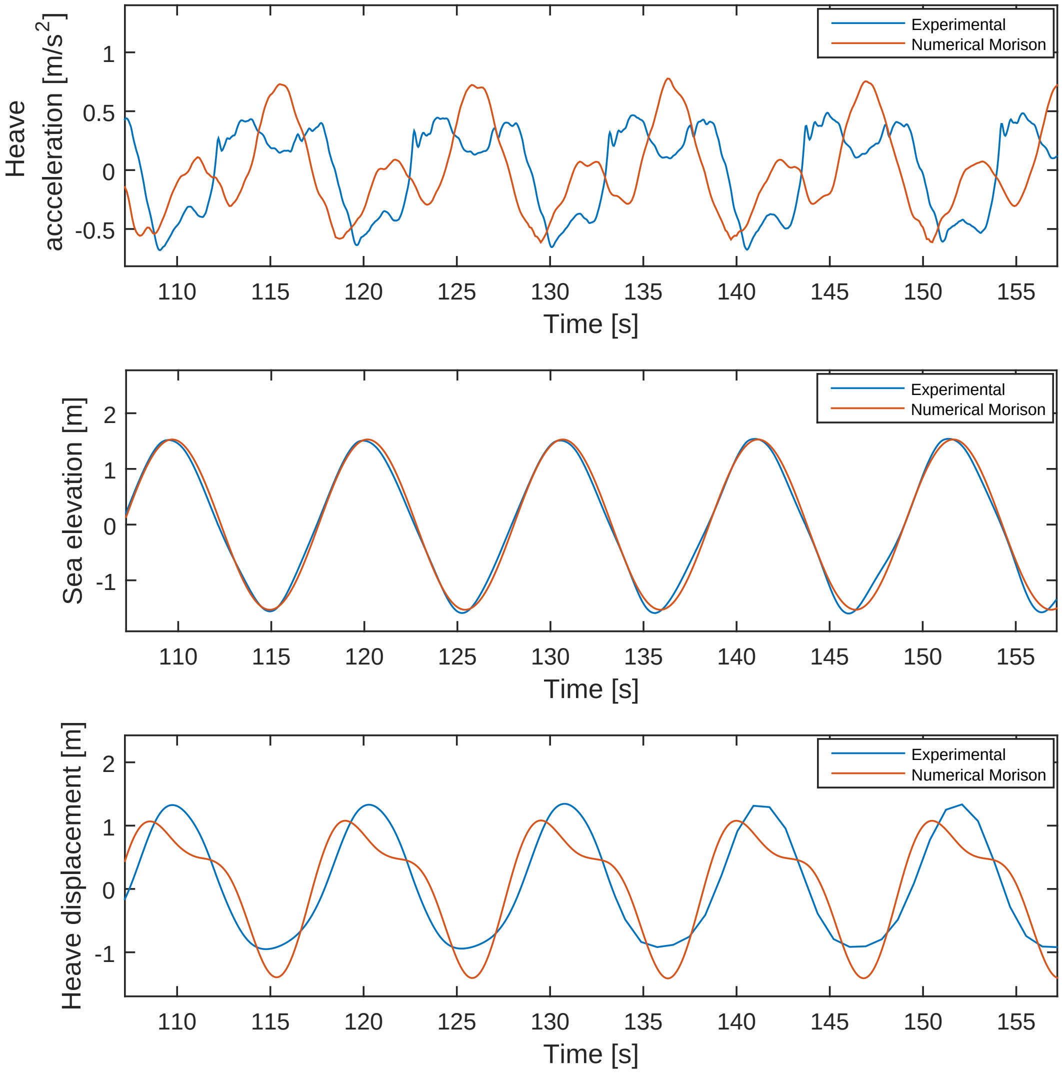

Figure E.4: Comparison of case 3

Case 4: H = 5.86 m and T = 9 s.

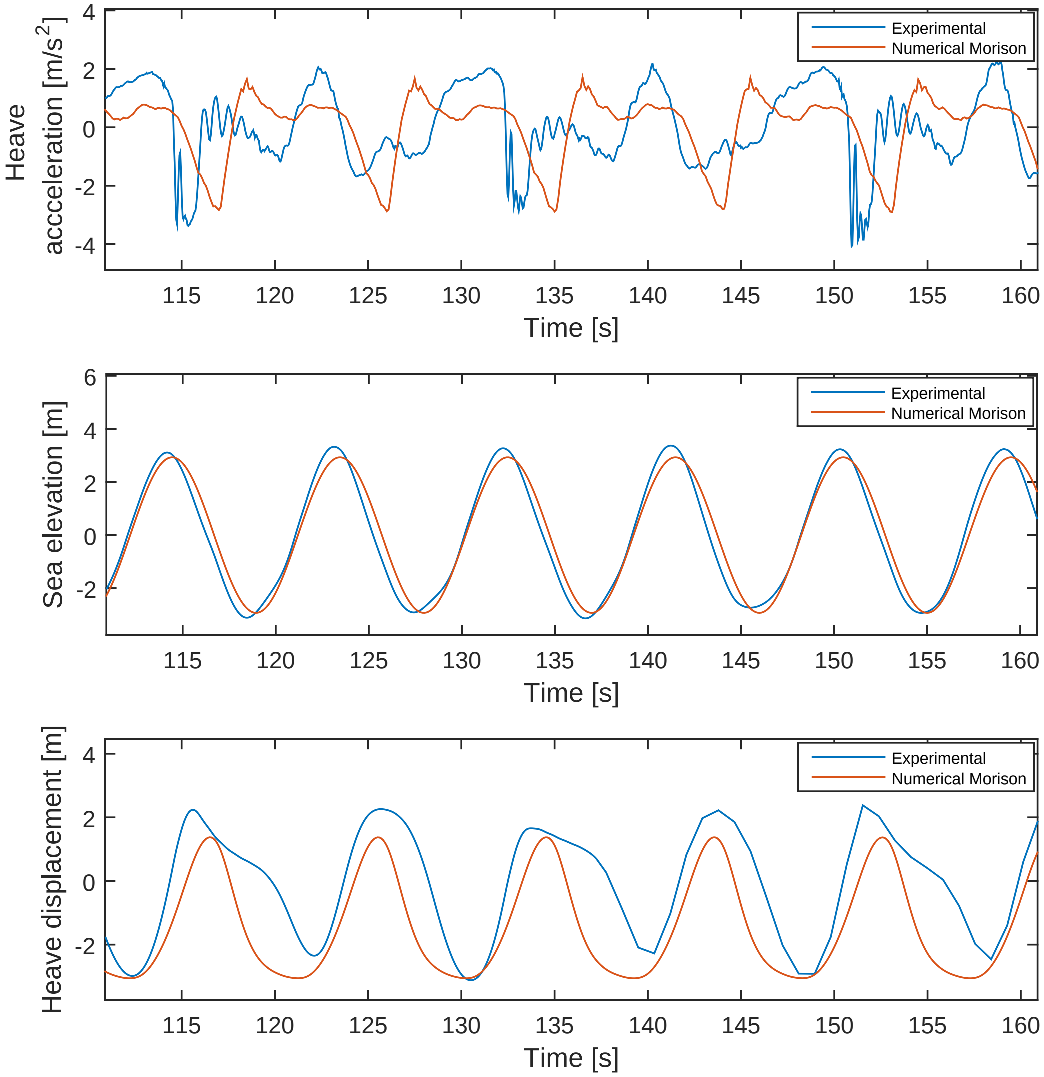

Figure E.5: Comparison of case 4

Case5: H = 2.71 m and T = 9 s.

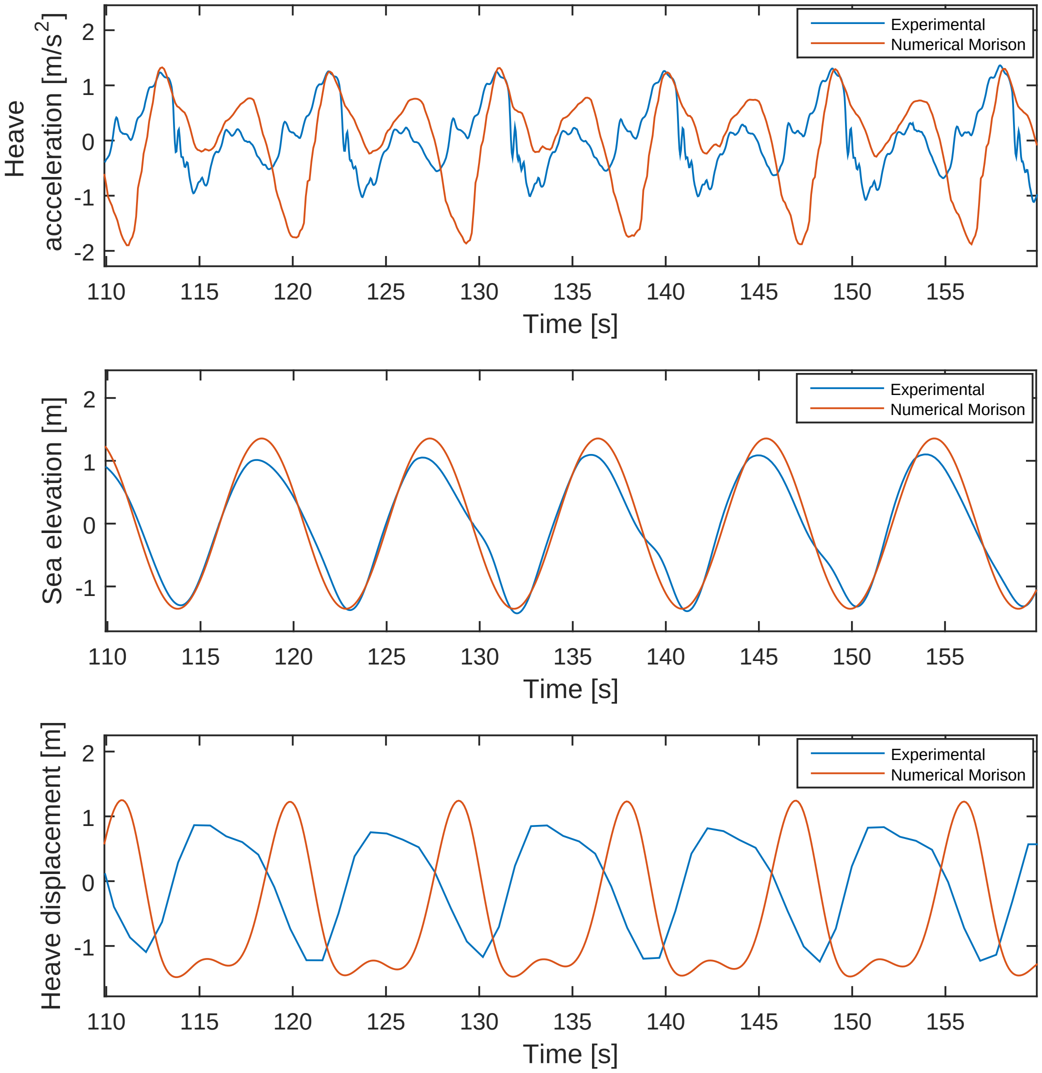

Figure E.6: Comparison of case 5

Appendix F

Comparison Between Numerical LPT Model and Experimental Model

This comparison consist of decay and regular waves.

F.1 Linear Decay

The linear decay comparison is for heave, pitch and heave with heave plates.

Heave

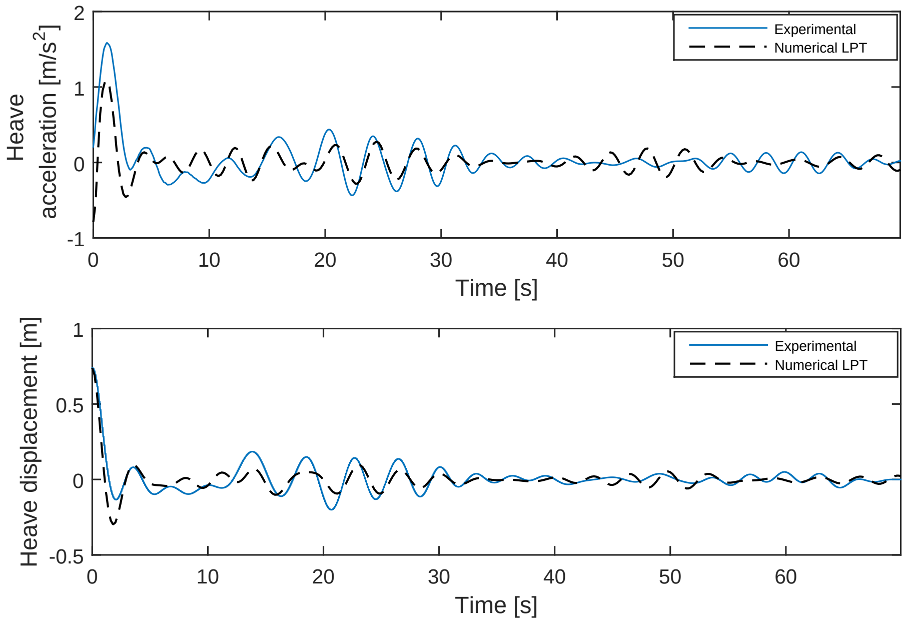

Figure F.1: Linear heave decay motions

Pitch

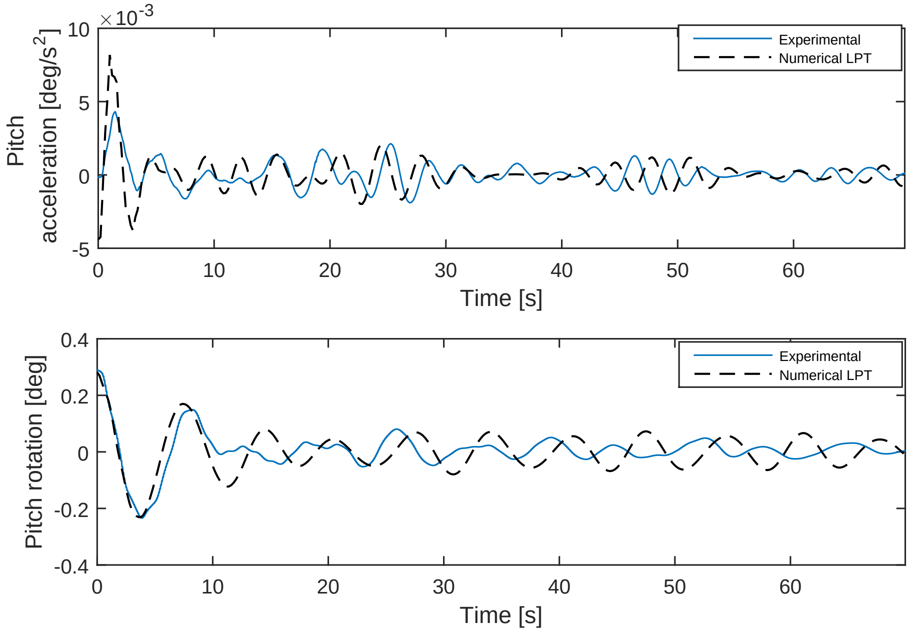

Figure F.2: Linear pitch decay motions

Heave with Heave Plates

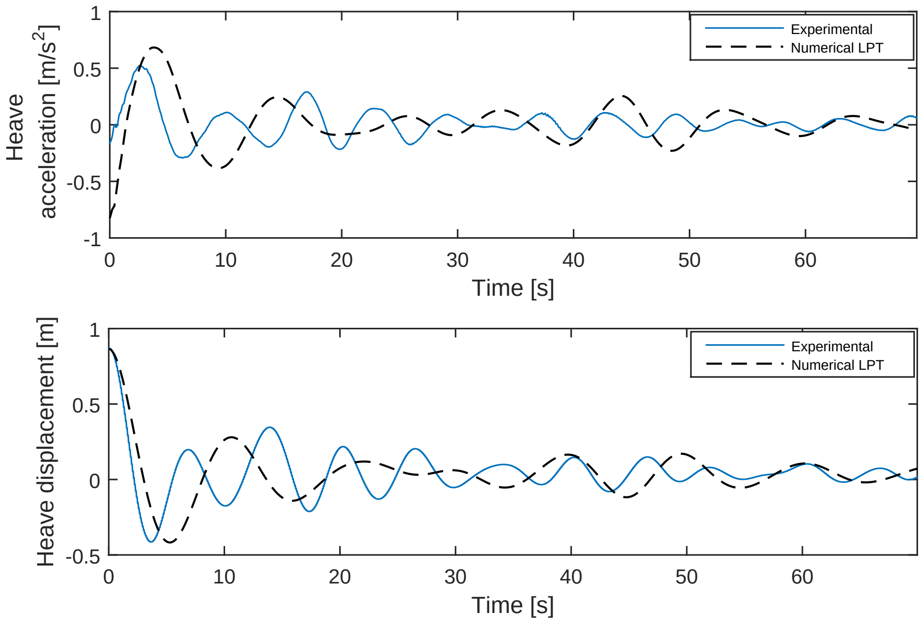

Figure F.3: Linear heave decay motions with heave plates

F.2 NonLinear Decay

The nonlinear decay test comparison is for heave, pitch and heave with heave plates.

Heave

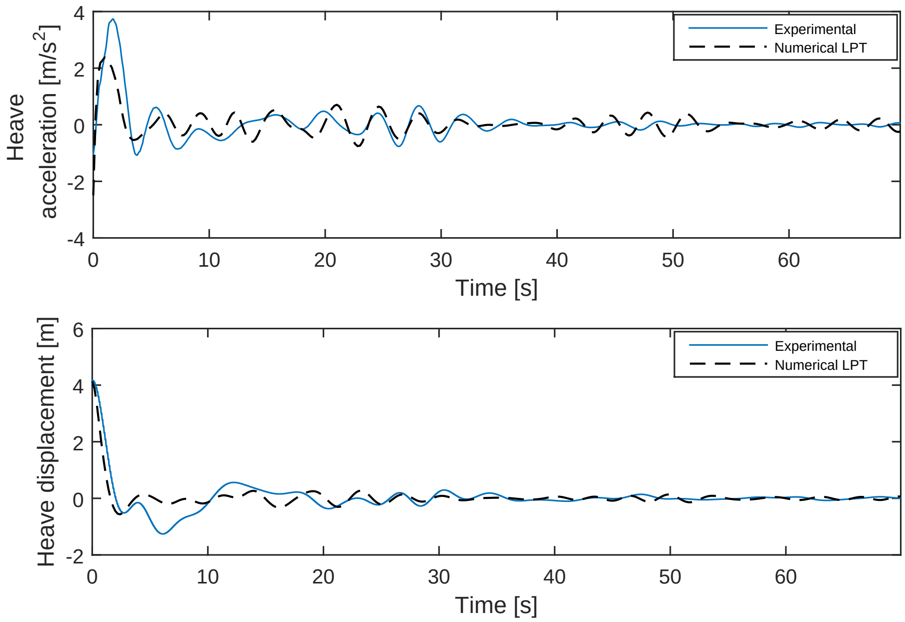

Figure F.4: Nonlinear heave decay motions

Pitch

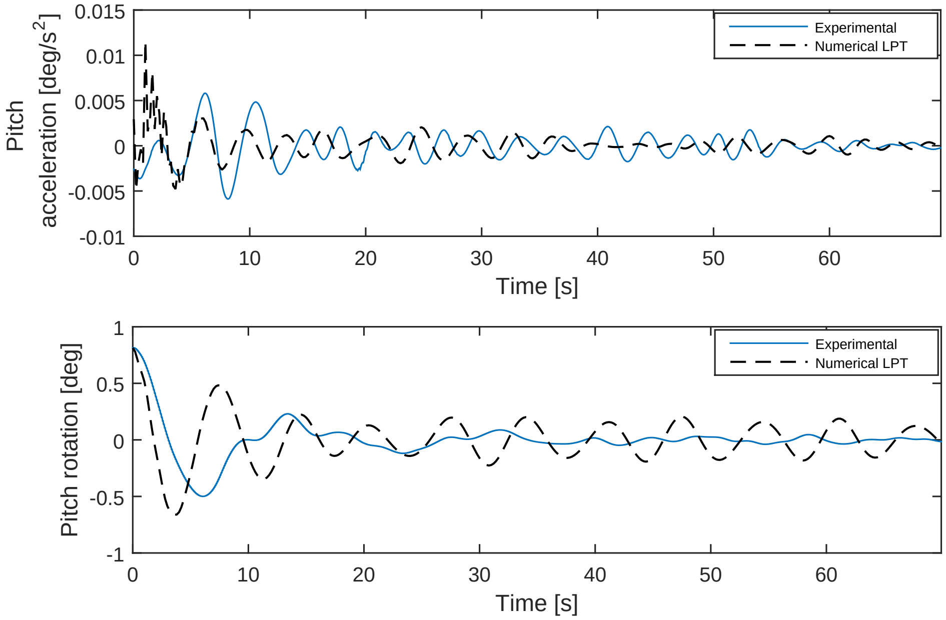

Figure F.5: Nonlinear pitch decay motions

Heave with Heave Plates

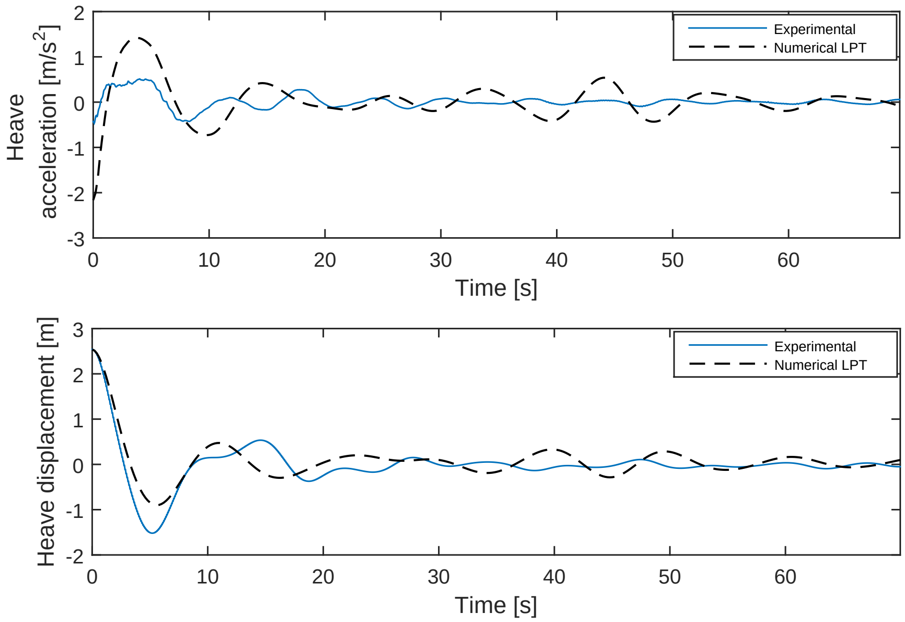

Figure F.6: Nonlinear heave decay motions with heave plates

F.3 Regular Wave

The regular wave comparison consists of six cases; five without heave plates, one with heave plates.

Case 1: Hs of 1.8 m and T of 10 s

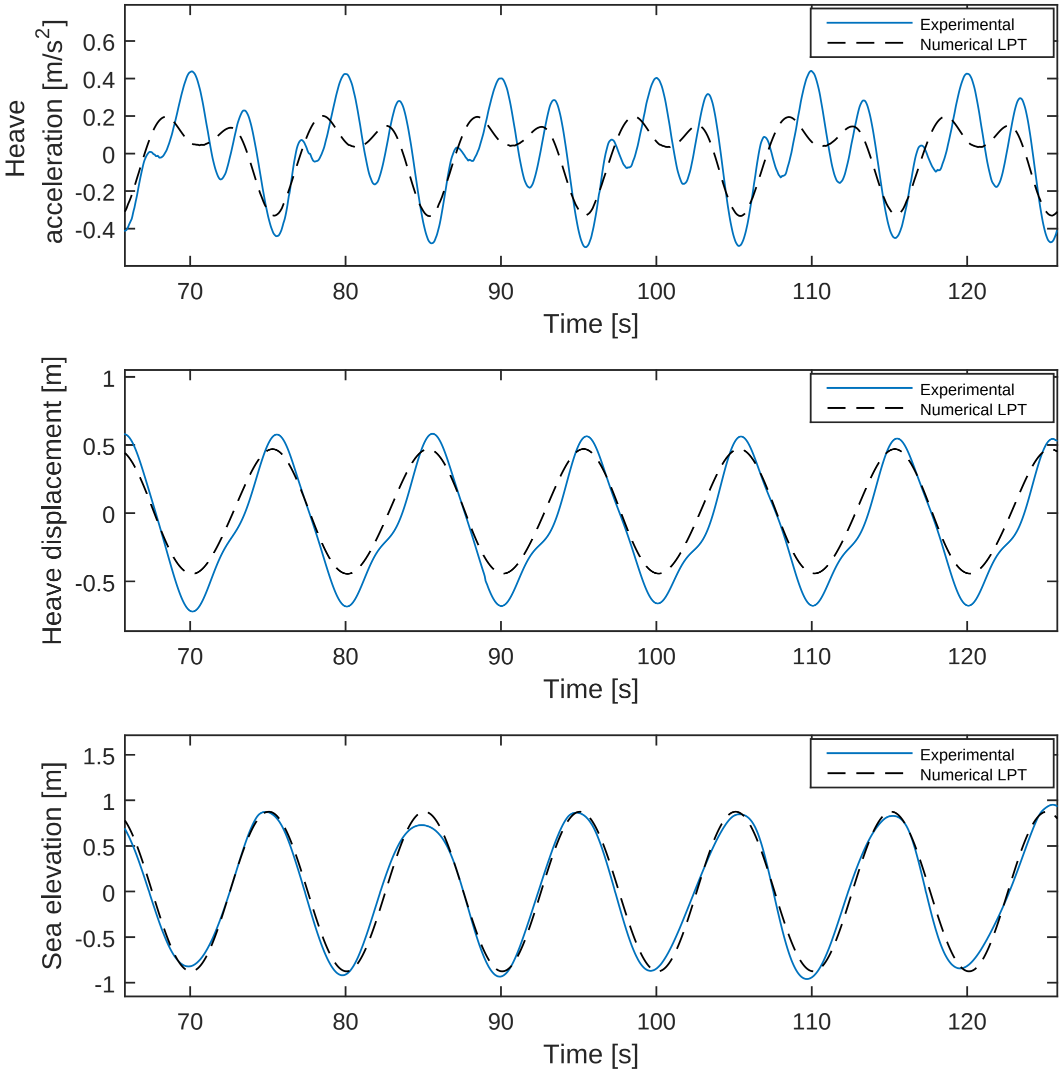

Figure F.7: Comparison of case 1

Case 2: H of 1.05 m and T of 14.5 s:

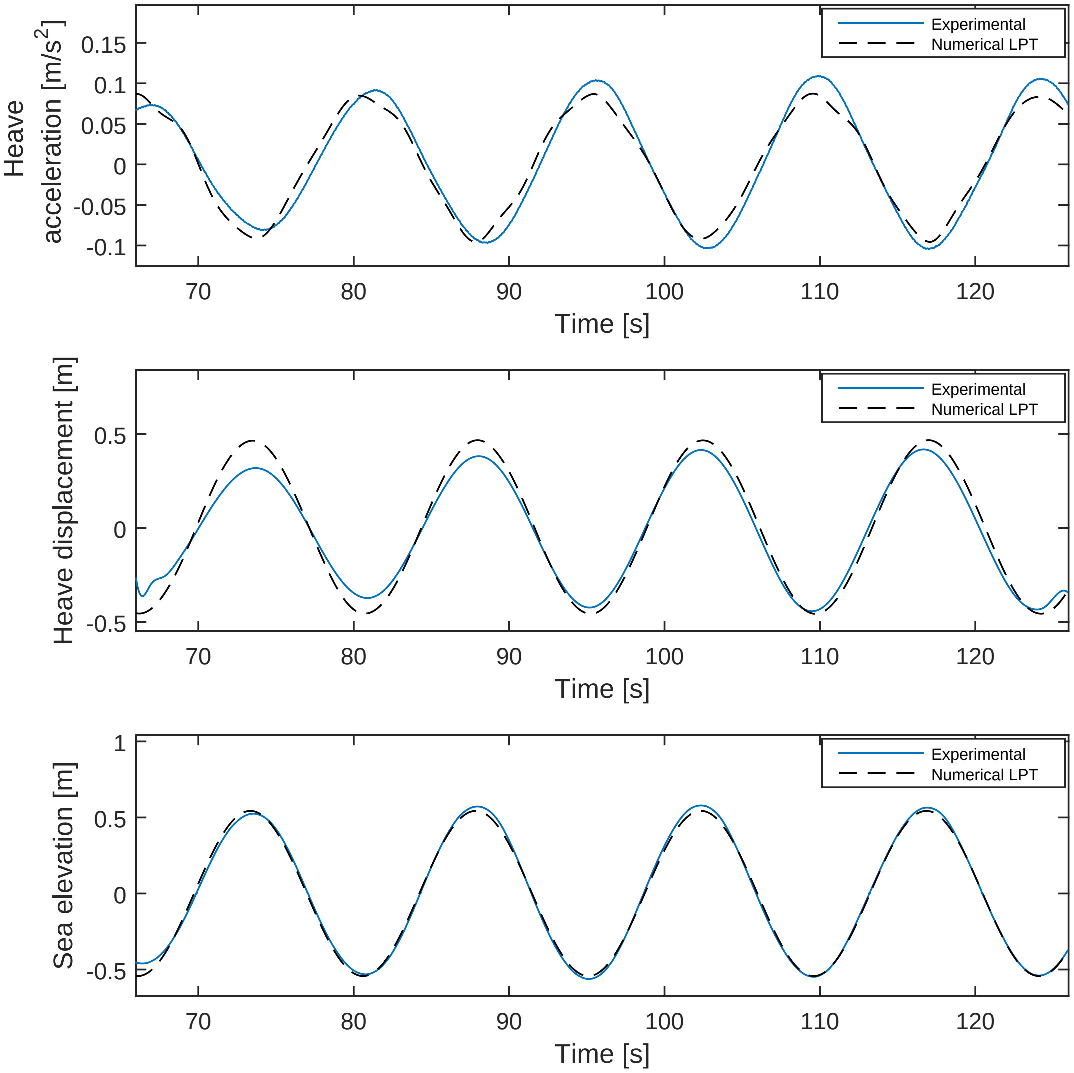

Figure F.8: Comparison of case 2

Case 3: H = 3m and T = 10.5 s

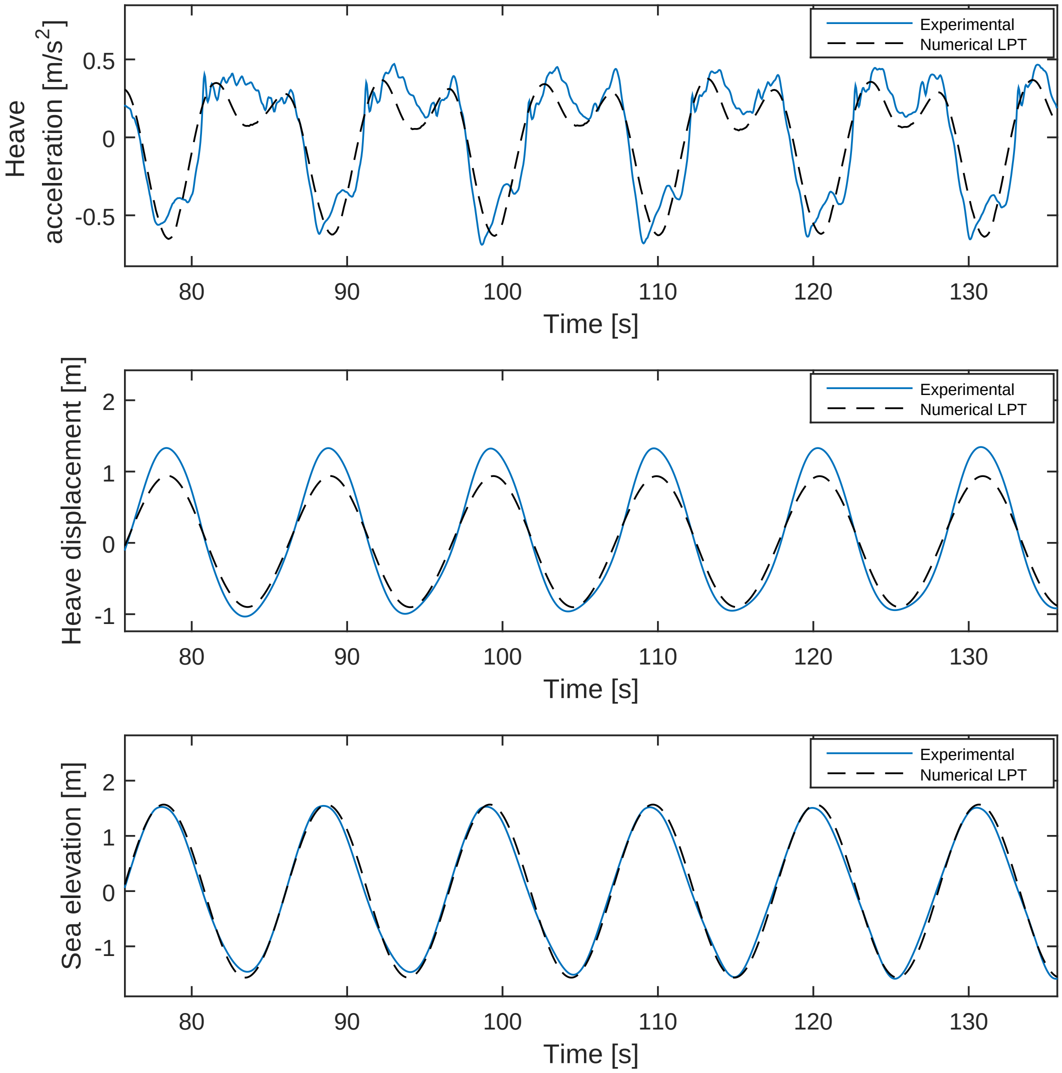

Figure F.9: Comparison of case 3

Case 4: H = 5.86 m and T = 9 s

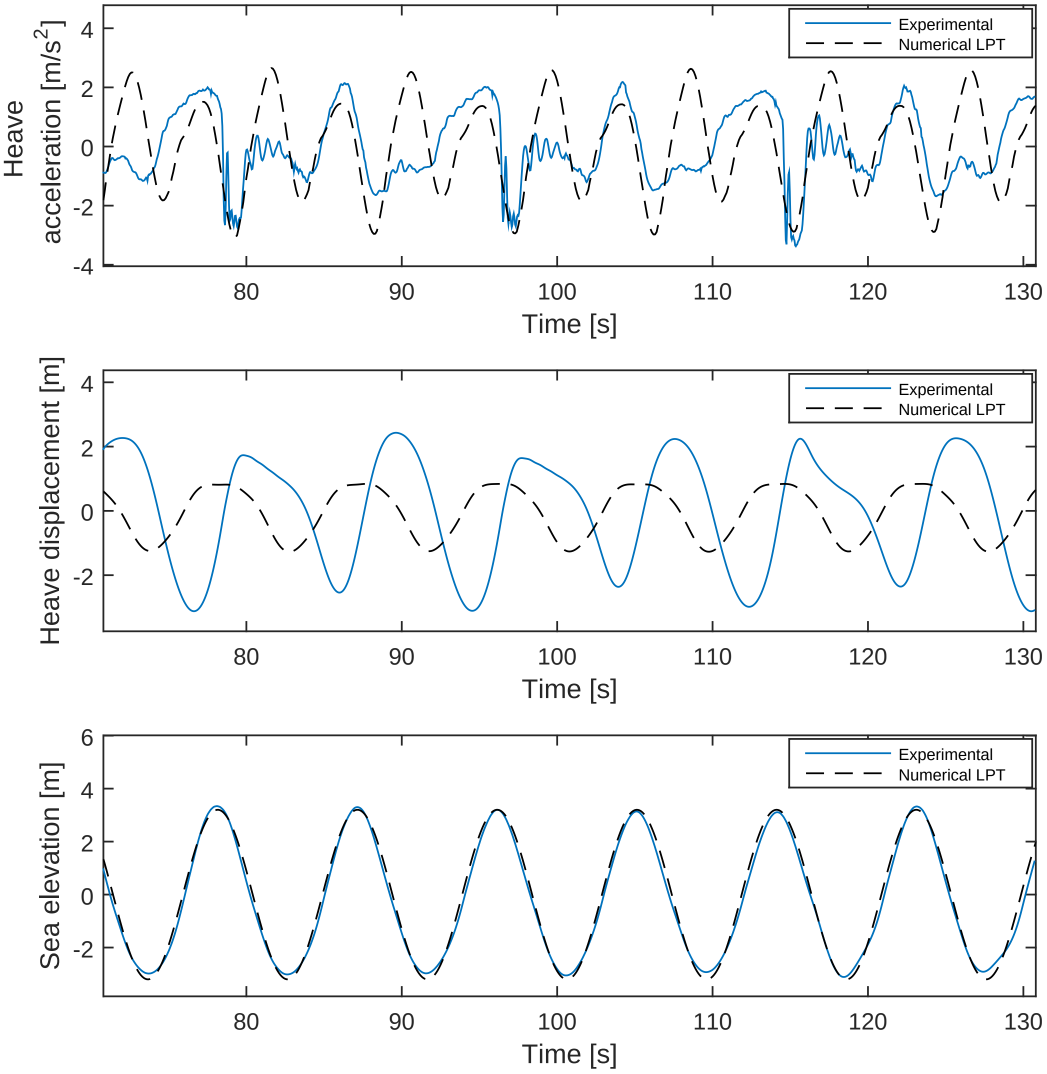

Figure F.10: Comparison of case 4

Case 5: H = 2.71 m and T = 9 s

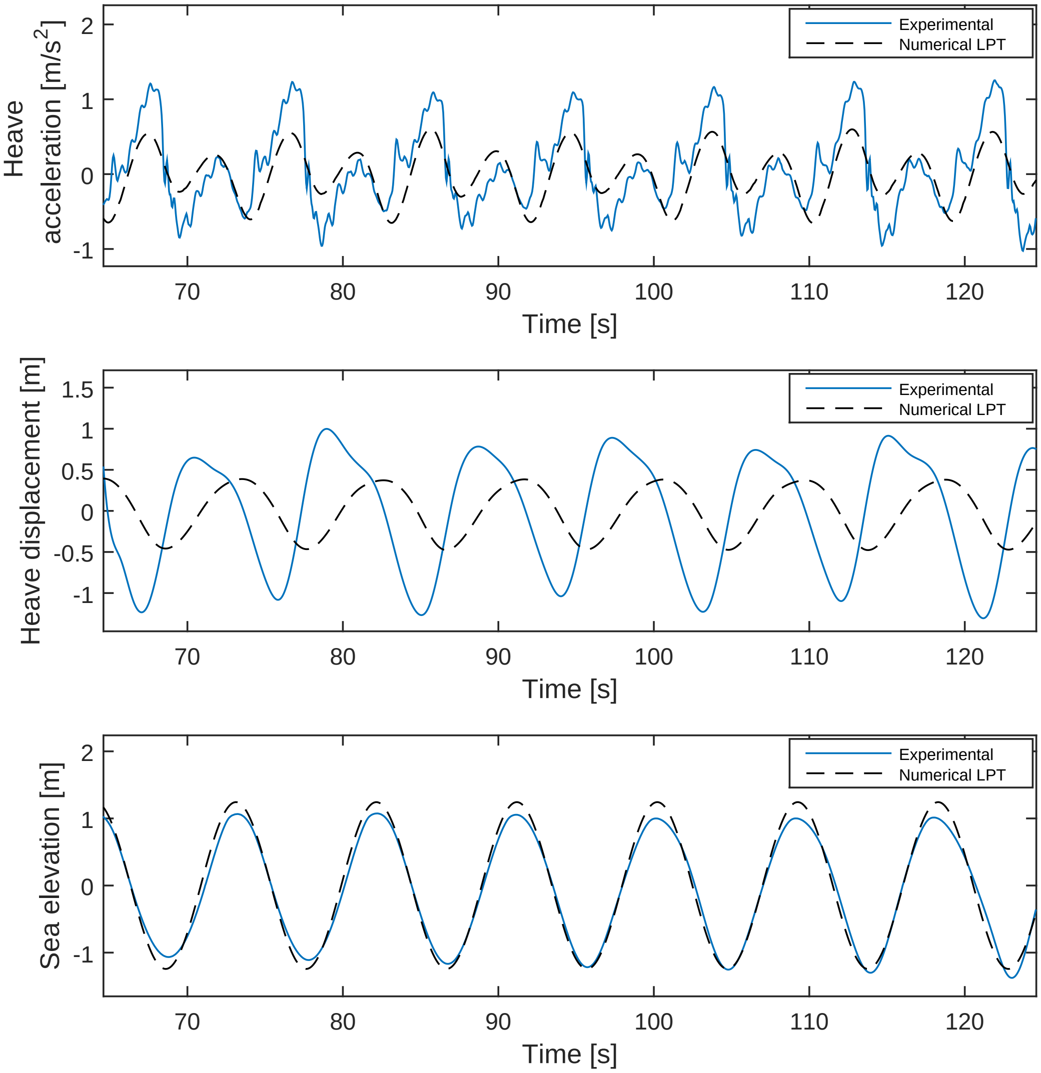

Figure F.11: Comparison of case 5

Case 6: H of 6 m and T of 10 s, with Heave Plates

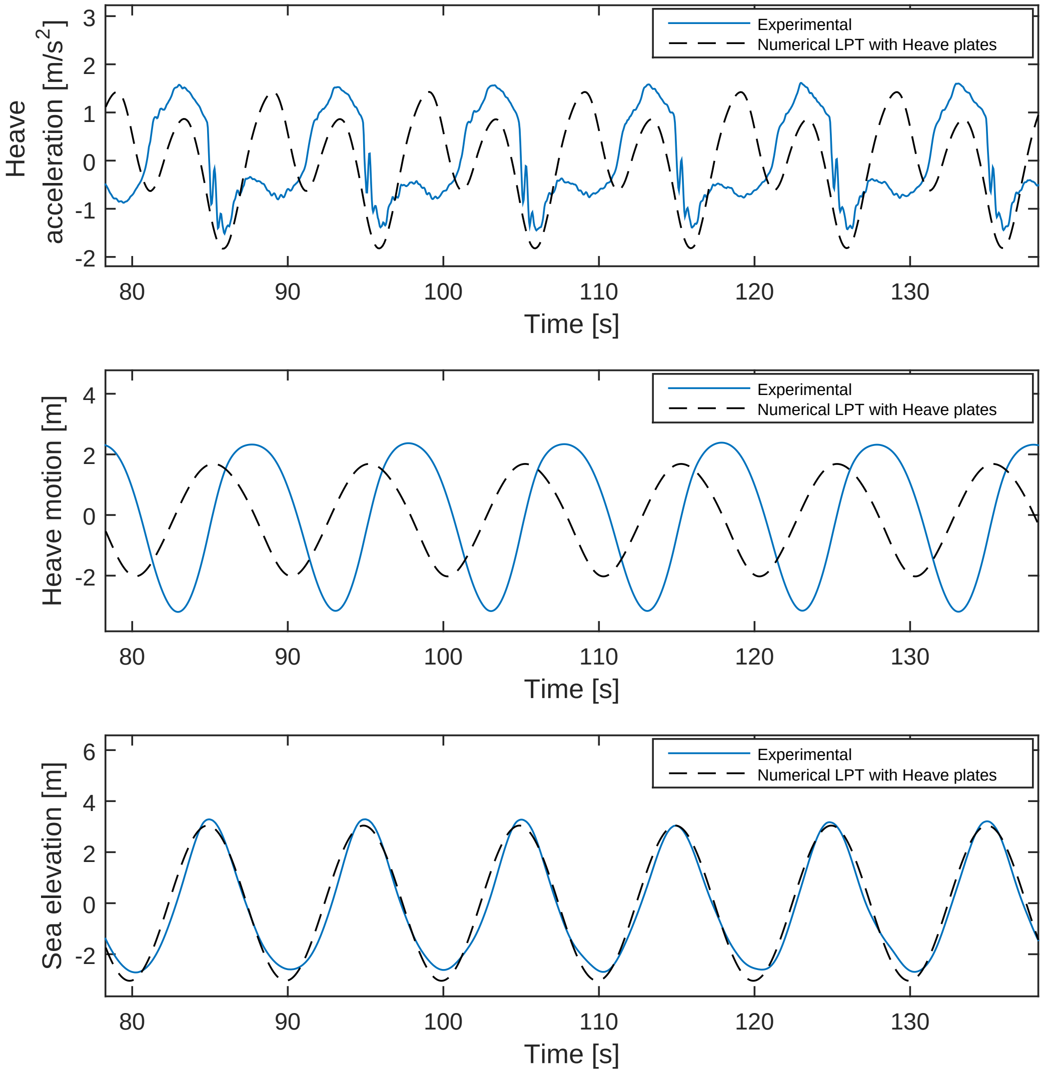

Figure F.12: Comparison of case 6, with heave plates

Appendix G

Verification of Computational Damage

A verification of the computed damage is necessary to outline, to evaluate the fatigue damage. The fatigue damage arises from moments, which arises from acceleration again, and these parameters are of interest when doing a verification study. This section will compute the time series of bending moments based on accelerations of the structure, to see whether 3DFloat calculates the bending moment with the same method.

One sea state from a hypotetical site[19] is used, in the verification study. The environmental parameters for the selected site are listed in Table G.1. The generated irregular waves are established by JONSWAP spectrum, and the majority of the waves within the sea state are assumed to be linear.

Table G.1: Input and measured values from 3DFloat

Hs	**Tp**	**U_{90}**
1.25 m	4s	4 m/s

Illustration and parameters for the fatigue problem are shown in Figure G.1 and Table G.2, where the fatigue point of interest is at the intersection between the column and the tower. This orientation is valid for all fatigue calculations.

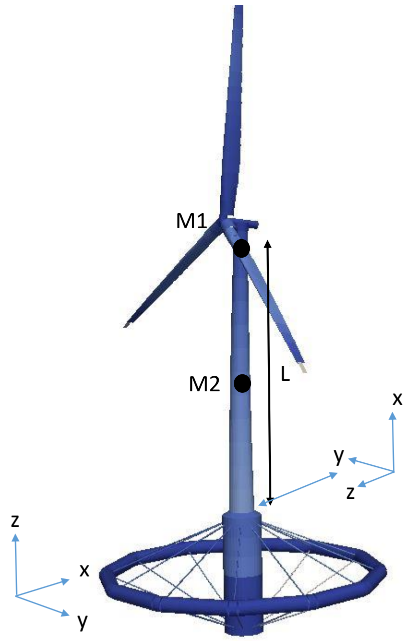

Figure G.1: Fatigue Model

Table G.2: Description of parameters

Parameters	**Value**
L	73.6 m
M1	345.2 tons
M2	426.3 tons

The calculated bending moments is a simplification to the measured values from 3DFloat and have some assumptions.The mass of the tower and rotor is assumed to be two point masses, where 3DFloat has a distributed mass along the tower and the rotor. The center point of the point mass for the tower is selected to be 0.5L out of simplicity, even though it is, in reality, lower (due to a cone shape of the tower). The tower and column are assumed to be rigid, such that rotations are assumed to be constant along the whole height of the structure.

It is possible to calculate the time series bending moment about the y- axis for tower base (see Figure G.1 for orientation) by having these assumptions in mind. This calculation is dependent on the time series of rotations and accelerations from 3Dfloat, and are therefore assumed to be correct. The calculated bending moment is established by using Equation G.1.

$$M_{y_{\text{calculated}}} = (M_1 + M_2 \cdot 0.5)\left[L \cdot \ddot{\eta}_1 + L \cdot \sin(\dot{\eta}_4) \cdot \ddot{\eta}_6 - L \cdot (1 - \cos(\dot{\eta}_5)) \cdot \ddot{\eta}_5)\right]; \tag{G.1}$$

Figure G.2 illustrates the comparison between the calculated bending moment, and the measured bending moment from 3DFloat. A time interval between 2000 and 2500 s from a 1-hour analysis has been selected, to see it more clearly.

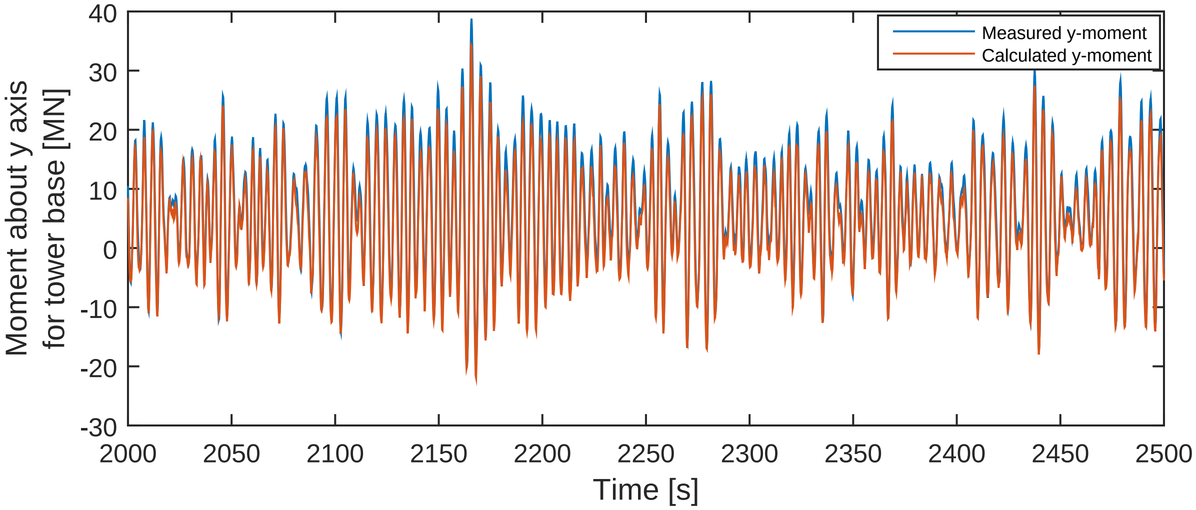

Figure G.2: Moment about y - axis for measured and calculated values

It is from this figure observed that the calculated y-moment is approximately the same as the measured values. There are some differences at the peaks, which is due to the calculation assumptions. A further investigation of the max values for acceleration, moments and forces are established in Table G.3.

Table G.3: Measured and calculated values from 3DFloat

$\ddot{\eta}_{\mathbf{1max}}$	$\ddot{\eta}_{\mathbf{5max}}$	$\mathbf{M}_{\text{ymax}_{\text{3DFloat}}}$	$\mathbf{M}_{\text{ymax}_{\text{calculated}}}$	$\mathbf{N}_{\text{x,mean}_{\text{3DFloat}}}$	$\mathbf{N}_{\text{x,mean}_{\text{calculated}}}$
$0.77 m/s^2$	$0.0695 deg/s^2$	38.8 [MNm]	31.6 [MNm]	7.6 [MN]	7.5 [MN]

The max surge and pitch accelerations are realistic, which means that 3DFloat calculates accelerations accurate. The calculated max bending moments about the y-axis at the tower base are also close, which is an indication that our calculation method is correct. The calculated compression force N_x from the same table is calculated by a simple theory based on the tower and rotor mass and the cross section. The 3DFloat compression force is the mean of the time series, which is a good approximation since the mean heave acceleration is approximately 0 m/s^2. The calculated axial force due to the weight of the rotor and tower is also approximately the same, seen from Table G.3.

It is, to summarize, observed that the calculation of the bending moment is good and that the following stress computation is good. The fatigue damage is, therefore, reliable if the time series of the accelerations are reliable since the damage is based on the variation of stress, represented by a time series.

Bibliography

[1] (2006). 3dfloat user manual. Technical report, IFE.

[2] (2010). Fatigue design of offshore steel structures. Technical Report DNV-RP-C203, DNV.

[3] (2011). Sesam hydrod user manual. Technical report, DNV.

[4] (2013a). Buckling strength of shells. Technical Report DNV-RP-C202, DNV.

[5] (2013b). Structural design of offshore ships. Technical Report DNV-RP-C102, DNV.

[6] (2014). Design of offshore wind turbines. Technical Report DNV-RP-J101, DNV.

[7] Bachynski, E. E. (2014). *Design and Dynamic Analysis of Tension Leg Platform Wind Turbines*. PhD thesis, NTNU.

[8] Breton, S.-P. and Moe, G. (2008). Status, plans and technologies for offshore wind turbines in europe and north america.

[9] Chen, X., Zhang, J., and Ma, W. (1999). On dynamic coupling effects between a spar and its mooring lines. *Ocean Engineering*, 28(2001):873.

[10] Chowdhury, I. and Dasgupta, S. P. (2003). Computation of rayleigh damping coefficients for large systems.

[11] Colton, D. and Kress, R. (2013). *Integral Equation Methods in Scattering Theory*.

[12] Dabell, B. J. and Wtson, P. (1975). Symposium on statistical aspects of fatigue testing.

[13] Dowling, N. E. (1972). Fatigue failure prediction for complicated stress-strain histories. *Journal of Materials*.

[14] EUCO (2014). *2030 Climate and Energy Policy Framework.* http://www.consilium.europa.eu/uedocs/cms_data/docs/pressdata/en/ec/145397.pdf [Accessed: 13.08.2016].

[15] Faltinsen, O. M. (1990). *Sea Loads on Ship and Offshore Structures.* Cambridge University Press.

[16] Felippa, C. A. and Haugen, B. (2005). *Unified Formulation of Small-Strain Corotational Finite Elements: I. Theory.* Technical Report CU-CAS-05-02, Department of Aerospace Engineering Sciences and Center for Aerospace Structures.

[17] Gao, Z. (2014). *Frequency- and time-domain stochastic analysis of wave induced dynamic responses.*

[18] Gao, Z. (2015). *TMR4505: Integrated Dynamic Analysis of Wind Turbines, Powerpoint: Hydrodynamic analysis of offshore wind turbines.*

[19] Gao, Z. and Bachynski, E. (2015). Course project: Integrated dynamic analysis of wind turbines fall 2015.

[20] Gavin, H. P. (2016). Numerical integration in structural dynamics.

[21] Greco, M. (2012). *TMR4215: Sea Loads, Lecture Notes.*

[22] Hansen, M. O. L. (2008). *Aerodynamics of Wind Turbines, 2nd edition.*

[23] Heronemus, W. E. (1972). *Pollution-Free Energy From The Offshore Winds.* Washington D.C.

[24] Jonkman, J. and Musial, W. (2010). Offshore code comparison collaboration (oc3) for iea task 23 offshore wind technology and deployment. Technical report, NREL.

[25] Jonkman, J. M. (2007). *Dynamics Modeling and Loads Analysis of an Offshore Floating Wind Turbine.*

[26] Kvittem, M., Bachynski, E., and Moan, T. (DeepWind January 2012, Trondheim). *Effects of Hydrodynamic Modelling in Fully Coupled Simulations of a SemisubmersibleWind Turbine.*

[27] Li, L., Gao, Z., and Moan, T. (2013). Joint environmental data at five european offshore sites for design of combined wind and wave energy devices. *International Conference on Ocean, Offshore and Arctic Engineering*.

[28] Lindenburg, C. (2005). User manual: Program from horizontal axis wind turbine analysis and simulation.

[29] Lindenburg, C. and Snel, H. (2004). Aero-elastic stability analysis tools for large wind turbine rotor blades.

[30] Logan, D. L. (2011). *A First Course In The Finite Element Method*. CL Engineering.

[31] Lu, M.-S., Chang, C.-L., Lee, W.-J., and Wang, L. (2008). Combining the wind power generation system with energy storage equipments.

[32] Maastad, M. B. (2016). Numerical and experimental study of the fred olsen wind turbine concept. Master's thesis, Norwegian University of Science and Technology.

[33] Maastad, M. B. and de Vaal, J. B. (2016). Implementation of lpt software in 3dfloat. E-mail correspondance.

[34] Maastad, M. B. and Kristiansen, T. (2016). Drag coefficients on horizontal cylinder in the sea surface. E-mail correspondance.

[35] MacCamy, R C ; Fuchs, R. A. (1954). *WAVE FORSES ON PILES: A DIFFRACTION THEORY*. CL Engineering.

[36] Matsuishi, M. and Endo, T. (1968). Fatigue of metals subjected to varying stress. In *Proceedings at Kyushu Branch of Japan Society of Mechanics Engineering*, pages 37–40.

[37] Moriarty, P. and Hansen, A. (2005). *AeroDyn Theory Manual*. `http://www.nrel.gov/docs/fy05osti/36881.pdf` [Accessed: 26.05.2016].

[38] Muren, M. (2015). Load and response calculation from wave impacts on columns of semi-submersibles. Master's thesis, Norwegian University of Science and Technology.

[39] Musial, W. and Butterfield, S. (2006). Energy from offshore wind.

[40] Nygaard, T. A. (2015). 3dfloat: Aero-servo-hydro-elastic computations for offshore wind turbines.

[41] Sieminski, A. (2016). *International Energy Outlook 2016*. http://www.eia.gov/pressroom/presentations/sieminski_05112016.pdf [Accessed: 13.08.2016].

[42] Steen, S. (2014). *Experimental Methods in Marine Hydrodynamics*. NTNU: Department of Marine Technology.

[43] WAMIT, I. Wamit, inc. user manual. http://www.wamit.com [Accessed: 15.08.2016].

[44] Watson, G., Hill, B., and Courtney, F. (2005). A framework for offshore wind energy development in the united states.